



Politecnico di Bari

Repository Istituzionale dei Prodotti della Ricerca del Politecnico di Bari

Application and processing of Time Domain Reflectometry: a model-based approach

This is a PhD Thesis

Original Citation:

Application and processing of Time Domain Reflectometry: a model-based approach / D'Aucelli, Giuseppe Maria. - (2018). [10.60576/poliba/iris/d-aucelli-giuseppe-maria_phd2018]

Availability:

This version is available at <http://hdl.handle.net/11589/120645> since: 2018-01-22

Published version

DOI:10.60576/poliba/iris/d-aucelli-giuseppe-maria_phd2018

Publisher: Politecnico di Bari

Terms of use:

(Article begins on next page)



**Politecnico
di Bari**

Department of Electrical and Information Engineering

ELECTRICAL AND INFORMATION ENGINEERING PH.D. PROGRAM
SSD: ING-INF/07 - ELECTRIC AND ELECTRONIC MEASUREMENTS

FINAL DISSERTATION

**Application and processing of Time Domain
Reflectometry: a model-based approach**

by:
Giuseppe Maria D'AUCELLI

Supervisor:
Prof. Ing. Nicola GIAQUINTO

Coordinator of Ph.D. Program:
Prof. Ing. Vittorio M. N. Passaro

Course n° 30, 01/11/2014 - 31/10/2017



Politecnico di Bari

Department of Electrical and Information Engineering

ELECTRICAL AND INFORMATION ENGINEERING PH.D. PROGRAM
SSD: ING-INF/07 - ELECTRIC AND ELECTRONIC MEASUREMENTS

FINAL DISSERTATION

Application and processing of Time Domain Reflectometry: a model-based approach

by:
Giuseppe Maria D'AUCELLI

Referees:
Prof. Ing. Stefano Pisa
Prof. Dr. Christof Hübner

Supervisor:
Prof. Ing. Nicola GIAQUINTO

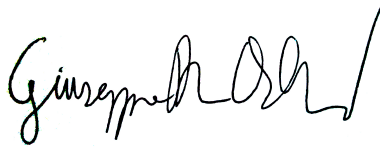
Coordinator of Ph.D. Program:
Prof. Ing. Vittorio M. N. Passaro

Course n° 30, 01/11/2014 - 31/10/2017

Declaration of Authorship

I, Giuseppe Maria D'AUCELLI, declare that this thesis titled, "Application and processing of Time Domain Reflectometry: a model-based approach" and the work presented in it are my own. I confirm that:

- This work was done wholly or mainly while in candidature for a research degree at this University.
- Where any part of this thesis has previously been submitted for a degree or any other qualification at this University or any other institution, this has been clearly stated.
- Where I have consulted the published work of others, this is always clearly attributed.
- Where I have quoted from the work of others, the source is always given. With the exception of such quotations, this thesis is entirely my own work.
- I have acknowledged all main sources of help.
- Where the thesis is based on work done by myself jointly with others, I have made clear exactly what was done by others and what I have contributed myself.



Signed:

Date: 18/12/2017

“Put an intelligent (possibly) quote here”

Giuseppe Maria D’Aucelli

POLYTECHNIC UNIVERSITY OF BARI

Abstract

Department of Electrical and Information Engineering

Doctor of Philosophy

Application and processing of Time Domain Reflectometry: a model-based approach

by Giuseppe Maria D'AUCELLI

In this thesis a full featured workflow for the implementation of integrated diagnosis and monitoring systems based on Time Domain Reflectometry (TDR) is proposed.

First it is shown how TDR probes installed in TDR-based setups can be adopted with simpler and cheaper techniques, then newly developed DSP algorithms for direct reflectogram analysis are presented.

Afterwards, the TDR inverse problem, i.e. estimating the profiles of Transmission Line parameters from reflectograms, is dealt with. LineLab, a custom, reflectometry oriented frequency and time domain Transmission Line simulator is presented as simulation tool, and the jDE optimization algorithm is applied to successfully solve the inverse problem in both synthetic and real life scenarios.

Both synthetic and experimental results are illustrated. The proposed techniques are of immediate practical application in a number of fields, such as leakage detection, concrete structures monitoring, precision agriculture, cable soft-fault detection, etc. Besides, they pave the way towards the realization of an integrated low-cost TDR instrument capable of continuous monitoring with both on-device and in the cloud processing and profile reconstruction features.

Acknowledgements

So, this is the part where things get dramatic, and even somehow melancholic. This is where doctoral candidates express their most sincere gratitude toward the institution(s) that brought them to the coveted goal of adding “PhD” to their email signature. But this, dear readers, is an engineering PhD thesis, is it not? And one written by someone who notoriously likes to tell and listen to stories. As an obvious convergence between these two points, I would like to state some facts.

First, I would like to turn back the clock to three years ago, when I took this fateful decision. I have always been an engineer on the inside: I wanted to know how things worked, to customize tech and, of course, to make it work (almost) as intended. One may ask himself what does “almost” mean, but this is a long story. Just stick to the fact that research is a lot of things, but it is seldom about making stuff actually work: as I learned, it is mostly about proving that stuff can work, but in the end, and deeply, you are not required to produce something that someone could install behind his couch and use on a daily basis.

Science, baby.

So why a PhD course? Because my advisor means it differently: stuff must work, otherwise there is no purpose in writing a paper about it, right? Whether it is uncertainty assessment or sensor prototyping: you write about tech that works. This is on you, Professor, and I promise that, as long as I am a researcher, this assumption will hold.

Besides, many things have changed during these three years, and many a thunderstorm has roared. Fact is that I grew up as a man as much as a professional, however my focus here goes to the human side of it. Disenchantment is what has been lurking in the shadows, and from time to time it comes out to take its toll. Think of it as the overabused darkness in that Simon & Garfunkel song but, in this case, it comes to me. I swear I always try to act as candidly as I can, implying that I always play by the rules. Some may say that this, sometimes, results in a naive attitude or, quoting a good friend of mine, that I am (literally) clueless. This is not (entirely) true. I have, in fact, also been taught to read unwritten rules, but what I did not learn is to abide by them. Therefore, I hereby state that I terribly hate unwritten rules. Thank you, academy, and thank you, music business, for enlightening me.

Final fact: it does not end here. And that, dear science, is a threat. Whatever happens, I will always remember how good it tastes to have a good idea and prove that it actually works: that is what I’m yearning for.

For me, for my friends, for my family.

I managed to find Uno and Checkers, and Battleship and most of the pieces of Candyland. Which I figure, we can mix together to create a fabulous new game, Candyship Battleland. War never tasted so good!

Lorelai Gilmore

Contents

Declaration of Authorship	iii
Abstract	vii
Acknowledgements	ix
1 Introduction	1
1.1 Distributed measurements with Time Domain Reflectometry	1
1.2 TDR waveform processing	2
1.3 Purpose of this thesis	3
2 Diagnostics on TDR probes with TDR-related techniques	7
2.1 Introduction	7
2.2 Preliminary theoretical analysis	8
2.2.1 C and ToF variations with the presence of water	8
2.2.2 C and ToF variations with temperature	10
2.2.3 Numerical computations and simulations	11
2.3 Experimental setup	12
2.3.1 Measurement methods and instrumentation	12
2.3.2 Setup for Determining the Sensitivity to the Presence of Water	13
2.3.3 Setup for Determining the sensitivity to temperature varia-	
tions	14
2.4 Experimental results for the sensitivity to the presence of water	14
2.4.1 Capacitance measurements	15
2.4.2 Time of flight measurements	18
2.5 Sensitivity to temperature variations	22
2.5.1 Capacitance measurements	22
2.5.2 Time-of-Flight measurements	22
2.5.3 Effect of temperature on water sensing	23
2.6 Discussion of results	23
2.7 Conclusions	24
3 Time-of-Flight estimation from TDR waveforms	27
3.1 Introduction	27
3.2 Signal preconditioning and error model	29
3.3 Materials, methods and measurement protocols	31
3.3.1 Experimental setup for measurements on cables with known	
parameters	31

3.3.2	Experimental setup for water level measurement application	32
3.3.3	Time-of-Flight estimation criteria	32
3.4	Experimental results and repeatability study	33
3.4.1	Measurements on cables with known propagation velocity	33
3.4.2	Repeatability study	36
3.4.3	Measurements on cables with unknown electrical parameters	36
3.5	Test application: water level measurement	37
3.5.1	Analytic ToF model for two layered materials	40
3.5.2	Experimental design	41
3.5.3	Water level measurements as ToF estimation benchmark	42
4	Theoretical background and TL simulation algorithms	47
4.1	Introduction	47
4.2	Simplified measurement setup	48
4.3	TEM propagation mode and its equivalent circuit	49
4.4	Telegraph equations in the time domain	50
4.4.1	Finite Difference Time Domain algorithm	51
4.4.2	Modeling losses and dispersion in the time domain	52
4.5	Telegraph equations in the frequency domain	54
4.5.1	Modeling losses and dispersion in the frequency domain	54
4.6	TDR simulation with arbitrarily profiled parameters	55
4.6.1	The nodal analysis approach	56
4.6.2	Fast tridiagonal solver	57
4.6.3	Final remarks about the simulation algorithm	58
4.6.4	Simulation outputs	60
4.6.5	Reference transmission line	60
4.6.6	Frequency domain results	61
4.6.7	Time domain results	63
4.7	Case studies	66
4.7.1	Concentrated capacitive fault	68
4.7.2	Distributed Gaussian profile of capacitance	68
4.7.3	Step-like capacitive faults	68
4.7.4	Distributed rectangle-like resistive fault	68
5	Calibration of the TDR setup for simulation-based measurements	73
5.1	Overview of the time domain calibration problem	73
5.2	Stimulus calibration	77
5.2.1	Experimental results for v_s	78
5.3	Full featured calibration procedure	82
5.3.1	Connectors network calibration	84
5.3.2	Generator internal impedance calibration	85
5.3.3	Shifting the reference plane	89

6	Simulation-based reconstruction of distributed parameters	93
6.1	Introduction	93
6.2	Choice of the parameters set	94
6.2.1	Concentrated capacitance faults	95
6.2.2	Profile of capacitance as sum of Gaussian curves	96
6.2.3	Staircase-like profile of capacitance	97
6.2.4	Generic smooth profile of capacitance	99
6.3	Target function	99
6.4	Synthetic optimization results	102
6.4.1	Simple Gaussian profile	103
6.4.2	Two overlapping Gaussian profiles	106
6.5	Experimental results	110
7	Conclusions and future work	115
A	MATLAB implementations of the simulation algorithm	117
A.1	Foreword	117
A.2	Line builder module	117
A.3	LineLab frequency domain simulation module	118
A.4	LineLab time domain simulation module	125
A.5	Subroutines and other utilities	127
A.5.1	Base values for the primary parameters	128
A.5.2	Primary parameter profile composition	130
A.5.3	Transverse impedance	133
A.5.4	Longitudinal impedance	134
A.5.5	Frequency domain parameters	135
A.5.6	Tridiagonal solver	137
	Bibliography	139

List of Figures

1.1	Voltage measured at the reflectometry port on a TL loaded with an arbitrary impedance Z_L	2
1.2	Voltage measured at the reflectometry port with an impedance mismatch in the middle of the line	2
1.3	Example of distributed sensing: a TDR probe in presence of an arbitrary dielectric constant profile.	3
1.4	Block diagram representation of a generic TDR setup for distributed measurements	5
2.1	Simplified schematization of the cross section of the used bi-wires.	9
2.2	Schematization of the SE detecting the presence of a wetting medium surrounding a portion of length Δl . The quantities ϵ_{eff1} and ϵ_{eff2} are the effective permittivities when the wetting medium is absent or present.	10
2.3	Effective relative permittivity ϵ_{eff} of the SE surrounded by a cylindrical volume with given radius (0.5, 1, 2, 5, 10, 20 cm) and given permittivity ϵ_m (in the 50 - 100 range).	12
2.4	Sketch of the positioning of the bi-wire inside the container: top view (<i>left</i>) and lateral cross section (<i>right</i>).	14
2.5	Positioning of the bi-wire in the thermally-controlled box (TCB).	15
2.6	Capacitance measurements for the 20 m-long bi-wire, water addition every 300 seconds (left vertical axis). The behavior of the ambient and of the water temperatures is also reported (right vertical axis).	16
2.7	Time-of-flight measurement for the 20 m-long bi-wire (water addition every 300 seconds). The behavior of the ambient and of the water temperatures is also reported.	17
2.8	Measured and fitted values of the capacitance (C), as function of relative wet length ($\Delta l/l_0$).	19
2.9	Measured and fitted ToF values as function of relative wet length ($\Delta l/l_0$).	21
2.10	Percentage capacitance variation as function of temperature for different lengths of the bi-wire.	24
2.11	Percentage ToF variation as function of temperature for different lengths of the bi-wire.	25
3.1	Reflectogram denoising with Nicolson's technique	31
3.2	Sketch of the experimental setup for water level measurement	33

3.3	Rising edge of the reflectogram acquired on a 15 cm long coaxial cable, its derivative, and POIs.	34
3.4	Measured reflectograms for different cable lengths	36
3.5	Set of 100 noisy reflectograms ($l = 30$ cm)	37
3.6	Repeatability analysis for a 10 cm long cable in terms of average measured length (a) and standard deviation (b)	38
3.7	Repeatability analysis for a 30 m long cable in terms of average measured length (a) and standard deviation (b)	39
3.8	TDR (step-like) signal on a completely dry probe	40
3.9	TDR (step-like) signal on a wet probe	41
3.10	ToF versus wet biwire length: compared calibration curves	43
3.11	Reflectogram flattening in presence of high wet lengths	44
3.12	Water level measurement calibration curve for the TC criterion	45
4.1	Two port model of a TDR measurement apparatus	49
4.2	Transmission line elementary cell	50
4.3	Generator and load sections of the TL equivalent circuit	52
4.4	Convolution-free approximation of frequency-dependent primary parameters as proposed in [69]	53
4.5	Simplified elementary cell	57
4.6	Simulation times for fixed number of elementary cells $N_x = 1000$	59
4.7	Cross section of the simulated coaxial line	60
4.8	Reflection coefficient at reflectometry port (S_{11}) for a simulated 1 m long coaxial cable left open-ended	62
4.9	$ S_{11} $ simulation for a 1 m long coaxial cable (RG-58 CU) performed in different simulation environments.	63
4.10	Time Domain Reflectometry on a 50m long coaxial cable, using a synthetic Gaussian pulse as stimulus signal	64
4.11	Time Domain Reflectometry on a 50m long coaxial cable with step-like stimulus, obtained by numerical integration of the pulse response	65
4.12	Case studies for the analysis of non-homogeneous Transmission Lines	67
4.13	Concentrated capacitive fault in a 50m long line, centered at $l_f = 25$ m	69
4.14	Distributed capacitive fault in a 100m long line, centered at $l_f = 50$ m	70
4.15	Interfaces between materials with different ϵ_r located at $l_f^{(1)} = 0.25l$ and $l_f^{(2)} = 0.75l$, with $l = 100$ m	71
4.16	Distributed resistive fault in a 100m long line, centered at $l_f = 50$ m	72
5.1	Realistic model of a TDR measurement setup	75
5.2	Campbell Scientific CS605 3-Rod TDR Probe with RG58 Cable [75]	75
5.3	Basic TDR setup with negligible interconnections	79
5.4	TDR network model and calibration circuit (negligible interconnections)	80
5.5	Calibration of an 8ns pulse stimulus supplied by Agilent 33250A AWG through a short RG58-CU cable	81

5.6	TDR waveform measured on a $\sim 50\text{m}$ long RG58-CU coaxial cable with a $\sim 10\text{ns}$ wide pulse-like stimulus (Fig. 5.5)	83
5.7	$ S_{11} $ for a 40 cm long RG316-U cable: model versus actual measurements	85
5.8	Calibration equivalent circuit for the estimation of v_S and Z_S	86
5.9	Two configurations for v_S and Z_S calibration	87
5.10	Measured (NI PXIe-5632 VNA) terminator impedance	89
5.11	Measured derivatives of the step-like stimulus signal from the fast edge generator of Tektronix MSO71254C oscilloscope and its calibrated counterpart	90
5.12	Compensated and uncompensated reflectograms simulated with a 1m long coaxial line preceding a 10m long bi-wire. The solid line simulates the time domain response taken by shifting the reference plane to the interface between the lines	91
6.1	Capacitance profile with three concentrated faults	96
6.2	Composing a generic capacitance profile using Gaussian curves	98
6.3	Staircase-like capacitance profiles	100
6.4	Generic smooth profile of capacitance	101
6.5	A conventional Differential Evolution flowchart [91]	104
6.6	Synthetic measurement data for the reconstruction of simple Gaussian profiles: profiles to be reconstructed and simulated TDR measurements	105
6.7	Best fitness versus number of evaluations in jDE for the reconstruction of the Gaussian profiles of Tables 6.1, 6.2 and 6.3	107
6.8	Best fitness versus number of evaluations in jDE for the reconstruction of the Gaussian profiles of Tables 6.4, 6.5 and 6.6	109
6.9	Intermediate optimization results for the problem outlined in Table 6.6	109
6.10	Junction between 5 m long RG58-CU coaxial cables	110
6.11	“F1” (left) and “F2” (right) capacitive fault devices	111
6.12	Measured and reconstructed reflectogram on the 30 m long coaxial line without faults	111
6.13	Measured versus reconstructed TDR waveforms for the first dataset, detail on relevant reflectogram features	112
6.14	Target function values for the first dataset	113

List of Tables

2.1	AWG-18 electrical parameters.	9
2.2	Measured capacitances (C) for different lengths (l_0) of the bi-wire and for different wetted lengths (Δl).	18
2.3	Measured ToFs for different lengths (l_0) of the bi-wire and for different wetted lengths (Δl).	20
3.1	DUT electrical parameters	32
3.2	Gain, Offset and Nonlinearity errors in the estimation of cable length with the three considered criteria	35
3.3	Propagation velocity estimated with the three considered criteria (nominal velocity: $0.83c$)	35
3.4	Gain, Offset and Maximum errors in the estimation of the length of biwires with the three considered criteria	37
3.5	Nonlinearity errors for each criterion	43
4.1	Frequency dependent resistance and inductance in coaxial lines and twin leads	55
4.2	Simulator features comparison	63
5.1	Simulation parameters for a ~ 50 m long RG58-CU coaxial cable	82
6.1	Optimization results for simple Gaussian profile 1	106
6.2	Optimization results for simple Gaussian profile 2	106
6.3	Optimization results for simple Gaussian profile 2	106
6.4	Optimization results for two overlapped Gaussian profiles (1)	108
6.5	Optimization results for two overlapped Gaussian profiles (2)	108
6.6	Optimization results for two overlapped Gaussian profiles (3)	108
A.1	Available profile shapes	130

List of Abbreviations

TDR	Time Domain Reflectometry
FDR	Frequency Domain Reflectometry
TL	Transmission Line
TE	Transverse Electric
TM	Transverse Magnetic
TEM	Transverse ElectroMagnetic
FDTD	Finite Difference Time Domain
DUT	Device Under Test

*To my beloved Valentina
To Minerva*

Chapter 1

Introduction

Going out of your door. You step onto the road, and if
you don't keep your feet, there's no knowing where
you might be swept off to

THE HOBBIT OR THERE AND BACK AGAIN. BY BILBO
BAGGINS

1.1 Distributed measurements with Time Domain Reflectometry

Time Domain Reflectometry (TDR) can safely be assumed to be the cheapest and simplest technique for distributed sensing applications in a very broad range of sensing element (SE) sizes, from a few centimeters [1] to several tens of meters and more [2] and, therefore, for an even broader range of applications.

Basically, TDR consists in stimulating a suitably designed Transmission Line (TL) with a wideband voltage stimulus, usually a step or pulse-like burst and monitoring the incident and reflected voltage waves at a specific point on the line. Figure 1.1 schematically depicts the simplest possible TDR configuration, where a TL loaded with an arbitrary impedance Z_L is stimulated by a step-like signal. The voltage wave travels along the line and, if the load impedance does not match its characteristic impedance, is partially reflected. The amplitude of the reflected wave depends on the impedance mismatch and the time interval Δt after which the reflected wave is detected at the reflectometry port is proportional to the length of the line. Typically, in TDR application, the measurement port is coincident with the stimulus port and the line is left open ended, i.e. $Z_L \rightarrow \infty$.

Impedance mismatches can also occur at some point in the middle of the line, as shown in Figure 1.2. In this case, the traveling wave is partially reflected before reaching the load, and such reflection(s) are immediately visible as features on the measured waveform. The time elapsed between the forward wave and the partial reflections can also be considered proportional to the physical distance of the mismatches.

Such mismatches can be introduced by a broad range of physical phenomena, from the compression of a coaxial cable [3] to the change in the dielectric constant

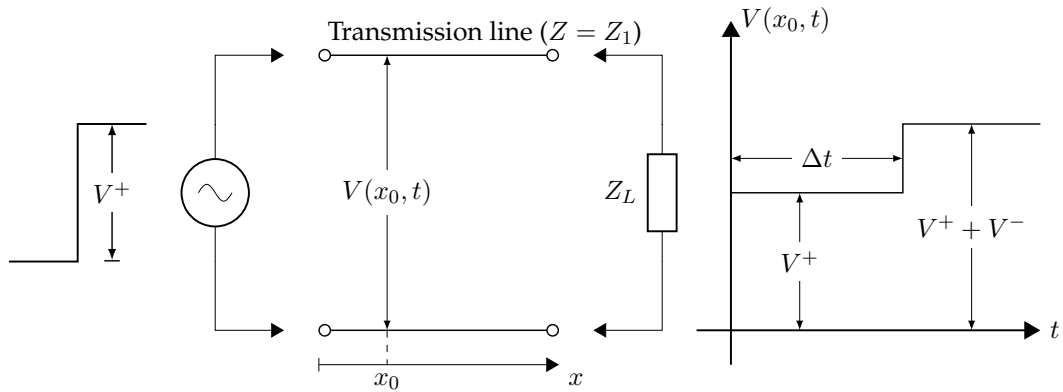


FIGURE 1.1: Voltage measured at the reflectometry port on a TL loaded with an arbitrary impedance Z_L

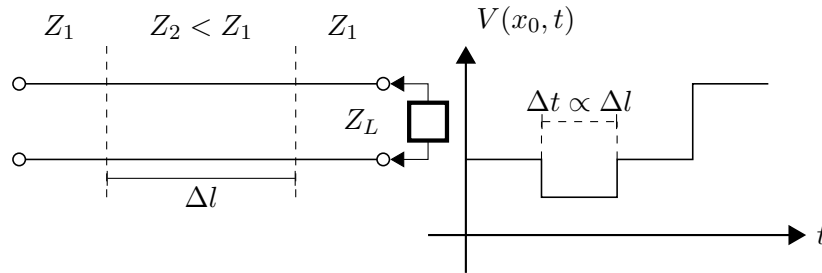


FIGURE 1.2: Voltage measured at the reflectometry port with an impedance mismatch in the middle of the line

of the material surrounding a twin lead (Figure 1.3) or any other appropriate Transmission Line [4]. Generally and theoretically speaking, therefore, this technique can be used to measure any physical quantity that somehow modifies the properties of a suitably designed TL [5].

1.2 TDR waveform processing

Although much effort has been spent on developing efficient and robust TDR processing techniques, still the most widespread algorithms are based on direct reflectogram processing. For example, if the stimulus signal is a voltage step, the time instant where the derivative of the reflectogram reaches its apex is associated to the group velocity of the incoming wave packet and, therefore, can be used to infer the dielectric permittivity of the transmission line [6]. Time of Flight (ToF) Estimation algorithms based on direct reflectogram processing have been developed and characterized [7], achieving excellent results in terms of accuracy. Such algorithms can provide a simple and quick yet preliminary interpretation of the reflectograms, and can be used for real-time diagnostic applications or for applications that require, e.g., the detection of abrupt changes of characteristic impedance along the line [8].

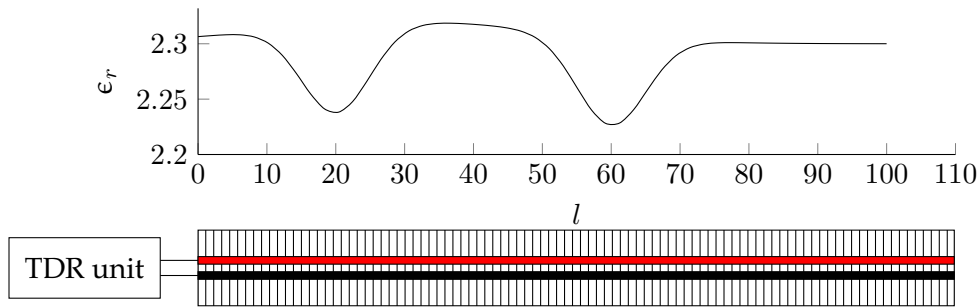


FIGURE 1.3: Example of distributed sensing: a TDR probe in presence of an arbitrary dielectric constant profile.

Nevertheless, much more information can be inferred from TDR waveforms, provided that an accurate and detailed model of the probe under working conditions is available. TDR is, in fact, closely related to more expensive and complex measurement techniques based on vector network analysis or impedance spectroscopy [9]. Interesting results can be achieved by analyzing the frequency content of reflectograms with Fourier domain algorithms, allowing to characterize the dielectric properties of materials [10] without actually carrying out vector network analysis, which is usually unfeasible in harsh or uncontrolled environments (i.e. petrochemical industry, waste processing plants etc.).

Other approaches to TDR processing based on system identification and echo modeling are also available in literature [11]. However, these techniques are not suitable to applications where the material surrounding the probe is not homogeneous or made up by discrete layers of homogeneous materials, e.g. in precision agriculture, building health monitoring, pipe leak detection [12] and so forth.

An interesting technique for the restoration of the incident signal from the transient response of Transmission Lines by means of compact Green functions has been presented in the 90s by Lundstedt [13]–[15]. This approach has also been recently applied to the non-destructive diagnosis of wiring networks [16], where the application requires finding and characterizing concentrated faults on long lines.

Finally, the most advanced techniques for reflectogram processing currently available rely on optimization algorithms [17]–[19] or identification techniques [20]. The approaches presented in literature, however, are always highly application-specific, thence being hardly reproducible and lacking versatility.

1.3 Purpose of this thesis

In this thesis, an integrated approach to distributed sensing employing TDR and TDR-related measurement techniques is presented. The work is organized as follows.

First, the fact that TDR probes can be used even independently from the Time Domain Reflectometry itself for extremely cost-effective diagnostic purposes is considered. Simpler and cheaper techniques than TDR, i.e. Time-of-Flight (ToF) measurements and capacitometry are investigated, as they can straightforwardly be applied to

the same sensing elements employed in TDR measurements, and can trigger alerts in case of anomalies [21].

Then an automated procedure for basic TDR processing is presented [7] that accurately computes the ToF and can be employed for real-time diagnostics in leak detection systems [22] and sibling applications. A simple application to water level measurement is also discussed to assess the accuracy of the proposed method.

Going further, it is considered that TDR waveforms virtually embed any needed information on the Transmission Line used as a probe in the spectrum defined by the frequency content of the stimulus signal. Two important facts, however, need to be stated:

- It is impossible to infer every line parameter from a reflectogram, i.e. some parameters need to be considered known
- Measurement systems need to be rigorously modeled, and model constraints must hold under well defined working conditions.

This means that a well-established and straightforward workflow needs to be defined for distributed measurement applications. Design steps that need to be defined are:

1. Distributed probe design and optimization
2. Characterization of transitions and/or cables connecting the TDR instrumentation to the probe
3. Definition of the typical operating conditions
4. Definition of a suitable electromagnetic model of the TL
5. Choice of a reconstruction algorithm for the parameter(s) under test

For the purpose of this thesis, focus is given especially to steps 4 and 5. A Transmission Line simulation approach to advanced TDR processing, designed for the estimation of distributed quantities is proposed and its applicability to both traditional and cheaper TDR setups is demonstrated.

From the measurement point of view, the idea behind this work consists in modeling the setup as a generic (dispersive and non homogeneous) Transmission Line, stimulated by the actual TDR signal. The building blocks of a general reflectometry-based system, also depicted in Figure 1.4 are:

- Test signal generator
- Acquisition and digitizing instrumentation
- Intermediate cables, connectors and transitions
- TDR probe
- Material under test

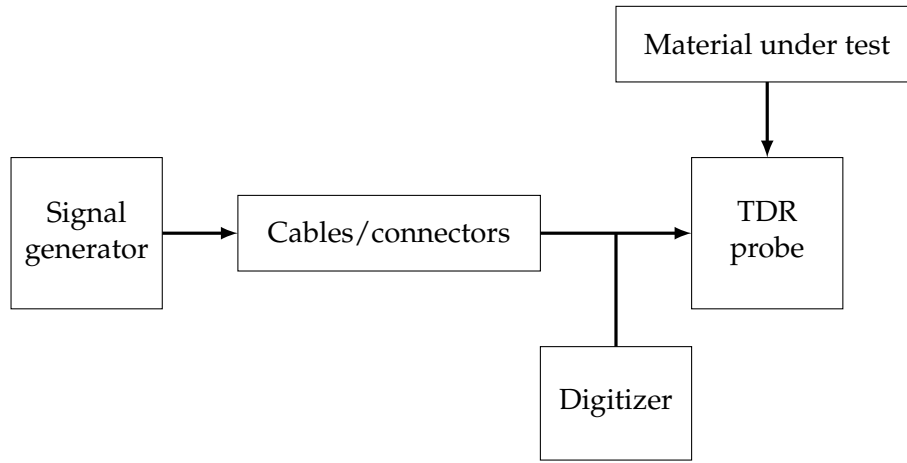


FIGURE 1.4: Block diagram representation of a generic TDR setup for distributed measurements

The proposed approach consists in accurately modeling each of these blocks and implementing an integrated simulation algorithm capable of reproducing measured waveforms based on theoretically sound equations and physically reasonable parameters. The proposed software implementation of this algorithm, based on a custom made TL simulator [23], is also verified on real life, although perfectly controlled experimental conditions.

Afterwards, actual measurements are performed following the recently introduced principles of "TDR inversion" [17], [18] on fully characterized measurement systems. Traditional optimization algorithms are compared in different case studies of increasing complexity, and finally a stochastic approach based on Markov chain Monte Carlo algorithms is presented that enables taking into account the uncertainty of the estimated parameters.

The estimation algorithms hereby presented are fairly heavy from a computational cost perspective, therefore a simple client-server architecture that processes data acquired from on-site TDR instrumentation and provides a user interface for the analysis of the results is also briefly outlined.

Chapter 2

Diagnostics on TDR probes with TDR-related techniques

It has long been an axiom of mine that the little things
are infinitely the most important

ARTHUR CONAN DOYLE, THE MEMOIRS OF
SHERLOCK HOLMES

2.1 Introduction

Real-time monitoring and diagnostics have become increasingly important, coherently with the growing interest towards a smart city-oriented approach to monitoring. However, since most monitoring solutions rely on point sensors, it becomes difficult to quickly obtain comprehensive information when the areas to be monitored are large and extended. In fact, in these cases, a large number of point-sensors should be employed, with all the related consequences in terms of interrogating such a multitude of sensors. Typical examples of such situations is the monitoring of water infiltrations in a large area, e.g. in the structure of a building [24]–[27] or moisture content determination in generic materials [28]–[30], and in soils [31]. In addition to this, many commercial sensors often work on battery, thus requiring periodic maintenance.

On the other hand, in recent works (e.g. [12], [2] and [32]), it has been demonstrated the usefulness of passive, wire-like sensors (e.g. bi-wires) to accurately locate the presence of water in large areas, employing specific measurement techniques based on the analysis of time domain reflectometry (TDR) waveforms. In these applications, SE's may be tens of meters long and can follow any desired path in the system to be monitored, thus allowing to obtain a diffused profiling with a single SE, also when monitoring interfaces between multiple materials [33]. Additionally, the bi-wire SE's are passive, hence, they do not require batteries nor maintenance.

However, while bi-wires are inexpensive, TDR instrumentation is not. Cost is an issue when a large set of bi-wire sensors (as a sensor network) must be monitored, to promptly detect the presence of water in a large region. Coupling TDR instruments to each bi-wire of the network is clearly unfeasible.

Therefore, it is justified to investigate the possibility of employing an alternative and less expensive measurement methodology for the same SE's. In practice, such a methodology could be used to trigger an 'alert', which prompts further investigations involving more expensive and accurate TDR instrumentation.

Since the presence of water increases the dielectric constant of the medium surrounding the bi-wire, there are two major candidate methods. One method is based on the TDR technique itself, but does not require the high-speed sampling and A/D conversion typically associated with TDR measurements; basically, the idea is to measure the time of flight (ToF) of the signal propagating along the bi-wire [12]. ToF measurement can be accomplished using simple devices of limited complexity, based on fast comparators and clock counting hardware [34].

The second method consists in the measurement of the capacitance of the bi-wire, a cheap technique already used, for example, to determine its length [35]. As a matter of fact, at the state of the art, there are capacitance sensors for monitoring water presence or moisture content [36], and also sensors based on inductor-capacitor resonant circuits [37]; however, these are essentially point sensors, unlike the bi-wire SE. The capacitance of a bi-wire can be measured using a number of inexpensive methods, e.g. on the basis of the response to a single-tone sinusoidal signal, or with more complex impedance metering algorithms [38], or simply measuring the charge time with a DC current, or also the frequency it determines when put in an oscillating circuit, etc.

The paper examines the performance of the considered methods in terms of

- the (desired) sensitivity of ToF or capacitance to the presence of water; and
- the (undesired) sensitivity of ToF or capacitance to changes in the ambient conditions and, in particular, to temperature variations.

2.2 Preliminary theoretical analysis

The characteristics of the bi-wire used as SE in the present work are summarized in Table 2.1, whereas Fig. 2.1 shows its cross-section.

Before presenting and discussing experimental results, in this Section the sensitivity of the bi-wire to the presence of water, and to temperature variations, is analyzed theoretically. To this purpose, we make use of the notion of effective relative dielectric permittivity, which considerably simplifies electromagnetic equations in complex systems, e.g. multi-layer systems [39]. In the present case, a bi-wire surrounded by a coating with relative permittivity ϵ_c and a medium with relative permittivity ϵ_m is modeled as a couple of conductors surrounded by an homogeneous medium of (effective) relative permittivity ϵ_{eff} .

2.2.1 C and ToF variations with the presence of water

Consider a SE of length l_0 , where a portion of length Δl is immersed in a wetting medium (e.g. water), and the remaining portion, of length $l_0 - \Delta l$, is immersed in a "normal" medium (e.g. air). This configuration is schematized in Fig. 2.2. Let ϵ_{eff1}

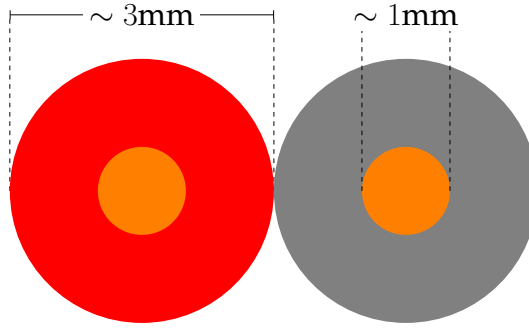


FIGURE 2.1: Simplified schematization of the cross section of the used bi-wires.

TABLE 2.1: AWG-18 electrical parameters.

Diameter	Cross-section area	Copper resistance	Nominal capacitance
1.024 mm	0.823 mm ²	20.95 Ω/km	50 pF/m

the effective relative permittivity of the dry portion of the SE, and ϵ_{eff2} the effective relative permittivity of the wet portion. The capacitance of a generic length l with effective relative ϵ_{eff} may be written as:

$$C = k \cdot \epsilon_0 \cdot \epsilon_{eff} \cdot l \quad (2.1)$$

where ϵ_0 is the absolute permittivity of vacuum, and k is an adimensional constant, which depends only on the geometry of the SE: for the geometry in Fig. 2.1, $\pi \operatorname{arccosh}(D/d)$ where d is the diameter of the conductors, and D the separation between the centers of the conductors. On the basis of (2.1), the total capacitance of the SE is given by:

$$C = k\epsilon_0[l_0\epsilon_{eff1} + \Delta l(\epsilon_{eff2} - \epsilon_{eff1})] \quad (2.2)$$

Therefore, the capacitance variation of the SE, due to the presence of the wetting medium, may be written as:

$$\frac{\Delta C}{C_0} = \alpha_C \frac{\Delta l}{l_0} \quad (2.3)$$

where C_0 is the capacitance of the dry SE (i.e. for $\Delta l = 0$), and α_C is a sensitivity coefficient, which is given by the relative variation of effective permittivity due to the wetting medium:

$$\alpha_C = \frac{\epsilon_{eff2}}{\epsilon_{eff1}} - 1 \quad (2.4)$$

A similar equation also applies for ToF variations. Under the hypothesis of non-magnetic dielectric materials, the velocity of an electromagnetic wave propagating in the SE is $v = c/\sqrt{\epsilon_{eff}}$, being c the speed of light in vacuum. The round-trip ToF,

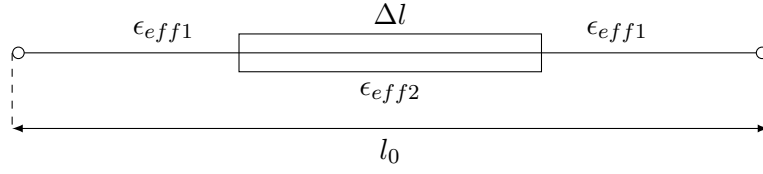


FIGURE 2.2: Schematization of the SE detecting the presence of a wetting medium surrounding a portion of length Δl . The quantities ϵ_{eff1} and ϵ_{eff2} are the effective permittivities when the wetting medium is absent or present.

τ , for a wave transmitted and reflected is

$$\tau = 2 \frac{l}{c} \sqrt{\epsilon_{eff}} \quad (2.5)$$

Therefore, the total ToF of an electromagnetic wave for the SE in Fig. 2.2 is given by

$$\tau = \frac{2}{c} \cdot [l_0 \sqrt{\epsilon_{eff1}} + \Delta l \cdot (\sqrt{\epsilon_{eff2}} - \sqrt{\epsilon_{eff1}})] \quad (2.6)$$

hence, the relative ToF variation due to the wetting medium is given by the following equation:

$$\frac{\Delta\tau}{\tau_0} = \alpha_\tau \frac{\Delta l}{l_0} \quad (2.7)$$

where τ_0 is the ToF in the dry SE, and α_τ is a sensitivity coefficient. The value of α_τ is the relative variation of the square root of the permittivity due to the wetting medium:

$$\alpha_\tau = \sqrt{\frac{\epsilon_{eff2}}{\epsilon_{eff1}}} - 1 \quad (2.8)$$

2.2.2 C and ToF variations with temperature

It must be considered that, since effective permittivities depend on temperature, also the actual values of capacitance and ToF will depend on it; as a result, temperature variations can mimic or mask the presence of a wetting medium. Let us consider a dry SE, and let us assume a linear variation of the effective relative permittivity ϵ_{eff1} with temperature:

$$\epsilon_{eff1}(T) = \epsilon_{eff1}(T_0)[1 + \alpha_T(T - T_0)] \quad (2.9)$$

The capacitance variation in the dry SE due to a temperature variation $\Delta T = T - T_0$ is:

$$\frac{\Delta C}{C_0} = \alpha_T \Delta T \quad (2.10)$$

while the ToF variation is

$$\frac{\Delta\tau}{\tau_0} = \sqrt{1 + \alpha_T \Delta T} - 1 \simeq \frac{\alpha_T}{2} \Delta T \quad (2.11)$$

In practical applications, in (2.11), the quantity $\alpha_T \Delta T$ is expected to be small; therefore, the first-order term should be dominant (generally, α_T is in the order of $0.01 \text{ } ^\circ\text{C}^{-1}$).

On the basis of the above equations, the sensitivity of the capacitance to temperature is about twice that of ToF. Since the temperature variation is a disturbance quantity, it appears that, from this point of view, ToF measurements should be preferred. On the other hand, when $\epsilon_{eff2} > \epsilon_{eff1}$, which is the situation of common practical interest, capacitance is more sensitive to the presence of the wetting medium ($\alpha_C > \alpha_T$).

2.2.3 Numerical computations and simulations

A more quantitative prediction of the behavior of the SE may be obtained with some further considerations and computations, necessary to obtain estimates of ϵ_{eff1} and ϵ_{eff2} . A specific problem that must be solved is that the relative permittivity ϵ_c of the coating is not declared by the manufacturer, who instead gives the capacitance of the wire in air (50 pF/m). Therefore, the workflow for the computations is as follows.

1. Computation of ϵ_{eff1} using (2.1), given the nominal capacitance per unit length, and the actual k derived on the basis of the SE's geometry.
2. Estimation of ϵ_c , using a COMSOL simulation. The SE's capacitance is evaluated by the simulation for different values of ϵ_c and with $\epsilon_m = 1$ (case of bi-wire in air). The value of ϵ_c yielding $C = 50$ pF/m is determined.
3. Estimation, using another COMSOL simulation, of C when the SE is immersed in water ($\epsilon_m = 80$) with the previously found value of ϵ_c .
4. Computation of ϵ_{eff2} from 2.1, using the capacitance value of the SE in water.

In order to assess the technique's sensibility in different practical conditions, step n. 3 has been performed by simulating different values of ϵ_m (in the [50,100] range) and with the SE surrounded by a cylinder of water with increasing diameter (in the range 0.5 - 20.0 cm).

In step n. 1, from the actual geometry of the SE ($d \simeq 1$ mm, $D \simeq 3$ mm) comes the value $k = \pi / \text{arccosh}(D/d) \simeq 1.782$, and therefore the capacitance per unit length of the conductors in vacuum (without the insulating coating) is $c_v = C_v/l = 15.78$ pF/m. Since the nominal capacitance of the dry SE is $C/l = 50$ pF/m, its nominal permittivity is $\epsilon_{eff1} = C/C_v \simeq 3.16$.

In step n. 2 the value of the coating permittivity ϵ_c which produces the capacitance $C/l = 50$ pF/m in the geometry of 2.1 was determined in the COMSOL Multiphysics environment; it is achieved by setting $\epsilon_c \simeq 5.7$. The results of step n. 3 and 4, in terms of the final effective relative permittivity $\epsilon_{eff2} = C/C_v$, are depicted in Fig. 2.3. They lead to the following considerations:

- The effective permittivity is substantially constant for volumes with cylindrical radius > 2 cm;

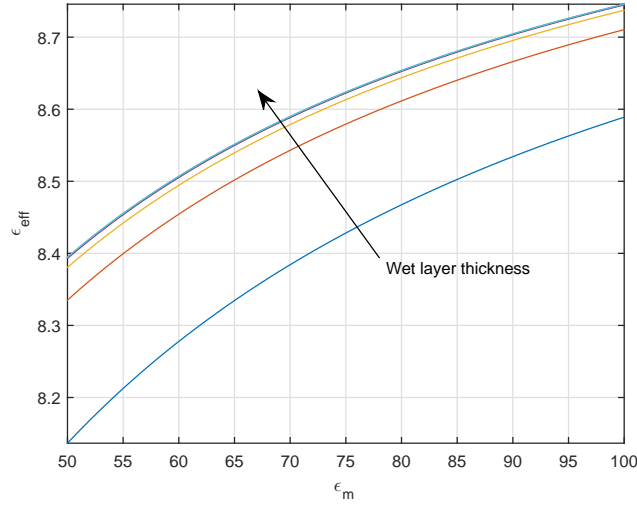


FIGURE 2.3: Effective relative permittivity ϵ_{eff} of the SE surrounded by a cylindric volume with given radius (0.5, 1, 2, 5, 10, 20 cm) and given permittivity ϵ_m (in the 50 - 100 range).

- For a medium with $\epsilon_m = 80$ (approximate permittivity of water) and radius > 2 cm, the resulting effective permittivity is $\epsilon_{eff2} = C/C_v \simeq 8.65$ (derived from the COMSOL computed capacitance value $C/l \simeq 132.47$ pF/m).

According to these computations, for the SE used in the simulations (which mimics that actually used in experiments) the ratio $\epsilon_{eff2}/\epsilon_{eff1}$ is approximately 2.74, and the sensitivity coefficients are $\alpha_C = \epsilon_{eff2}/\epsilon_{eff1} - 1 \simeq 1.68$ and $\alpha_\tau = \sqrt{\epsilon_{eff2}/\epsilon_{eff1}} - 1 \simeq 0.64$. As a consequence, even if the (undesired) sensitivity of the capacitance to temperature is twice that of ToF according to (2.11), the desired sensitivity to the presence of water is about three times that of ToF. On the basis of simulations, therefore, capacitance measurements appear slightly preferable.

This preliminary analysis yields only indicative conclusions about the actual sensitivity and usability of the SE. Rather than trying to obtain a more accurate characterization of the SE using full-wave simulations, in the following Sections an experimental study of the SE is reported.

2.3 Experimental setup

2.3.1 Measurement methods and instrumentation

All the tests were performed on a set of four bi-wires (devices under test - DUTs) with different lengths (l_0), namely 5 m, 10 m, 15 m and 20 m. The bi-wires are always left open-ended by simply cutting off their endings. The considered bi-wires exhibit an inductive behavior at high frequencies (in the order of a few megahertz) and a predominantly capacitive behavior at lower frequencies, as demonstrated in [40].

The capacitance measurements were performed using a portable capacitance meter (Escort EDC-128) equipped with a serial interface for data logging. This instrument operates on the principle of measuring the charging time of the DUT (a capacitor of 1 nF is measured by charging it for about 5 - 10 ms).

ToF measurements were performed using an arbitrary waveform generator (Agilent 33220A), which was used to generate a 100 kHz square waveform with a rise time $t_r \simeq 3.4$ ns, corresponding to a bandwidth $B \simeq 0.35/t_r \simeq 100$ MHz. This waveform was generated using the sync output rather than the signal output, since the rise time of the square waveform generated by the latter would have been higher (approximately 6.1 ns). The reflectograms were acquired using a 350 MHz-bandwidth digital oscilloscope (LeCroy LT262) in random interleaved sampling (RIS) mode. The equivalent sample rate was 50 GS/s.

In the set of experiments related to the assessment of the sensitivity to temperature, the temperature of the DUT was regulated using a simple hand-made ‘climatic chamber’, i.e. a thermally-controlled box (TCB) made of an insulating material (polystyrene) with a Peltier cell, used for both heating and cooling cycles, and a temperature control system implemented through the Arduino prototyping board. The TCB can provide temperature cycles ranging between 17 °C and 70 °C in about 40 minutes (both heat-up and cool-down rates). The TCB is controlled via a GUI written in C#, which exchanges information with the hardware through a serial port.

In the experiments, the ambient temperature (outside the chamber) was constantly measured and monitored through a Pt100 resistance temperature detector (RTD); whereas the temperature of the water and the temperature of the air in the chamber were monitored through two K-type thermocouples. The resistance of the RTD sensor and the voltages of the thermocouples were acquired through a multimeter (Agilent 34401A), in the 4-wire configuration for the resistance measurements.

2.3.2 Setup for Determining the Sensitivity to the Presence of Water

Starting at 1 m from the electrically accessible terminals, each bi-wire was attached to the inner wall of a 28 cm-high plastic container. Each bi-wire was positioned following a curvilinear path inside the container, as schematized in Figure 2.4.

As will be detailed later in this Chapter, the plastic container was progressively filled with water, in different steps. The bi-wire was positioned in the container so that a total length of 2.9 m would be subjected to watering, while the remaining cable was laid on the work bench. Ticks were traced on the container wall so that each addition-of-water step always wetted a prefixed length of the bi-wire. During these experiments, the ambient and the water temperatures were constantly monitored, and it was verified that their values were close to each other and approximately constant (within ± 1 °C) during the whole set of measurements. The ToF values were measured as the time intervals between the two rising edges of acquired reflectograms.

It is worth mentioning that the accurate estimation of the ToF from a TDR reflectogram is, in general, a non-trivial issue [41] [42], which, indeed, is not the focus of

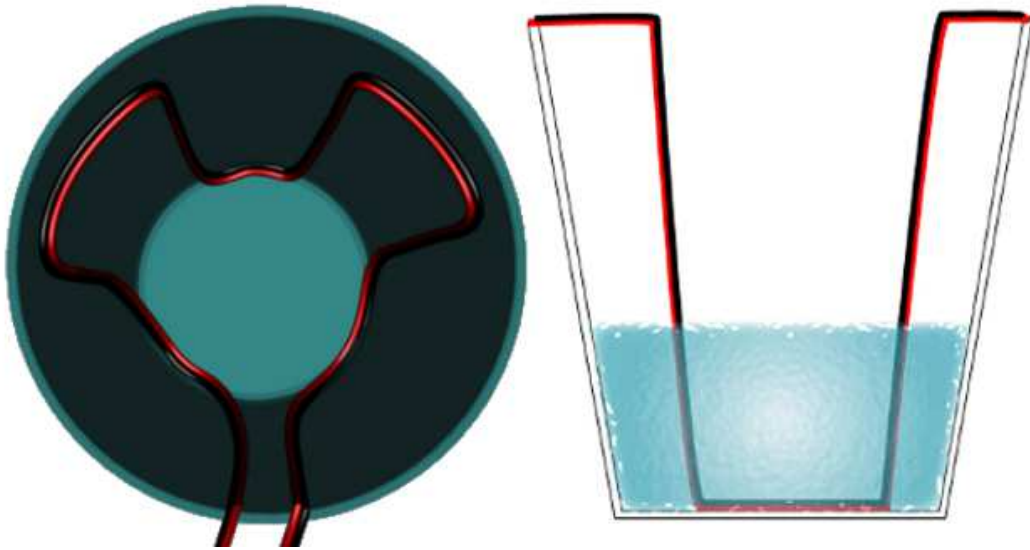


FIGURE 2.4: Sketch of the positioning of the bi-wire inside the container: top view (*left*) and lateral cross section (*right*).

the problem analyzed in this Chapter. For our purposes, however, locating the rising edges using pre-established thresholds on the reflectograms is as good as using other, more sophisticated methods.

Finally, with regards to the capacitance measurements, the capacitance values were acquired directly from the EDC-128, without further data-processing.

2.3.3 Setup for Determining the sensitivity to temperature variations

In this set of experiments, each dry bi-wire was rolled up in order to fit into the TCB, as shown in Fig. 2.5.

During each test, a 1 m-long portion of bi-wire, with the electrically accessible terminals, was intentionally left outside. The temperature in the TCB was raised with an approximately linear law, from 25 °C to 45 °C in approximately 15 minutes. The ToF and the capacitance of the dry bi-wires were measured continuously while the bi-wires were subjected to the temperature variation.

2.4 Experimental results for the sensitivity to the presence of water

To quantify the sensitivity to the presence of water, the ToF and the capacitance of the bi-wire were measured, with the setup described in Section 2.3.2. In particular, water was added to the container five times, once every 300 seconds (i.e. 5 minutes), for a total 30 minutes. After the first watering step, the length of the wetted portion of bi-wire was $\Delta l = 0.67$ m. The wetted length increased by 0.32 m on each successive watering step (up to a total wetted length of $\Delta l = 1.95$ m).



FIGURE 2.5: Positioning of the bi-wire in the thermally-controlled box (TCB).

Measurements were performed on all four DUTs and, for each DUT, the ToF and the capacitance values during watering operations were acquired. Two typical measurement runs for capacitance and ToF are shown in Fig. 2.6 and Fig. 2.7, respectively. The ambient and the water temperatures are also reported, showing that their variation is practically negligible during these experiments. On a side note, it is worth mentioning that in both Figure 2.6 and Figure 2.7, the water temperature is missing from the first 300 s long portions of the plot, because water had yet to be added.

2.4.1 Capacitance measurements

Measured capacitance values are summarized in Table 2.2, where the quantity Δl indicates the length of the wetted portion of bi-wire.

First of all we focus on the measurements on dry bi-wires (first row of the table). Not surprisingly, the measured values of capacitance follow a law of the kind

$$C_m = c_0 \cdot l_0 + C_{\text{off}} = C_0 + C_{\text{off}} \quad (2.12)$$

where c_0 is the capacitance per unit length, and C_{off} is a positive offset error, due to the instrument and to parasitic effects in the setup (connection cables, etc.). Linear fitting on the measurements yields $C_{\text{off}} = 89.7$ pF and $c_0 = 65.9$ pF/m, with a difference between measurements and model (2.12) lower than 0.65 %.

After subtraction of the offset C_{off} from the data in Table 2.2, the capacitance variations (ΔC) due to the wetting of the bi-wires are expected, of course, to follow the proportional law described by (2.3) in Section 2.2. As a matter of fact, measurement results fit better a slightly different model, i.e.

$$\Delta C = C(\Delta l) - C_0 = \alpha_C \cdot \frac{\Delta l}{l_0} [C_0 - C_p]. \quad (2.13)$$

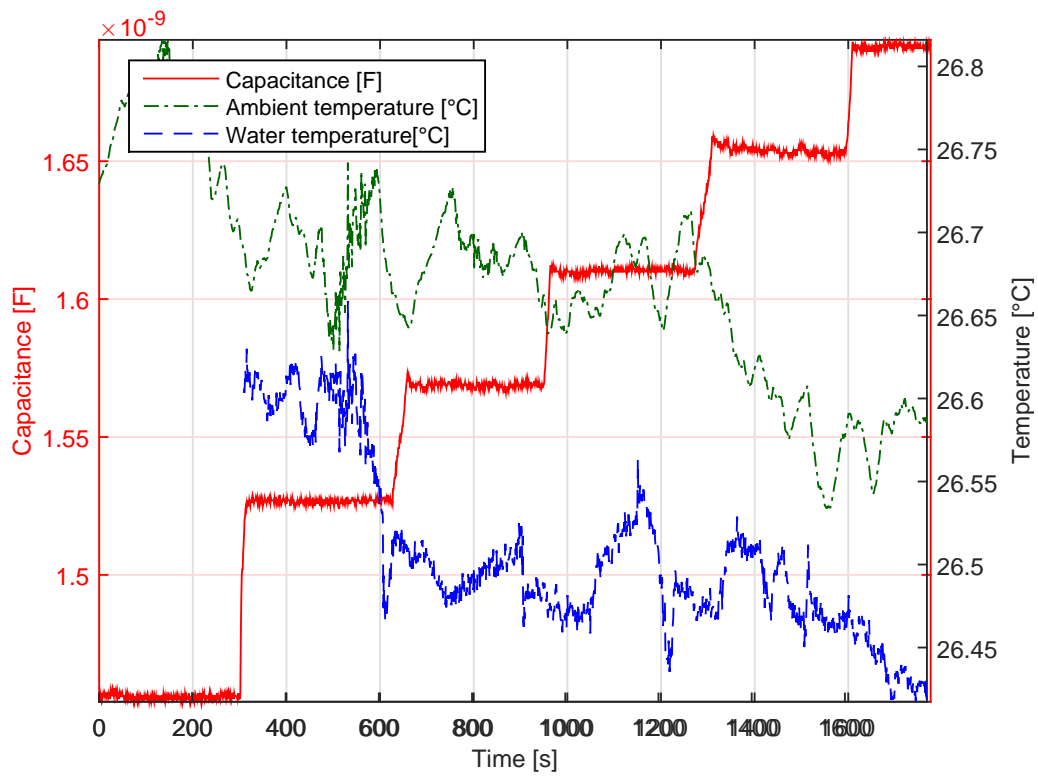


FIGURE 2.6: Capacitance measurements for the 20 m-long bi-wire, water addition every 300 seconds (left vertical axis). The behavior of the ambient and of the water temperatures is also reported (right vertical axis).

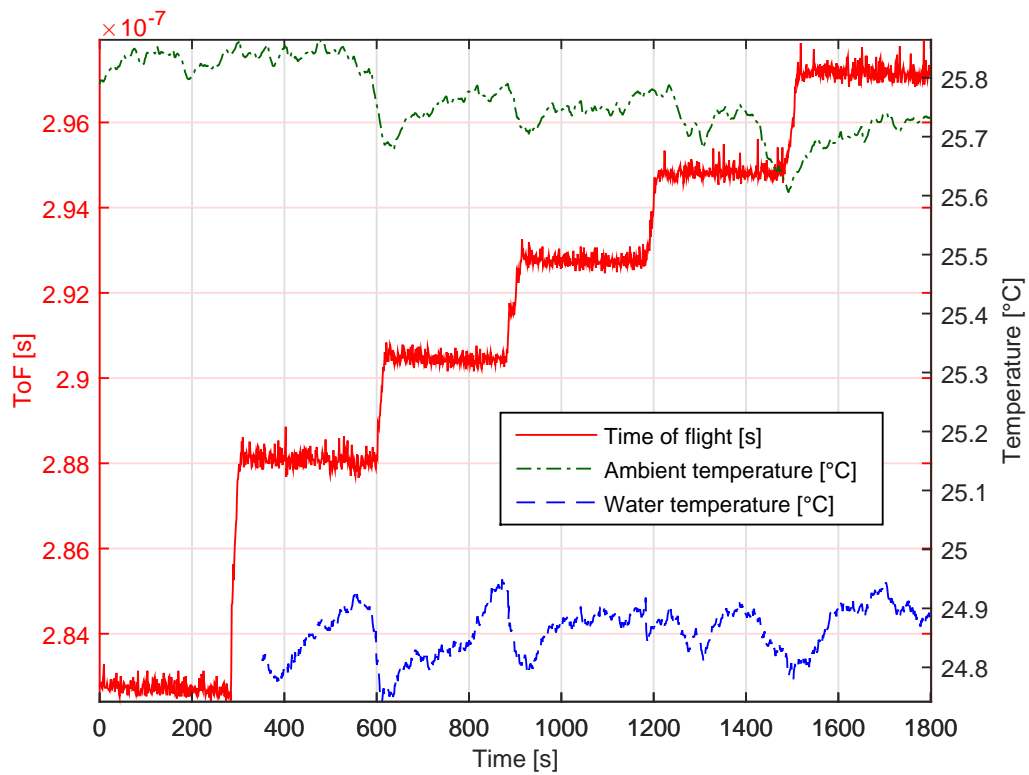


FIGURE 2.7: Time-of-flight measurement for the 20 m-long bi-wire (water addition every 300 seconds). The behavior of the ambient and of the water temperatures is also reported.

TABLE 2.2: Measured capacitances (C) for different lengths (l_0) of the bi-wire and for different wetted lengths (Δl).

Δl [m]	C [pF] ($l_0 = 5$ m)	C [pF] ($l_0 = 10$ m)	C [pF] ($l_0 = 15$ m)	C [pF] ($l_0 = 20$ m)
0	420.2	744.0	1084	1405
0.67	470.0	808.0	1139	1471
0.99	499.0	842.0	1168	1510
1.31	535.0	873.0	1203	1544
1.63	563.0	898.0	1232	1572
1.95	598.0	935.0	1270	1607

From a physical point of view, C_p represents a capacitance quota which is not influenced by water (related, for example, to the portion of the bi-wire that were intentionally left outside the container). The model described by (2.13) is nonlinear in the parameters α_C and C_p ; therefore, these parameters were evaluated through a nonlinear fitting procedure on the data, obtaining

$$\begin{aligned}\alpha_C &= 1.5675 \\ C_p &= 50.87 \text{ pF}\end{aligned}$$

It can be observed that the obtained sensitivity value agrees with theoretical computations and numerical simulations reported in Section 2.2 (in particular, equation (2.4)), and confirmed by the numerical simulations discussed in Section 2.2.3. The comparison between measurement results and the fitted model is shown in Figure 2.8, where it can be seen that the obtained values for α_C and C_p provide an excellent fitting for each considered bi-wire length, l_0 . The maximum fitting error occurs for $l_0 = 15$ m and is $C_{err} = 15$ pF. One can also invert (2.13) in order to estimate the wet length from the measured capacitances. Maximum estimation errors resulting from the application of (2.13) are 10 cm for the 5 m-long bi-wire and 9 cm for the 20 m-long bi-wire.

Equation (2.13) also allows assessing the minimum length of wetted bi-wire that can be detected for a given resolution of a capacitance meter. For instance, if $C_0 \gg C_p$, a resolution of 10 pF allows sensing approximately 10 cm of wet bi-wire.

2.4.2 Time of flight measurements

Measured ToFs values are summarized in Table 2.3. Also in this case, first of all we focus on the measurements on the dry cables (first row of the table), which follow the linear model:

$$\tau_m = s_0 \cdot l_0 + \tau_{off} = \tau_0 + \tau_{off} \quad (2.14)$$

where τ_{off} is an offset error and s_0 is a time per unit length, of course related to the propagation velocity by the relationship $v_0 = 2/s_0$ (the factor 2 being due to the round-trip of the e.m. wave). Fitting the model to the measurements yields an offset error $\tau_{off} = 80.30$ ns and a time per unit length $s_0 = 10.43$ ns/m, corresponding to a propagation velocity of the test signal in the bi-wire equal to $v_0 = 0.639 \cdot c$, where c

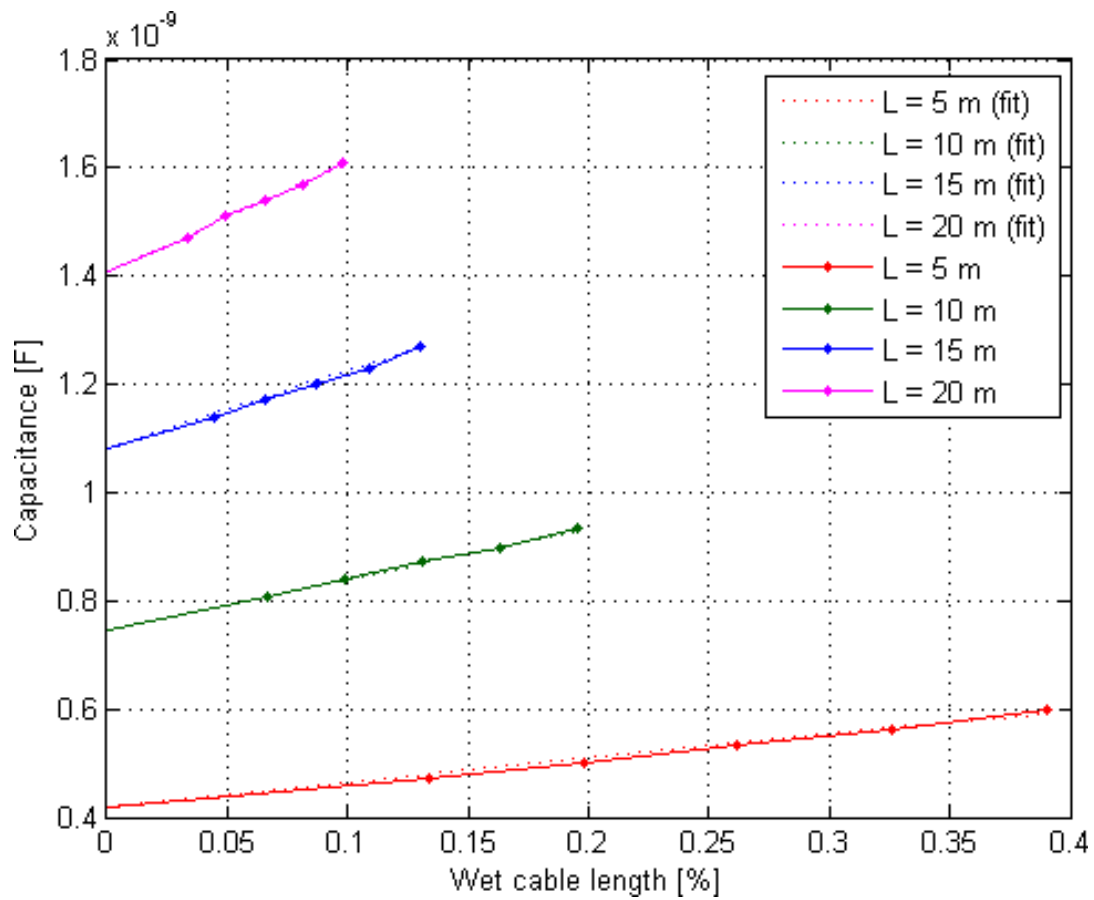


FIGURE 2.8: Measured and fitted values of the capacitance (C), as function of relative wet length ($\Delta l/l_0$).

TABLE 2.3: Measured ToFs for different lengths (l_0) of the bi-wire and for different wetted lengths (Δl).

Δl [m]	ToF [s] ($l_0=5$ m)	ToF [s] ($l_0=10$ m)	ToF [s] ($l_0=15$ m)	ToF [s] ($l_0=20$ m)
0	6.038E-08	1.118E-07	1.648E-07	2.165E-07
0.67	6.430E-08	1.165E-07	1.683E-07	2.215E-07
0.99	6.616E-08	1.182E-07	1.700E-07	2.235E-07
1.31	6.770E-08	1.204E-07	1.711E-07	2.247E-07
1.63	6.940E-08	1.214E-07	1.727E-07	2.250E-07
1.95	7.092E-08	1.231E-07	1.754E-07	2.271E-07

is the speed of light in vacuum. The fitted model reproduces the data with a relative error below 0.5%.

As a second step, the offset value was subtracted from the data and the result fits very well a model similar to (2.13):

$$\Delta\tau = \tau(\Delta l) - \tau_0 = \alpha_\tau \cdot \frac{\Delta l}{l_0} [\tau_0 - \tau_p] \quad (2.15)$$

where $\tau(\Delta l)$ is the ToF measured for a Δl wet length of bi-wire, while τ_p is a constant, which may be interpreted as a ToF quota which is not influenced by the presence of water. The values of α_τ and τ_p were evaluated through a nonlinear fitting on the measurement data:

$$\begin{aligned} \alpha_\tau &= 0.5415 \\ \tau_p &= 0.26 \text{ ns} \end{aligned}$$

Also in this case the measured α_τ is very close to the expected theoretical value, predicted from equation (2.8). The quality of this fitting operation is shown in Figure 2.9, which clearly shows that the two parameters α_τ and τ_p are characteristic of the ToF variation, and are independent of the total length of the bi-wire. The maximum fitting error is of 1.4 ns, occurring for $l_0 = 20$ m.

Similarly to the capacitance measurements, (2.15) can be inverted in order to estimate the wet length of the bi-wire from the measured ToFs. The maximum estimation errors are 8 cm and 25 cm, for the 5 m long bi-wire and for the 20 m-long bi-wire, respectively. They are slightly higher than those associated to the use of the capacitance model (2.13).

Equation (2.15) also allows evaluating the minimum wet length of bi-wire that can be detected for a given resolution of a ToF-measuring instrument. For example, if a bi-wire is long enough to ensure that $\tau_0 \gg \tau_p$, a resolution of about 800 ps for the ToF measurements allows sensing wet length of bi-wires that are at least 10 cm.

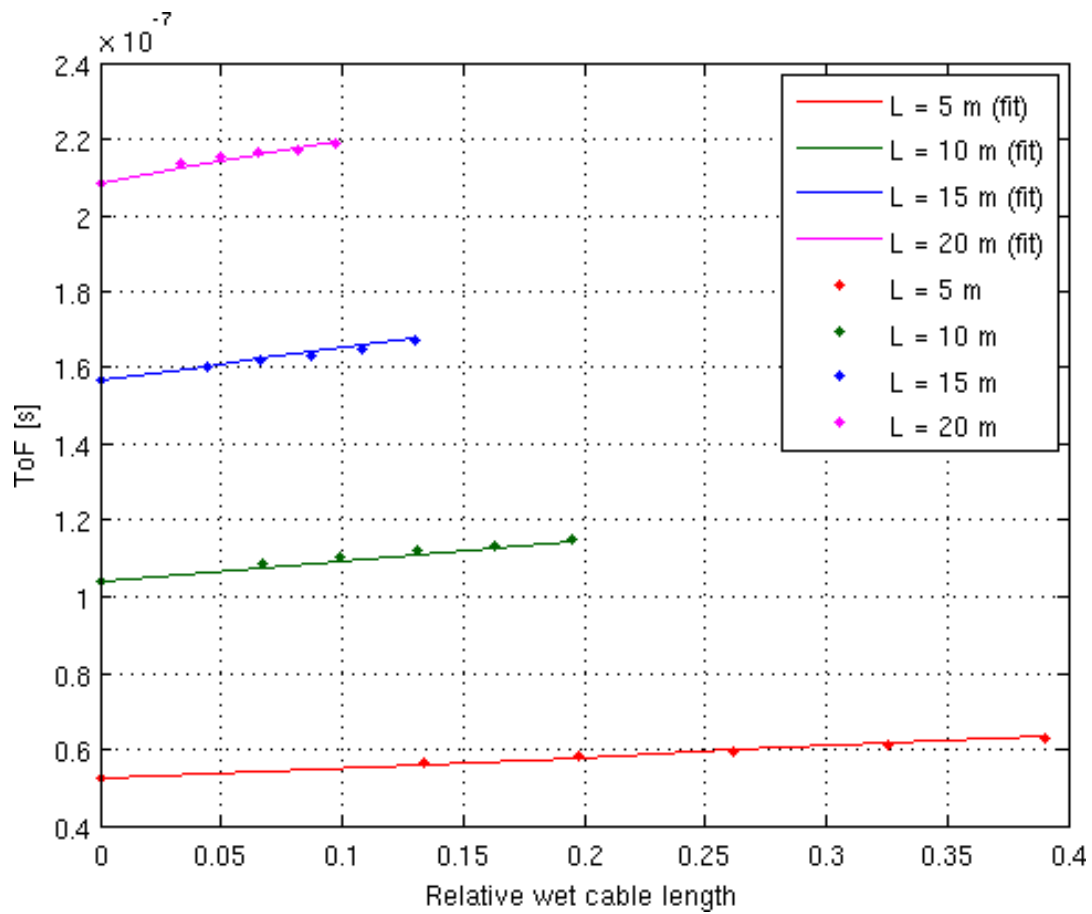


FIGURE 2.9: Measured and fitted ToF values as function of relative wet length ($\Delta l/l_0$).

2.5 Sensitivity to temperature variations

As described in Section 2.3.1, the DUTs were tested with controlled thermal cycles in a thermostated box, thus controlling the box internal temperature. During these tests, also the ambient temperature was monitored so as to verify that its variations (which affect the instruments) were below 1 °C. In this set of experiments, the measurement results consisted of some thousands of temperature-capacitance and temperature-ToF couples; therefore, they are reported only in graphical form.

2.5.1 Capacitance measurements

In principle, the same operation of offset removal described in section 2.4.1 could be applied to capacitance measurements with varying temperature. However, this post-correction is not needed, since, in this case, the goal is to quantify the effect of temperature variations as a disturbance (and not to measure temperature on the basis of the capacitance). Therefore, the simplified model (2.10) for ΔC can be used to fit the experimental data.

Figure 2.10 shows the very good agreement between measurements and the fitted model: it can be seen that there is a very good agreement between the measurements and the model. It also shows that the sensitivity coefficient α_T is actually different for the four examined cases: it ranges from $\alpha_T = 0.0015^\circ\text{C}^{-1}$ for $l_0 = 5$ m to $\alpha_T = 0.0046^\circ\text{C}^{-1}$ for $l_0 = 20$ m. The different sensitivity to temperature may be attributed to the fact that longer cables were wound. In other words, the different amassing of the coils for the different tested bi-wires leads to different sensitivity to temperature.

This outcome of the experiments points out that the sensitivity of the capacitance to temperature in the practical use of the bi-wire as a sensor is not accurately predictable, since it will be partly determined by the actual dielectric surrounding the wire. On the other hand, the sensitivity can be expected to be in the same order of magnitude obtained in the reported experiments, i.e., of the order of 0.001-0.005 °C⁻¹.

2.5.2 Time-of-Flight measurements

The same considerations made for capacitance apply to ToF measurements. The main difference between ToF and capacitance, as regards the sensitivity to temperature variations, is that data can be fitted better by using a quadratic law:

$$\frac{\Delta\tau}{\tau_0} = A \cdot \Delta T + B \cdot \Delta T^2 \quad (2.16)$$

The result of the fitting is shown in Figure 2.11. Also in this case, the actual values of A and B are different in the experiments with different bi-wire lengths, and the 20 m long bi-wire is the most sensitive to temperature variations, while the 5 m long bi-wire is the least sensitive. These results are in agreement with those obtained for the capacitance, and the same explanation apply: the plastic dielectric surrounding each portion of the wire is greater in the experiments with the 20 m-long bi-wire.

Even if the law is quadratic, and not linear, the ToF sensitivity to temperature is lower than that of the capacitance: the maximum ToF variation is in the range 1%-4.5%, while that of the capacitance is in the 3%-9% range. The lower sensitivity of ToF to temperature, with respect to capacitance, is in agreement with theoretical predictions.

2.5.3 Effect of temperature on water sensing

The capacitance method is more sensitive both to the presence of water and to temperature variations, with respect to the ToF method. Therefore, it is not immediately clear which of the two methods is less affected by temperature, in terms of false water detection. For quantifying the influence of temperature on water sensing, it is possible to compute the apparent fraction of wet length emulated by a given temperature variation. For the capacitance-based method, the apparent fraction of wet cable is

$$\frac{\Delta l}{l_0} \cong \frac{\alpha_T}{\alpha_C} \Delta T \quad (2.17)$$

while for the ToF-based method, this fraction is

$$\frac{\Delta l}{l_0} \cong \frac{A}{\alpha_\tau} \Delta T + \frac{B}{\alpha_\tau} \Delta T^2 \quad (2.18)$$

Considering the difference between a linear law and a quadratic law, it is intuitive that the ToF method can be preferred for small temperature variations, while the capacitance-based method is preferable for larger variations. This fact is better detailed in the next Section.

2.6 Discussion of results

On the basis of the obtained results, both methods are able to detect the presence of water, but they have different advantages and drawbacks. With the ToF method, the measurement hardware must be equipped with a fast clock. For example, in order to detect 10 cm of wetted bi-wire, it must be able to resolve a time variation of about 800 ps, and considering a clock period equal to half the required resolution, the minimum clock frequency is approximately $f = 2.5$ GHz.

With the capacimetric method, the measurement hardware does not need to meet exceptionally strict requirements. In order to detect 10 cm of wetted bi-wire, one must be able to resolve a capacitance variation of about 10 pF. However, it must be underlined that the relative capacitance variation (with respect to the capacitance of the dry wire) depends on the overall length of the SE. For example, for a 20 m long bi-wire, the relative capacitance variation is about 7.5%, while for a 100 m long bi-wire the variation is only 1.5%.

As regards the possibility of false or missed detections due to temperature variations, the two methods are comparable, the preference going to the ToF method for low temperature variations (10 °C or less), and to the capacimetric method for

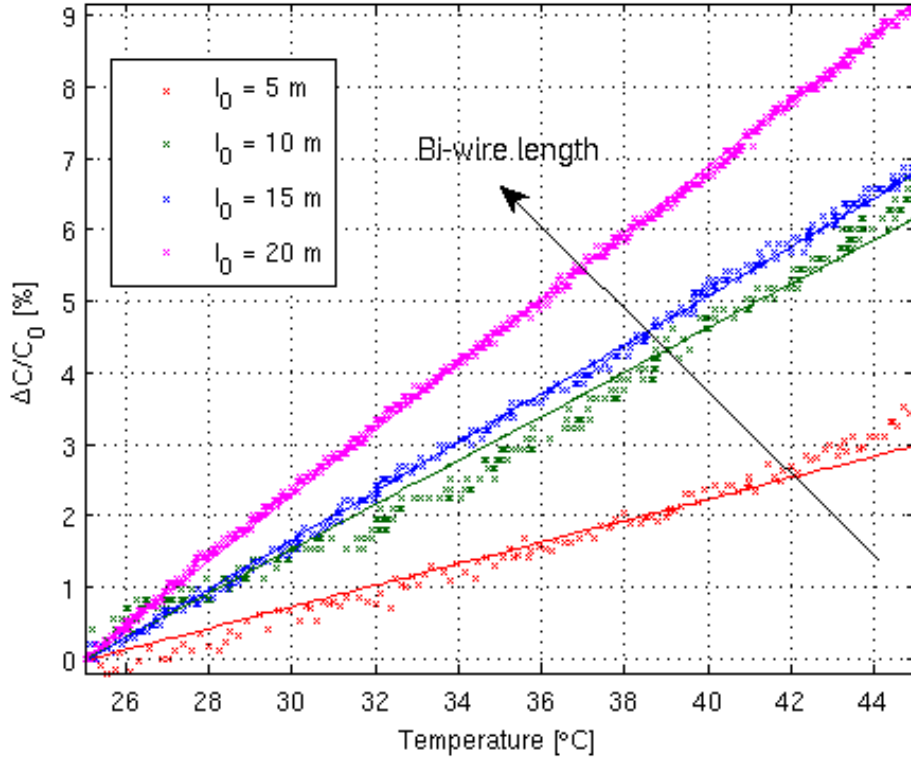


FIGURE 2.10: Percentage capacitance variation as function of temperature for different lengths of the bi-wire.

higher temperature variations. This statement is justified by the experimental results in Figures 2.10 and 2.11, and by equations 2.17 and 2.18 that fit the measurement data. In particular, for a 20 m long cable, a temperature variation $\Delta T = 10^\circ$ C causes an apparent wet cable fraction $\Delta l/l_0 \simeq 3\%$ with both the capacimetric and the ToF method. Since 2.17 is a linear and 2.18 a quadratic law, it is obvious that for $\Delta T < 10^\circ\text{C}$ the ToF method suffers less influence from temperature, while for $\Delta T > 10^\circ\text{C}$ the capacimetric method is less influenced. Therefore, considering the influence of temperature, capacimetry can be recommended for applications with greater expected temperature variations. It is, in any case, advisable to use bi-wires at most few tens of meters long, since the sensitivity to temperature variations becomes an important effect for longer wires, e.g. 100 m long or more.

2.7 Conclusions

Bi-wires can be used as SE's for water detection purposes, measuring the variations of the capacitance, or of the propagation velocity of electric pulses. The advantage of employing this type of SE is twofold: they are very inexpensive, and they can sense water in a continuous path that can be several meters long.

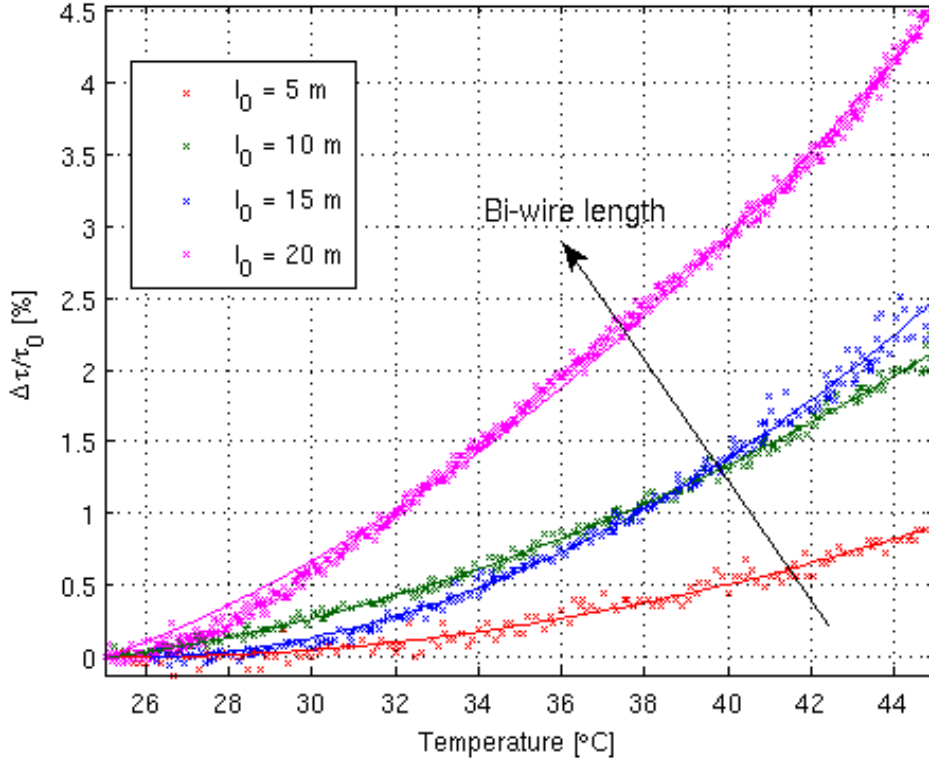


FIGURE 2.11: Percentage ToF variation as function of temperature for different lengths of the bi-wire.

Starting from these considerations, after a preliminary theoretical analysis, actual experiments were performed using bi-wires (in different lengths) in conjunction with the aforementioned measurement methods, thus characterizing the SE in terms of sensitivity to the presence of water. Furthermore, also the influence of temperature variations on the performance of the SE was investigated.

The obtained results demonstrate that, in view of possible practical implementation of diffused water-detection systems, the proposed low-cost methodologies could be used to trigger an alert regarding the monitored system and to prompt further, more accurate control using more expensive TDR instrumentation. In practical implementations, the great advantage would be that the concept can be extended to complex systems, with a distributed network of sensing elements, thus allowing to monitor large areas in real time.

The measured sensitivities agree with theoretical predictions made through numerical simulations, presented in Subsection 2.2.3 and, in particular, it was demonstrated that capacitance measurements on bi-wires are approximately three times more sensitive than ToF measurements:

$$\begin{cases} \alpha_C \simeq 1.57 \\ \alpha_\tau \simeq 0.54 \end{cases} \quad (2.19)$$

It is important to emphasize that capacitance metering is also simpler to implement using inexpensive and largely available hardware for very accurate measurements [43]. The results open the way to the development of a simple capacitance meter tailored to the proposed SE, and of a fully-featured water presence alert system for multipurpose environmental diagnostic systems.

Chapter 3

Time-of-Flight estimation from TDR waveforms

I ask people who don't fly, "How can you not fly when you live in a time in history when you can fly?"

WILLIAM LANGEWISCHE

3.1 Introduction

In Chapter 2, two simple and cost-effective techniques for quickly monitoring the presence of anomalies in distributed systems without actually performing TDR measurements have been compared. Although such techniques employ the same sensing elements as TDR setups, they can be considered standalone, since they do not necessarily rely on actual reflectograms. However, if TDR instrumentation is already available, there is no need to implement Time-of-Flight measurements on a standalone basis, since now full TDR waveforms can be acquired and ToF can be directly derived from them.

In TDR, the ToF indicates the time it takes for a test signal to travel a certain distance through a medium. The evaluation of the ToF in TDR measurements is essential for a number of applications. One of the first TDR-based applications, which is the localization of faults in electrical cables, strongly relies on measurements of the ToF; in fact, the ToF of the TDR test signal up to the defect or fault is used to infer the position of the fault [44], [45].

Furthermore, measurements of the ToF of TDR signals are at the basis of applications in several fields, such as leak detection in underground water pipes [46], real-time monitoring of the flow and the liquid level in intravenous medical infusions [1], crack/strain sensing in reinforced concrete structures [47], and dielectric characterization of liquids [48], [49].

However, in spite of the widespread use of TDR, the accurate measurement of the ToF is still an open issue [50], [51]. As a matter of fact, the estimation of the ToF has always been considered one of the major sources of uncertainty in TDR measurements. The traditional waveform analysis has used the fitting of tangent lines to the waveform reflection to determine the travel time [52]–[54]; this travel time is related to the signal phase velocity.

Successively, Robinson et al. [6] argued that it is more appropriate to calculate the ToF from the apices of the derivative of the waveform. In their work, the medium under test is strictly divided into homogeneous segments and experimental conditions are rigorously controlled, and therefore the $S_{11}(f)$ scattering parameter can be evaluated using the recursive schemes proposed by Feng et al. ([6], eq. (6)), together with Cole–Cole equations, for each individual segment. These conditions are verified, e.g., when measuring the dielectric constant of a perfectly homogeneous medium by a purposely designed TDR probe. In [6], in fact, the importance of high quality probe construction and the importance of minimizing long cables are stressed.

In [55], on the other hand, an algorithm for wire integrity analysis in helicopters, tiltrotors, and aircrafts is considered. In this case, the probe consists of a wire running through an arbitrarily inhomogeneous medium. Moreover, faults can be wire to wire and wire to shield, generating waveforms that usually need to be interpreted by experienced personnel; finally, faults can be irregular. For such cases, simple derivative algorithms will not suffice in detecting the correct fault [55]; the proposed algorithm is therefore completely different (with some features in common with stock market analysis).

The authors are, instead, interested in a class of TDR applications that stands, in some way, in between those considered in [6] and [55]. These applications require the development of cost-effective sensing and monitoring TDR systems, often involving the impossibility to strictly control every single parameter [1], [8], [22], [46].

Starting from these considerations and from the results reported in [42], the goal of this Section is to demonstrate the performance of different derivative-based methods for the estimation of ToF in simple TDR signals like those encountered in [1], [8], [22], [46].

In fact, it is worth mentioning that the presented criteria can be particularly useful in applications such as TDR-based water-level measurements [8] or TDR-based localization of leaks in underground water pipes [22]. In fact, one of the goals of this paper is to pave the way for the implementation of fully automated algorithms that could improve the accuracy and efficiency in TDR waveform analysis.

For this purpose, three different criteria for ToF estimation using the derivative of reflectograms are compared, namely:

1. Maximum derivative (MD)
2. Zero derivative (ZD)
3. Tangent crossing (TC).

For a comparison of the algorithms, a large set of measurements was carried out on cables with different lengths (from 10 cm to 30 m) and with known electrical parameters. The accuracy of the methods is evaluated in terms of systematic (gain, offset, and nonlinearity) and random errors (repeatability) in the presence of noise. For the study hereby presented, step-like signals have been used as stimuli in TDR measurements.

After briefly illustrating the error model for the proposed estimation technique, a general description of the methods is carried out. The accuracy of the three criteria in terms of gain, offset, and nonlinearity errors is examined, and a discussion of algorithm robustness in the presence of noise is carried out. Furthermore, the performance of the three considered criteria is checked on twin leads with known length and unknown electrical parameters and finally the presented criteria are applied to water level measurements as test application, and their performance is assessed.

In a first set of experiments, the three criteria, referred to as maximum derivative (MD), zero derivative, and tangent crossing (TC), are applied to TDR signals propagating along a set of coaxial cables, with different known lengths and electrical parameters. In a second set of experiments, the same criteria are applied to twin leads in air, with different known lengths and unknown electrical parameters. Finally, in the last set of experiments, the criteria are applied in a more complex situation, i.e., on a twin lead used as a sensing element for water-level measurement.

The results show that, among the tested criteria, TC appears to provide a very good performance in terms of systematic errors and superior performance in terms of repeatability. The popular MD criterion appears to be more prone to random errors due to noise and TDR artifacts. The results hereby presented are relevant to many practical applications of TDR, ranging from fault location in cables to media interface sensing.

3.2 Signal preconditioning and error model

From a practical point of view, the accuracy of the ToF measurement can be identified with the following:

1. Length measurement accuracy (for cables with known propagation velocity)
2. Velocity measurement accuracy (for cables with known length)
3. linearity and repeatability of the calibration curve, in a ToF-based measurement (e.g., water-level measurement)

It is common to characterize the accuracy of length measurements with its absolute error, i.e., the difference between the estimated length and its real value. In this Section, the performance of each criterion is assessed by evaluating gain, offset, and nonlinearity error components.

The estimated lengths are fitted to a straight line in the least squares sense, giving the following error model:

$$l(l_0) = (1 + er_G)l_0 + e_O + e_{nl}(l_0) \quad (3.1)$$

where l_0 is the real length and l its estimated value. The meaning of the parameters in (3.1) is given as follows:

er_G Relative gain error (mismatch between the slope of the fitted straight line and unity)

e_O Offset error (y-intercept of the fitted straight line)

$e_{nl}(l_0)$ Integral nonlinearity error (difference between measured lengths and fitted straight line)

From a practical point of view, offset error is associated with the goodness of the agreement between the estimated and the true cable length, and gain error is related to a multiplicative factor that proportionally alters all measured lengths.

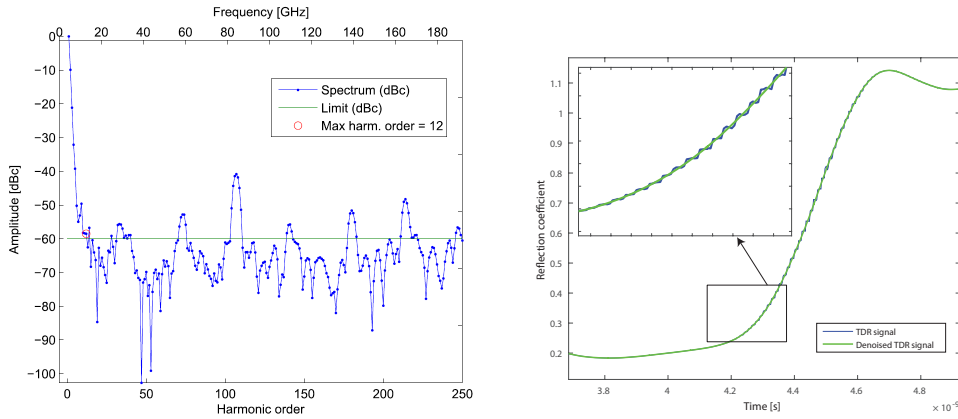
Since the three criteria considered in this paper are based on the direct analysis of the first derivative of the signal, it is important to be able to accurately compute it. The simple finite difference approximation is too sensitive to noise in most practical cases, and therefore, a denoising technique is necessary.

In [56], it was demonstrated that wavelet-based denoising methods, using empirically chosen thresholds, optimally adapt the denoised signal to the signal that must be recovered. However, the wavelet denoising technique is particularly case dependent and, although providing excellent results [57], needs to be fine-tuned for each combination of test signal and acquisition instrumentation adopted. In order to avoid complex and case-dependent fine-tuning, Nicolson's technique [58] together with high order harmonics filtering has been used for denoising, with the approach already adopted in [22]. This denoising technique can be briefly outlined as follows:

1. Signal detrending
2. Fast Fourier Transform (FFT)
3. High-order harmonics suppression (3.1(a))
4. Frequency domain derivative evaluation
5. Inverse FFT (3.1(b))

Such a filtering routine eliminates noise without introducing undesired filter-dependent ripple, and it also enhances peaks in the derivative, which, indeed, are not detectable in the finite difference derivative approximation. Moreover, this technique excellently performs against noise without introducing any delay in relevant features. Figure 3.1 shows typical denoising results and, in detail, one of the signal peaks, whose position in time is unchanged between the original noisy signal and its denoised version.

Step 3 includes rough low-pass filtering, by simple high order harmonics suppression. The specific harmonic order to be chosen is not a critical issue, since with Nicolson technique, any reasonably low harmonic order works very well against noise while preserving required signal features. Therefore, the results that will be reported have been achieved by filtering harmonics under a reasonably chosen noise floor (-60 dBc). Furthermore algorithms have also been tested against different harmonic orders in terms of repeatability.



(a) Harmonic thresholding of detrended reflectogram (b) Denoised reflectogram in the time domain

FIGURE 3.1: Reflectogram denoising with Nicolson's technique

3.3 Materials, methods and measurement protocols

As aforementioned, the algorithm and the ToF estimation criteria were tested on real reflectograms (rather than on synthesized ideal reflectograms). In fact, although it would have been easier to synthesize ideal reflectograms and test, for example, the noise robustness of each criterion, it is clear that measured reflectograms exhibit unpredictable TDR-related features, e.g., limited rise time of the test signal, artifacts in the test signal, oscillations in the reflectogram due to multiple reflections, different slopes between the two rising edges, amplitude noise, and sampling jitter. A synthetic reproduction of such features and effects would be largely arbitrary.

A brief descriptions of the experimental setup and the three considered criteria for the estimation of the ToF follow.

3.3.1 Experimental setup for measurements on cables with known parameters

In the first experimental setup, the reflectograms have been acquired using a Campbell Scientific TDR100 reflectometer. It provides a 250 mV step-like signal in an output impedance of 50Ω , with nominal time response of combined pulse generator and sampling circuit ≤ 300 ps. In order to work in low-noise conditions, signal averaging was also applied (128 averages per reflectogram). Such a measurement configuration guarantees reliable, clean, and stable reflectograms, suitable for characterizing the systematic errors of the algorithms. These experiments have been performed on coaxial cables (terminated in OC), whose nominal EM propagation velocity is $0.83c$, being c the velocity of light in void. Other electrical parameters of the DUTs are detailed in Table 3.1. After assessing gain, offset, and nonlinearity errors, measurement repeatability has also been assessed by adding white noise to acquired waveforms and applying different filtering depths.

TABLE 3.1: DUT electrical parameters

Parameter	Value
Type	Coaxial
Impedance	75 Ω
Propagation velocity	0.83 c
Attenuation @10 MHz	3 dB / 100 m
Attenuation @ 1 GHz	26.1 dB / 100 m

Successively, to verify the robustness of the developed methodology, additional tests were performed on twin leads (also terminated in OC), with unknown electrical specifications. For this class of experiments, test signals with a rise time of $\simeq 4$ ns were generated using an arbitrary waveform generator (80-MHz Agilent 33250A) and reflectograms were acquired using a LeCroy LT262 350-MHz oscilloscope in random interleaved sampling mode. The authors have used instrumentation with poorer performance in order to demonstrate the performance of the developed algorithms in a more cost-effective environment.

3.3.2 Experimental setup for water level measurement application

The algorithms were tested on a typical ToF-related practical application, namely, TDR-based water-level monitoring [8]. The schematic of the setup is shown in Figure 3.2. A biwire was inserted into a graduated transparent cylindrical container. A 1 m long RG-58 coaxial cable was used to connect the beginning of the biwire to an arbitrary waveform generator (80-MHz Agilent 33250A). This waveform generator was used to apply a 100 kHz square-wave test signal to the biwire under test. In this configuration, water was progressively added into the container, with a consequent increase in the water level. As reported in [8], in such a configuration, the biwire acts as a sensing element (or probe) for TDR-based measurements of the level of water inside the container. Since the container was graduated, after each water addition step, the resulting true water level could be measured by eye.

On a side note, it is worth mentioning that the choice of the interconnection scheme described above was purposely made to introduce an impedance mismatch between the signal source and the biwire under test, which may be accurately located using the presented automatic processing algorithm, and will be also thoroughly discussed in the following Sections.

3.3.3 Time-of-Flight estimation criteria

The value of the ToF is estimated as the time interval between two critical points detected on the reflectogram, which conventionally identify rising and/or falling edges on the signal. These points of interest (POIs), as anticipated in Section 3.1, are detected according to different criteria (Figure 3.3): 1) MD; 2) ZD; and 3) TC.

The first criterion identifies the signal edges with the absolute maximum of the derivative in the rising region, meaning the maximum for rising edges and the minimum for falling edges. The second criterion identifies the edges with the last zero

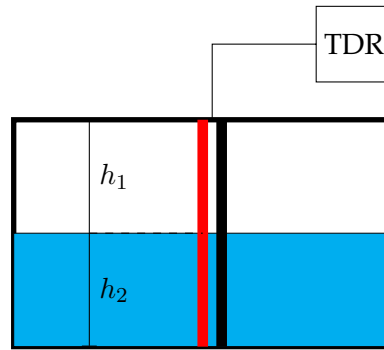


FIGURE 3.2: Sketch of the experimental setup for water level measurement

crossing of the derivative before the MD point. In other words, it is used to identify the leading edge of the test signal. Finally, the third criterion, as simple and widespread as the first, models the rising edge as a smoothed ramp and identifies the crossing of the tangents to the reflectogram for the MD and ZD points.

The three criteria have different features listed as follows.

1. The MD criterion evaluates the ToF on the basis of maximum energy points of the pulses, and it is essentially linked to the group velocity
2. The ZD and TC criteria evaluate the ToF on the basis of the leading edges of the pulses, and they are essentially linked to the phase velocity of the faster sinusoidal component
3. By their definitions, it follows that $t_{ZD} \leq t_{TC} \leq t_{MD}$
4. Since the MD point is the rightmost, and can never fall before the knee of the step-like pulse, it will overestimate more often than underestimate the ToF; the contrary happens for the ZD point
5. By simple geometric considerations, the TC point is more stable near the knee of the pulse, and in the case of overestimation by MD and underestimation by ZD, it represents a convenient tradeoff.

3.4 Experimental results and repeatability study

3.4.1 Measurements on cables with known propagation velocity

As mentioned in Section 3.3, preliminary tests were performed on coaxial cables with known propagation velocity. Measurements were performed on three sets of cable:

1. 0.1 - 0.5 m
2. 1 - 5 m

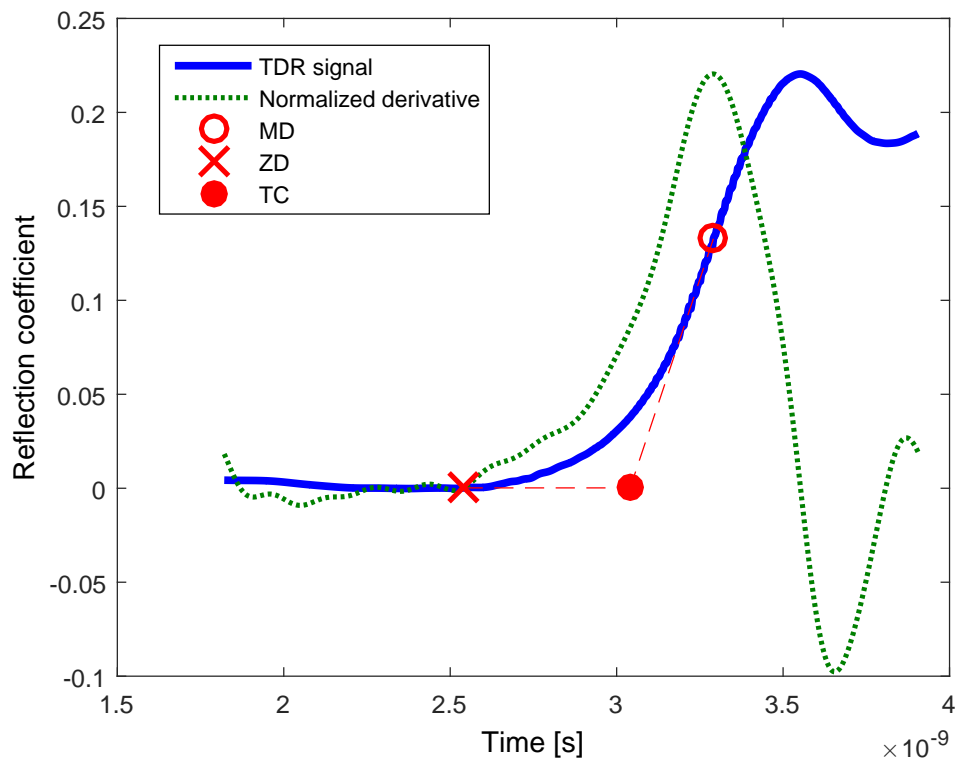


FIGURE 3.3: Rising edge of the reflectogram acquired on a 15 cm long coaxial cable, its derivative, and POIs.

TABLE 3.2: Gain, Offset and Nonlinearity errors in the estimation of cable length with the three considered criteria

		0.10 - 0.50 m	1.00 - 5.00 m	10.00 - 30.00 m
e_O [cm]	<i>Max derivative</i>	-0.475	-0.559	0.081
	<i>Zero derivative</i>	3.433	1.675	2.027
	<i>Tangent crossing</i>	0.387	0.328	0.994
er_G [%]	<i>Max derivative</i>	1.125	0.395	0.143
	<i>Zero derivative</i>	-2.522	0.122	0.143
	<i>Tangent crossing</i>	0.284	0.328	0.141
$\max e_{nl} $ [cm]	<i>Max derivative</i>	0.28	0.29	0.28
	<i>Zero derivative</i>	2.13	2.40	2.27
	<i>Tangent crossing</i>	0.27	0.41	0.59

TABLE 3.3: Propagation velocity estimated with the three considered criteria (nominal velocity: $0.83c$)

		0.10 - 0.50 m	1.00 - 5.00 m	10.00 - 30.00 m
$\frac{v}{c}$	<i>Max derivative</i>	0.8208	0.8267	0.8288
	<i>Zero derivative</i>	0.8515	0.8290	0.8288
	<i>Tangent crossing</i>	0.8276	0.8273	0.8288

3. 10 - 30 m

Each set encompassed nine cables of linearly spaced lengths, except for the last one, which had five linearly spaced lengths. Measured reflectograms from two sets of cables are shown in Figure 3.4.

Every reflectogram shows reflections of different nature: the first is weaker, determined by the mismatch between the interconnection cable and the cable under test ($50 \sim 75 \Omega$), and the other is stronger, determined by the open circuit termination. Since cable lengths of largely different values ranging from 10 cm to 30 m have been considered, different phenomena such as edges of different steepness and multiple reflections are visible.

The performances of the considered criteria are summarized in Table 3.2, which shows offset, gain, and nonlinearity error contributions in detail.

It must be highlighted that gain error depends on the propagation velocity, which is given by the manufacturer with no further uncertainty specification. Propagation velocity, however, can also be estimated from ToFs and true lengths and compared with its nominal value for the purpose of criteria testing. Such velocity measurements are reported in Table 3.3, showing an excellent agreement with the manufacturer specifications.

As regards gain, offset, and nonlinearity errors, the best performing criteria are clearly MD and TC, the latter performing significantly better for short cables. From the results in 3.3, on the other hand, the best performing criterion for propagation velocity estimation is TC. In fact, it allows an estimation of the propagation velocity with a 0.14% error with respect to its nominal value.

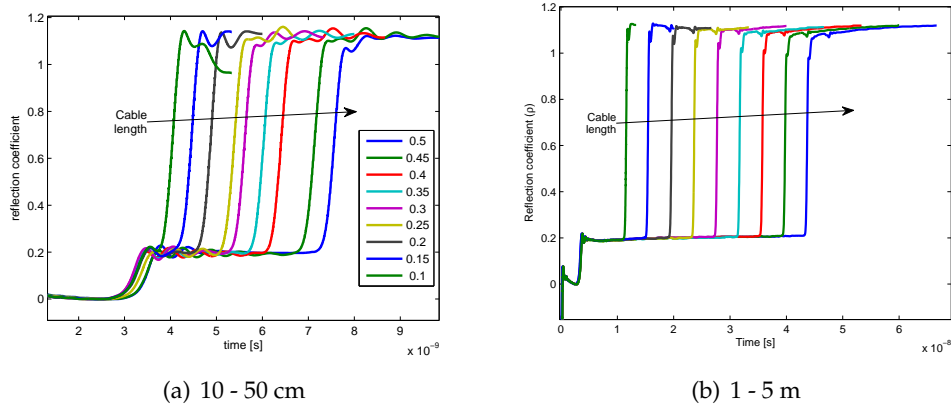


FIGURE 3.4: Measured reflectograms for different cable lengths

3.4.2 Repeatability study

Repeatability assessment has been performed by considering six cable lengths among the full set of DUTs previously described. One hundred realizations of white noise have been summed to each reflectogram, and afterward, the three criteria have been applied to noisy signals. Noise standard deviation has been reasonably chosen as 0.5% of the entire reflectogram span. An example of the resulting noisy reflectograms is reported in Figure 3.5. The bias and standard deviation of the estimated cable lengths have been evaluated as a function of filtering depth (harmonic order). Some explanatory results are shown in Figures 3.6 and 3.7 for the shortest (10 cm) and the longest (30 m) cables respectively, considering harmonic orders from 10 to 20. Here the bias values are, for the sake of clarity, expressed by representing the average estimated cable lengths and the real cable length, reported as a horizontal dashed line.

Figures 3.6 and 3.7 show that the TC algorithm outperforms the other two in terms of repeatability (standard deviation of the estimates) and also has very good bias properties. TC, therefore, can be, at this step, considered the most robust among the tested criteria.

Other noise standard deviations in a range up to 1% of the reflectogram span have also been tested, always achieving the results similar to those reported in this Section.

3.4.3 Measurements on cables with unknown electrical parameters

Additional measurements have been performed on biwires with an AWG-18 inner conductor, with unknown electrical specifications, in the range 5 – 30 m. These cables are of particular interest because of their good sensitivity to changes in the dielectric constant of the surrounding environment, which makes them suitable in many sensing applications [46].

The results are summarized in Table 3.4, and er_G was not computed since the true value for propagation velocity was not available. Also in this case, the TC criterion

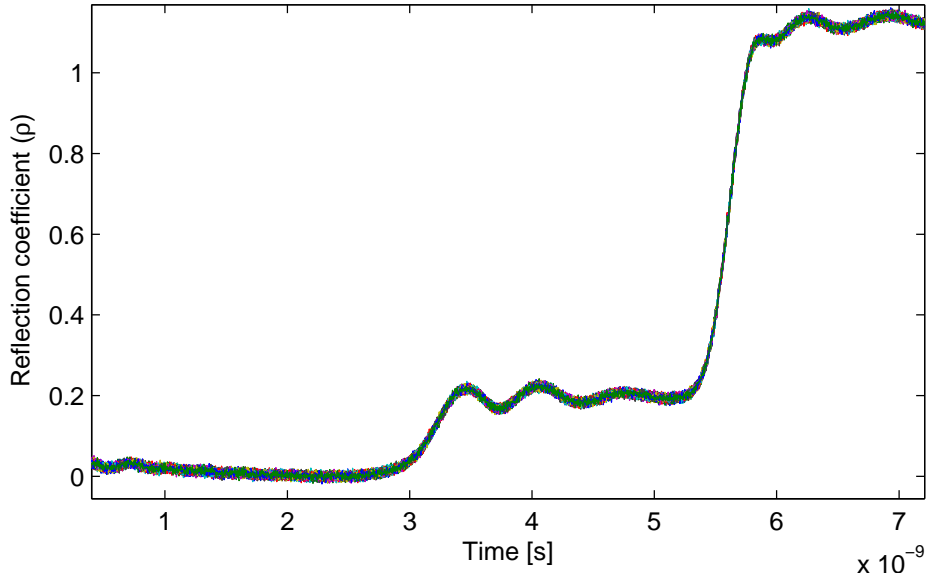
FIGURE 3.5: Set of 100 noisy reflectograms ($l = 30$ cm)

TABLE 3.4: Gain, Offset and Maximum errors in the estimation of the length of biwires with the three considered criteria

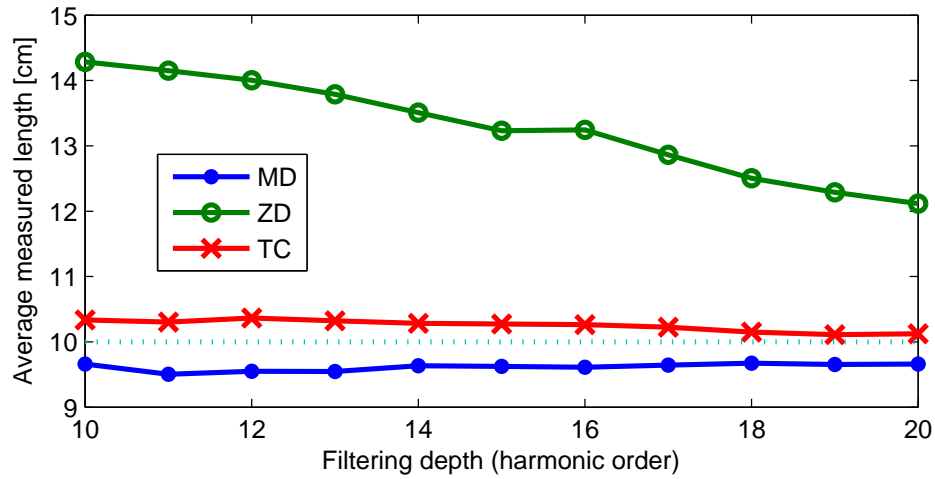
	Max Derivative	Zero Derivative	Tangents Crossing
er_G	N/A	N/A	N/A
e_O	-25.10 cm	-25.61 cm	-10.68 cm
$\max e_{nl} $	48.94 cm	15.73 cm	12.66 cm
v/c	0.6379	0.6591	0.6558

appears to have better performances in terms of offset and maximum nonlinearity error.

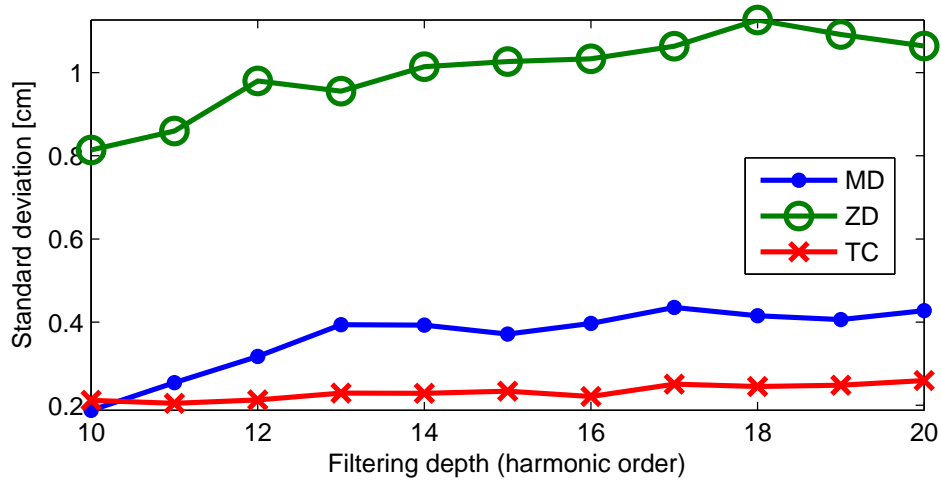
Propagation velocity values were also computed from the estimated ToFs. Such values demonstrate that the three criteria behave in the same way on two different kinds of DUTs: (i) the lowest value for propagation velocity is estimated with MD and (ii) the highest one comes from the ZD, TC standing in the middle.

3.5 Test application: water level measurement

In order to test the three presented criteria in a different application scenario, they were comparatively used for TDR-based water-level measurement [1], [10], with the experimental setup described in Section 3.3. The coaxial interconnection between the biwire and the instrumentation introduces an impedance mismatch between the signal source and the actual probe, which may be accurately located using the presented processing algorithms, as shown in Figure 3.8.

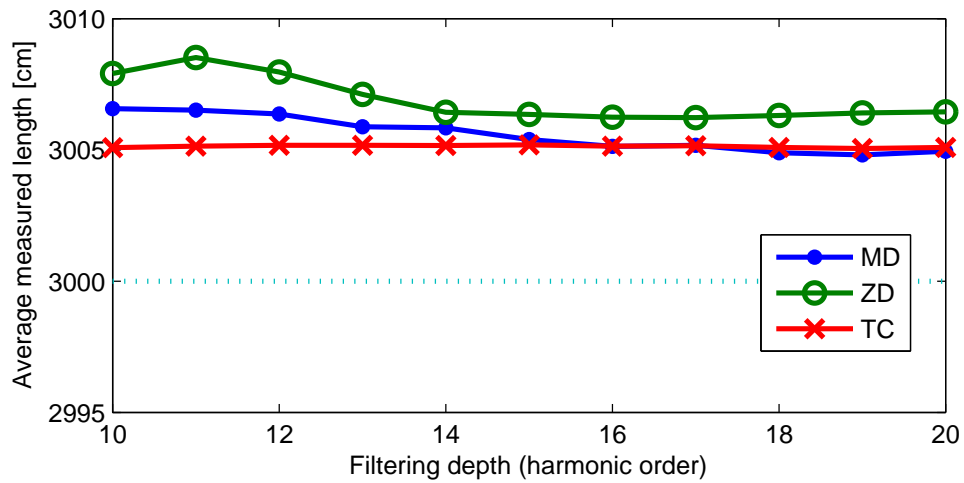


(a)

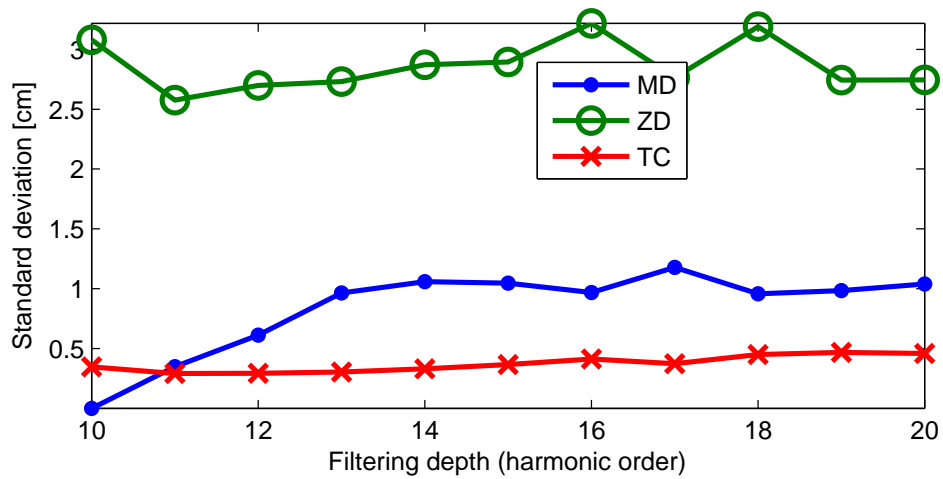


(b)

FIGURE 3.6: Repeatability analysis for a 10 cm long cable in terms of average measured length (a) and standard deviation (b)



(a)



(b)

FIGURE 3.7: Repeatability analysis for a 30 m long cable in terms of average measured length (a) and standard deviation (b)

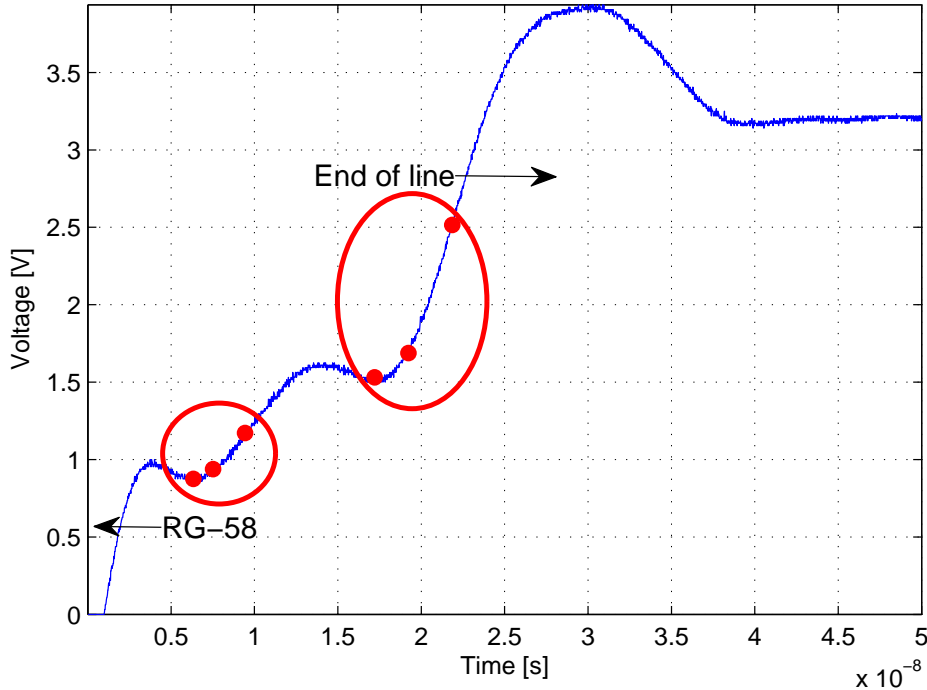


FIGURE 3.8: TDR (step-like) signal on a completely dry probe

The two sets of features depicted with dots represent the beginning and the end of the biwire under test according to the three criteria (ZD, TC, and MD, respectively). When a certain fraction of the biwire length is submerged in water, a discontinuity in the effective dielectric permittivity of the medium surrounding the probe occurs. Therefore, another impedance mismatch becomes clearly visible in the reflectogram, thus enabling the algorithm to detect another set of features, as shown in Figure 3.8. In the Figure, the variation in the position of the detected features with regard to the increase in the wet length is also pointed out. Going from the leftmost feature set toward the last on the right, the algorithm has been used to detect the following:

- The interface between the coaxial cable and the biwire
- The air–water interface on the biwire
- The end of the biwire.

3.5.1 Analytic ToF model for two layered materials

In the proposed experimental setup, the test signal has to travel twice the length of the biwire, which is surrounded by two different media with their respective ϵ_{eff} values, which represent the effective dielectric constant seen by the traveling wave.

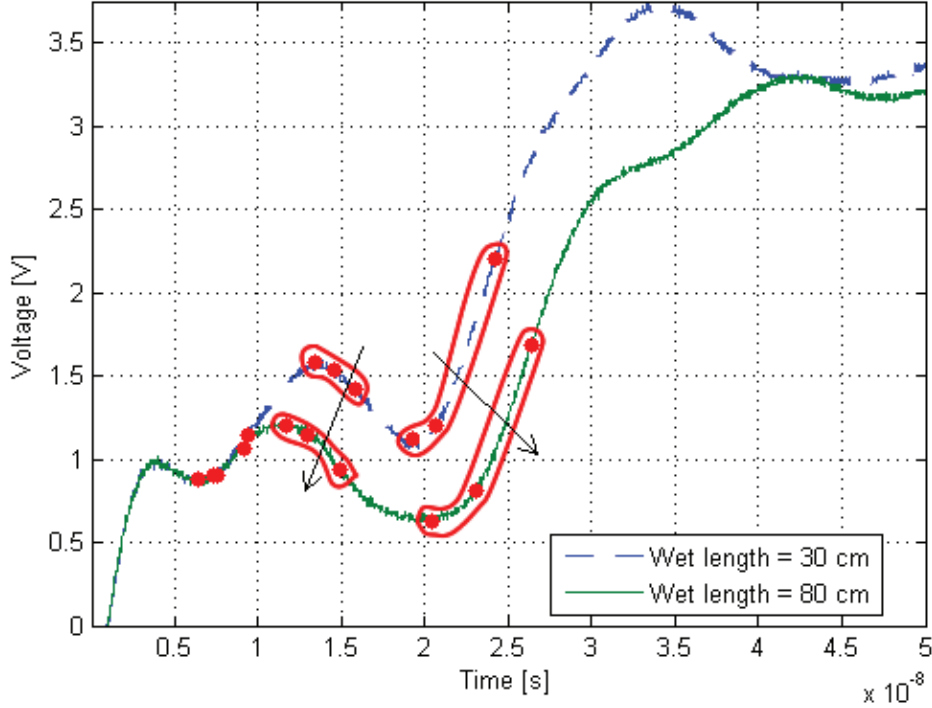


FIGURE 3.9: TDR (step-like) signal on a wet probe

With respect to this simple model, the overall propagation time in each media can be computed as follows:

$$\tau_1 = 2 \frac{h_1 \sqrt{\epsilon_{eff1}}}{c}; \quad \tau_2 = 2 \frac{h_2 \sqrt{\epsilon_{eff2}}}{c}; \quad (3.2)$$

where h_1 and h_2 are the biwire lengths surrounded by the first and second media, respectively (as in Figure 3.2), the factor 2 takes into account the round trip, $c/\sqrt{\epsilon_{eff1/2}}$ is the propagation velocity in each medium, and c is the propagation velocity in void. Therefore, the total propagation time in the biwire is given by

$$\tau = \tau_1 + \tau_2 = \frac{2}{c} [h_2 (\sqrt{\epsilon_{eff2}} - \sqrt{\epsilon_{eff1}}) + l \sqrt{\epsilon_{eff1}}] \quad (3.3)$$

where l is the total length of the biwire ($l = h_1 + h_2$).

Equation (3.3) is clearly linear with respect to h_2 , meaning that measuring τ should provide an excellent benchmark for the three ToF estimation criteria.

3.5.2 Experimental design

For this specific application, the set of experiments has been designed as follows:

1. TDR measurements have been performed in order to construct calibration curves, with confidence intervals quantifying the repeatability

2. TDR measurements were performed by raising the water level at intervals of about 5 cm and acquiring 100 reflectograms per level
3. True water-level values were directly read on the cylindrical container, which was graduated at 1 mm steps. The reading error can, therefore, be neglected
4. All the measurements were performed in a period of time of the order of a few minutes, with ambient temperature between 24 °C and 26 °C and with ambient humidity between 50% and 55%
5. The quantity affecting the measurement repeatability is essentially the instrumentation noise. Other influence quantities have been kept practically constant during the experiments
6. The obtained calibration curves are valid for the ambient conditions specified above and for the specific instrumentation used, with its metrological characteristics (especially in terms of frequency response and rise time)
7. Calibration curves, e.g., for other values of temperature should be obtained with separate calibration experiments.

3.5.3 Water level measurements as ToF estimation benchmark

In Figure 3.10, measured calibration curves for each presented criterion are comparatively plotted.

The results in Table 3.5 reproduce and confirm those of Section 3.4 regarding the reliability and robustness of the TC criterion.

The best performing criterion appears to be TC because of better linearity all over the considered wet length range. The ZD criterion shows a similar performance in terms of linearity; nevertheless, its linearity is impaired for greater wet lengths. The reason of ZD criterion performance degradation is due to the flattening of the reflectogram in correspondence with high wet lengths (as shown in Figure 3.11), which makes ZD unreliable. From a qualitative point of view, the excellent performance of the TC criterion is a direct consequence of using information coming from the other two examined criteria to achieve, overall, a greater robustness.

The 100 repeated measurements have been used to compute the 95% confidence levels reported (red dotted lines) for the TC calibration curve (Figure 3.12) and summarized in Table 3.5.

The overall results indicate, finally, that the MD of the signal is the information of a comparatively poor value if used alone; on the contrary, it leads to the best and most robust results if merged with the ZD information, i.e., into the TC criterion. This is observable in nearly ideal situations (coaxial cables and twin cables in air) and is particularly clear in less ideal situations (sensing applications). It is therefore an excellent candidate for many TDR measurement applications.

TABLE 3.5: Nonlinearity errors for each criterion

	Max Derivative	Zero Derivative	Tangents Crossing
$\max e_{nl} $ [ns]	1.0176	1.0041	0.4716
Sensitivity [ns/cm]	0.0686	0.0300	0.0584
2σ [ns]	1.3703	1.1143	0.1905

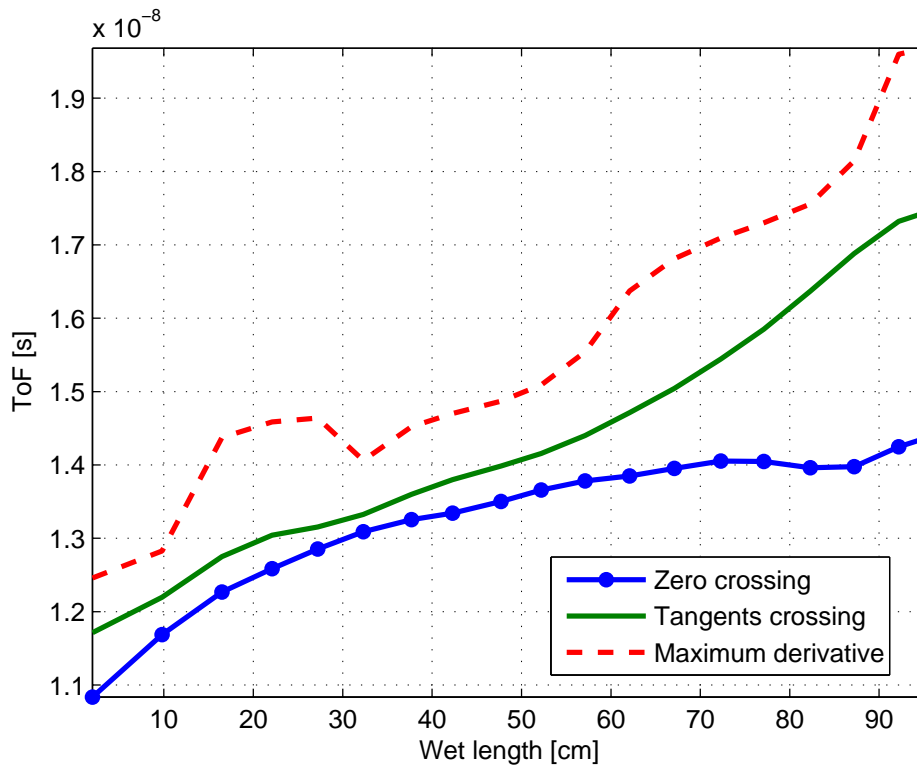


FIGURE 3.10: ToF versus wet biwire length: compared calibration curves

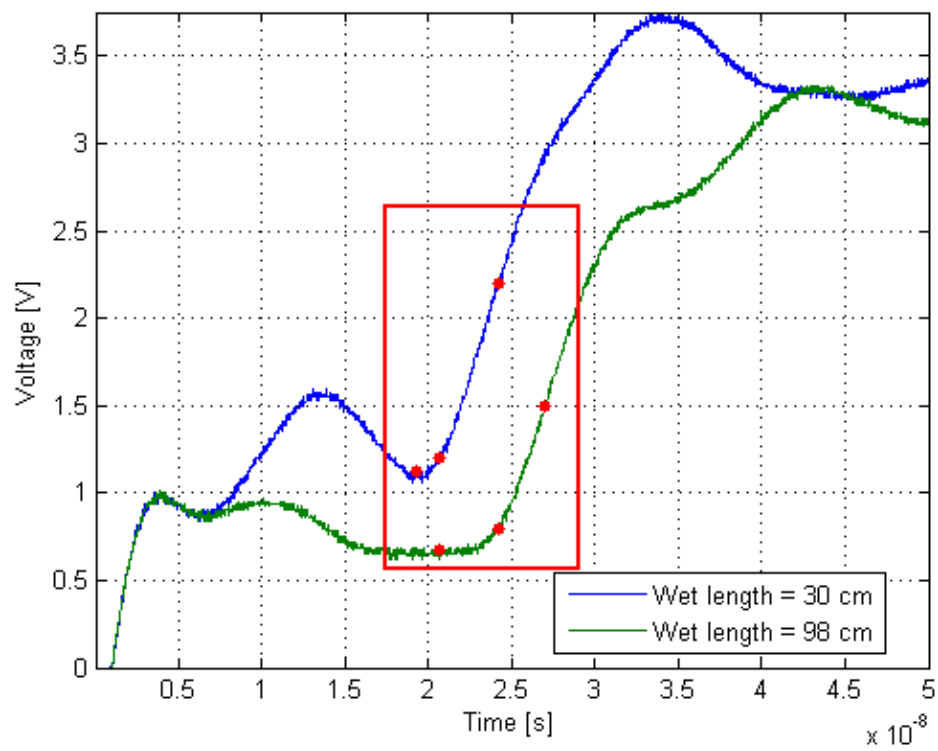


FIGURE 3.11: Reflectogram flattening in presence of high wet lengths

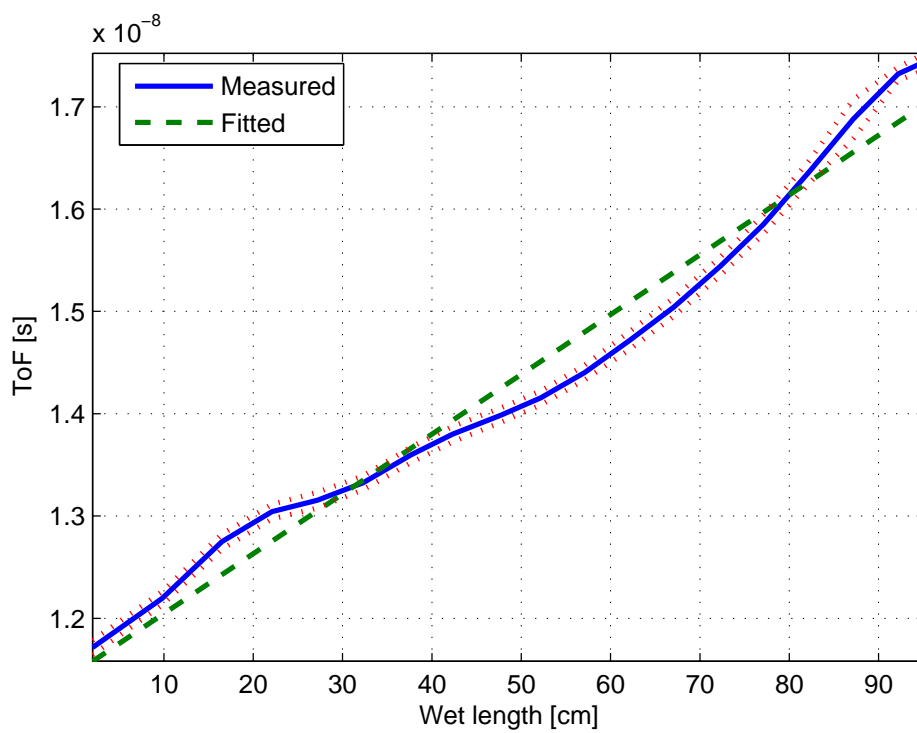


FIGURE 3.12: Water level measurement calibration curve for the TC criterion

Chapter 4

Theoretical background and TL simulation algorithms

Transmission line theory bridges the gap between field analysis and basic circuit theory [...] As we will see, the phenomenon of wave propagation on transmission lines can be approached from an extension of circuit theory or from a specialization of Maxwell's equations

DAVID POZAR

4.1 Introduction

In this Chapter the fundamentals of Transmission Line theory will be briefly recalled paying particular attention to their application in the context of the simulation of TDR systems and, finally, a custom made simulation algorithm, tailored for the simulation of TDR systems will be presented. TL theory is, in fact, an extremely powerful framework that embeds realistic and physically sound modeling tools in circuit theory [59] that is easy to implement in lightning-fast simulation software.

As stated in Chapter 1, in fact, building an accurate and effective model of the TDR measurement setup is crucial to be able to extract all needed information from TDR waveforms, that is reconstructing model parameters. In other words, connecting Transmission Line theory to TDR probe design and/or characterization is the first step to achieve a simplified model with its set of parameters.

Focusing on the ultimate problem, that is simulating the most general cases of TDR measurements (e.g. [1], [2], [4], [5]), it must be considered that the main characteristic of these systems is that the primary parameters are not constant along the TL, but are an arbitrary function of the position, which means that a Finite Elements algorithm is required. Moreover, the losses in dielectrics and conductors are far from being negligible, due to the typical length of TDR probes (tens of meters and more). In the Section dedicated to FDTD algorithm, it will be stressed that such effects can be modeled in the time domain, but it is practically too much of a challenge at least for three reasons:

- Converting frequency-dependent laws in time domain convolution kernels or equivalent lumped networks leads to ambiguities in the perspective of a profile-oriented model
- The application of convolution kernels increases the computational burden of the simulation
- Using equivalent lumped networks implies heavy modifications on standard FDTD algorithms

Furthermore, losses are customarily modeled in the frequency domain, in which well known analytic formulae are already available. Summing up, having in mind the goal of simulating TDR systems, the following two requirements must be fulfilled:

- It must be possible and easy to specify arbitrary profiles of the primary parameters;
- It must be possible and easy to specify frequency-dependent primary parameters, in order to model dispersion effects.

The MATLAB-based software LineLab, that will be presented in Section 4.6, implements a simple, scalable and lightweight algorithm for the simulation of quasi-TEM TLs meeting these requirements. The proposed simulator produces both frequency domain and time domain outputs, with arbitrary profiles of the primary parameters, and arbitrary dispersion models. LineLab's core engine works in the frequency domain and handles frequency-dependent parameters of the line. Therefore, its execution time is inherently longer, with respect to simpler FDTD solvers handling only parameters independent on the frequency. However, the frequency domain solver is well suited for parallel computing, and can still reach outstanding timing performances when running on multiple threads, which nowadays is not a critical issue anymore even on mid-range laptops.

The LineLab project is freely available on-line in a public Git repository [60] which easily allows collaborative development of the simulation core and of any additional modules. Currently, the software package allows the simulation of standard TDR measurements, i.e., reflectograms, and of related standard frequency domain (VNA) measurements, namely S_{11} , group delay and VSWR.

In the following Sections the problem of simulating TDR waveform will be thoroughly dealt with by means of different approaches to the solution of the telegraph equations. The discussion will be always kept measurement-oriented and, in the last Section, four case studies for non-homogeneous TLs (i.e. TDR probes under working conditions) will be analyzed using the proposed simulation algorithm.

4.2 Simplified measurement setup

The classic theoretical discussion on terminated Transmission Lines will be here replaced by the direct applications of TL models to TDR setups. The simplest possible

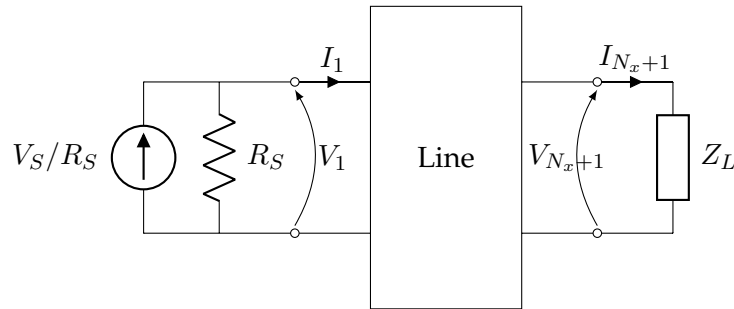


FIGURE 4.1: Two port model of a TDR measurement apparatus

setting, that is enough to develop the theoretical background, is depicted in Figure 4.1. This two-port representation deserves a few remarks. First, the TDR waveform is assumed to be measured at port 1, that is coincident with the generator port where, although usually a voltage stimulus (V_S) is used to drive TDR probes, a current equivalent ($I_S = V_S/R_S$) is introduced that is more suitable for the discussion brought on in this Chapter. Moreover, in common applications $Z_L \rightarrow \infty$, however a generic load impedance is considered for the sake of generality.

The simplified model in Figure 4.1 does not take into account some components of TDR measurement systems, especially when such systems do not rely on commercial reflectometers, that will be discussed later, namely:

- Reactive contributions to the generator internal impedance introduced by the output connectors
- The impedance of the acquisition system
- The presence of intermediate transitions or cables between the instrumentation and the TL.

4.3 TEM propagation mode and its equivalent circuit

Although from a microwave engineer's perspective it is an extremely coarse approximation, only Transverse Electromagnetic (TEM) mode is assumed to propagate in TLs applied to TDR measurement setups and, therefore, only the TEM mode equivalent circuit will be treated in this Chapter. Anyways, other circuit representations of TLs are also available for different propagating modes [61], [62].

There are four well known criteria for TEM propagation in a TL, that can also be good rules of thumb when designing a brand new TDR probe compatible with the TEM model:

1. EM fields are confined in uniform, isotropic dielectric materials
2. TEM lines include at least two conductors
3. Conductors must have infinite conductivity and dielectrics must be lossless

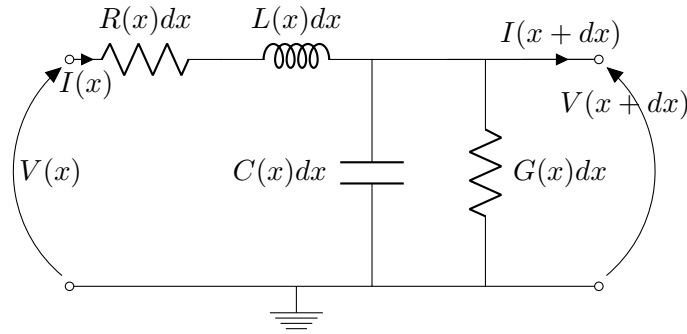


FIGURE 4.2: Transmission line elementary cell

4. The cross section of the line must not change

These requirements appear quite restrictive and in contradiction with the very principle of many TDR applications. A nonuniform profile of dielectric constant [8], e.g., glaringly contradicts the first requirement, whereas compression measurements [3] contradict the last one. Moreover, only seldom in practice dielectrics and conductors can be considered lossless, because TDR is inherently a broadband technique and high frequency components of its response can almost never be neglected. Nevertheless, it will be shown that the TEM approximation holds almost perfectly for the considered TLs.

Under the (quasi) TEM assumption, a segment of line of infinitesimal length dx can be modeled with the lumped elements circuit shown in Figure 4.2. The primary parameters thus introduced model, namely,

- R the non infinite conductance of the conductors
- L the total self-inductance of the conductors
- G the non-zero conductance of the dielectric
- C the capacitance due to the proximity of the conductors

This model can be improved by introducing the frequency-dependency of all four parameters.

A good understanding of the true meaning of such parameters is of great help in designing, choosing or optimizing TDR probes that exploit their variations due to the investigated phenomena.

4.4 Telegraph equations in the time domain

Kirchoff's voltage and current laws applied in the time domain to the circuit in Figure 4.2 respectively yield

$$\begin{cases} v(x, t) - R \partial x i(x, t) - L \partial x \frac{\partial i(x, t)}{\partial t} - v(x + \partial x, t) = 0 \\ i(x, t) - G \partial x v(x, t) - C \partial x \frac{\partial v(x + \partial x, t)}{\partial t} - i(x + \partial x, t) = 0 \end{cases} \quad (4.1)$$

Dividing by ∂x and solving for $\partial v(x, t)/\partial x$ and $\partial i(x, t)/\partial x$ respectively, the well known telegrapher equations (or Heaviside's equations) are promptly obtained:

$$\begin{cases} \frac{\partial v(x, t)}{\partial x} = -Ri(x, t) - L \frac{\partial i(x, t)}{\partial t} \\ \frac{\partial i(x, t)}{\partial x} = -Gv(x, t) - C \frac{\partial v(x, t)}{\partial t} \end{cases} \quad (4.2)$$

4.4.1 Finite Difference Time Domain algorithm

In the first instance, TDR setups have been modeled and reflectograms have been simulated by solving the telegraph equations directly in the time domain with a FDTD (Finite Difference Time Domain) algorithm. FDTD algorithms are a useful tool in that, with simple and fast implementations and with almost no need of code optimization, they provide a quick preview of how reflectograms behave under the normal operating conditions of the TDR probe. FDTD techniques are customarily used to simulate transient behaviors for many different applications [63], [64].

There are at least two constraints that must be considered when setting an FDTD algorithm up [65], i.e.

$$\begin{cases} \Delta t \leq \frac{\Delta x}{v} \\ \Delta x \leq \lambda_{\min}/10 \end{cases} \quad (4.3)$$

where $v = \max_x 1/\sqrt{LC}$ is the maximum propagation velocity of an EM wave along the line. While normally the time discretization step is chosen as $\Delta t \leq \Delta x \sqrt{LC}$, in this discussion the need to consider L and C non homogeneous along the line arises, thence the max operator must be applied.

Equations 4.2 must then be written in the discrete form with respect to both space and time. In this form, the space and time coordinates will be replaced with the k and n indices respectively, that are also used in the MATLAB code of Appendix A.

$$\begin{cases} \frac{v_k^n - v_{k-1}^n}{\Delta x} = -R_k i_k^n - L_k \frac{i_k^n - i_k^{n-1}}{\Delta t} \\ \frac{i_k^n - i_{k-1}^n}{\Delta x} = -G_k v_k^n - C_k \frac{v_k^n - v_k^{n-1}}{\Delta t} \end{cases} \quad (4.4)$$

By solving Equations 4.4 for i_k^n and v_k^n respectively, the update equations are immediately obtained:

$$\begin{cases} v_k^n = \frac{C_k/\Delta t}{G_k + C_k/\Delta t} \left(v_k^{n-1} - \frac{i_k^n - i_{k-1}^n}{\Delta x} \right) \\ i_k^n = \frac{L_k/\Delta t}{R_k + L_k/\Delta t} \left(i_k^{n-1} - \frac{v_k^n - v_{k-1}^n}{\Delta x} \right) \end{cases} \quad (4.5)$$

Intuitively, Equations 4.5 are applicable to all nodes of the equivalent electric network except the first and the last, where the generator and the load impedance must be taken into account. By applying Kirchoff laws to the schematics in Figure 4.3, the update equations for the source node can be easily obtained:

$$v_1^n = v_S^n - R_S i_1^n \quad (4.6)$$

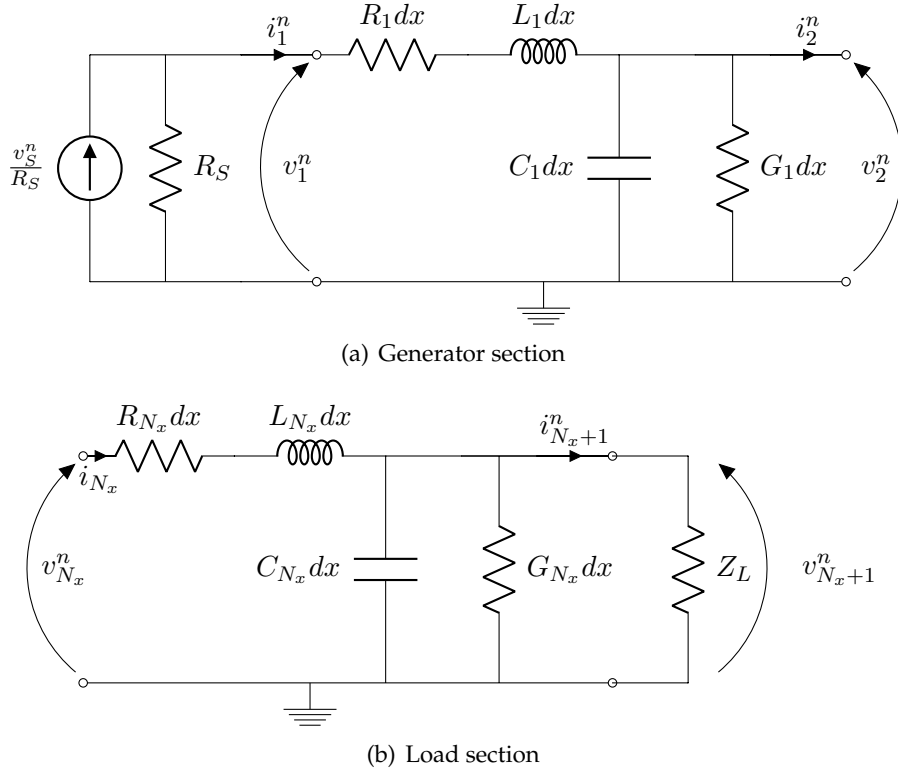


FIGURE 4.3: Generator and load sections of the TL equivalent circuit

and the same holds for the load section:

$$v_{N_x+1}^n = \frac{i_{N_x}^n - \frac{C_{N_x}}{\Delta t} v_{N_x+1}^{n-1}}{1 - G_{N_x} - \frac{C_{N_x}}{\Delta t}} \quad (4.7)$$

More sophisticated versions of Equations 4.6 and 4.7 have also been proposed [66], [67] to simulate complex loads.

4.4.2 Modeling losses and dispersion in the time domain

It may be argued that, applying the telegraph equations in this form, losses and other dispersive effects are a nontrivial issue, and this is true indeed. Frequency-dependent resistance and inductance due to the skin effect, e.g., could only be taken into account by replacing the constant R and L in Eq. 4.2 with a suitable time-dependent function $Z(t)$ [68], so that the first equation in 4.2 becomes

$$\frac{\partial v(x, t)}{\partial x} = -Z(x, t) * i(x, t) \quad (4.8)$$

However, computing $Z(x, t)$ might prove a tricky task, and computing convolution integrals is often unfeasible in actual simulation algorithm. Scarlatti and Holloway have shown that, due to the smooth behavior of the frequency-dependent R, L, G

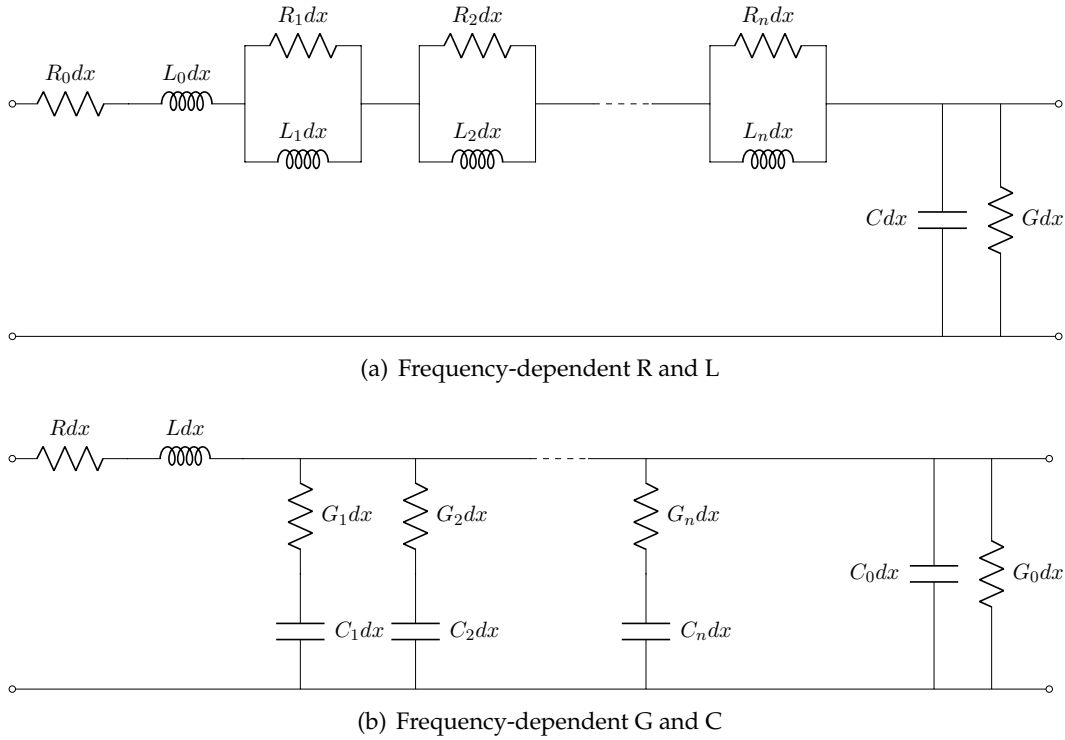


FIGURE 4.4: Convolution-free approximation of frequency-dependent primary parameters as proposed in [69]

and C , a good convolution-free approximation can be achieved by substituting $R-L$ series with a small number, n_c , of parallel $R-L$ cells (Figure 4.4(a)) and $G-C$ parallels with series $G-C$ cells (Figure 4.4(b)) [69]. Basically, this approximation descends from the synthesis of the frequency-dependent characteristic impedance with a Foster first form network [70].

The proposed circuit model can be introduced in the classic FDTD implementation, however this procedure is not seamless and modestly increases the computational burden of the simulation (good results with respect to full wave simulations can be achieved with $n_c = 5$ at most). This approximation is proven to be excellent for the simulation of standard homogeneous TLs with different geometries, ranging from Coplanar Waveguides (CPW) to Microstrip Lines and even for a circular wire over a ground plane. However, the computation of the lumped element values for the elementary cell requires a preliminary full wave simulation and the implementation of optimization routines. Moreover, the simulation of non-homogeneous TLs would not be feasible because the implementation of changing L , R , G and C profiles is not considered and would be, after all, an ambiguous problem if one follows the approximation approach of [69].

4.5 Telegraph equations in the frequency domain

In the most realistic setting, the primary parameters depend on the frequency because of losses in both dielectrics and conductors. On a nontrivial side note, it is crucial to understand what the frequency boundaries imposed by the TDR system are, and this can roughly although effectively be achieved by measuring the rise time of the stimulus (t_r , for step-like signals) or its duration (t_w for pulse-like signals) [71]. If at $f = 1/t_{r/w}$ losses and dispersion effects are neglectable, the frequency dependency of the primary parameters can also be neglected and the TL can be safely simulated by means of a fast and easy to implement FDTD (Finite Difference Time Domain) algorithm [65]. Guidelines for this kind of decision will be given when outlining dispersion effects and losses relevant to TDR applications.

In most practical situations, however, losses and dispersion cannot be neglected. In that case, it is convenient to write Heaviside's equations in the frequency domain:

$$\begin{cases} \frac{dV(x,\omega)}{dx} = -RI(x,\omega) - j\omega LI(x,\omega) \\ \frac{dI(x,\omega)}{dx} = -GV(x,\omega) - j\omega CV(x,\omega) \end{cases} \quad (4.9)$$

By introducing the complex impedances

$$\begin{cases} Z_s = R + j\omega L \\ Z_p = (G + j\omega C)^{-1} \end{cases} \quad (4.10)$$

Equations 4.9 become:

$$\begin{cases} \frac{dV(x,\omega)}{dx} = -Z_s I(x,\omega) \\ \frac{dI(x,\omega)}{dx} = -Y_p V(x,\omega) \end{cases} \quad (4.11)$$

The coupled Partial Differential Equations 4.2 have been transformed in coupled Ordinary Differential Equations that are way easier to solve.

4.5.1 Modeling losses and dispersion in the frequency domain

It is straightforward to model losses and other dispersion effects in the frequency domain by applying well known theoretical results. The models depend on the specific line geometry, and extremely realistic results can be achieved by simply applying analytic formulae derived for standard line geometries (e.g. coaxial cables and twin leads) [59]. A brief recap of formulae for conductor losses in coaxial lines and twin leads is reported as an example in Table 4.1. Dielectric losses, on the other hand, depend on the fact that dielectric materials inherently dissipate EM energy. This phenomenon can be related to both two properties of the material:

- Nonzero conductivity ($\sigma_d \neq 0$)
- Complex permittivity ($\epsilon = \epsilon' - j\epsilon''$)

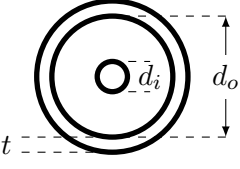
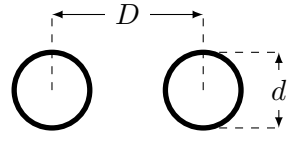
Geometry		
$R(\omega)$	$\frac{1}{2\pi} \sqrt{\frac{\omega\mu_0}{2\sigma_c}} \left(\frac{2}{d_i} + \frac{2}{d_o} \right)$	$\frac{2}{\pi D} \sqrt{\frac{\omega\mu_0}{2\sigma_c}}$
$L(\omega)$	$\frac{\mu_0}{2\pi} \log \left(\frac{d_o}{d_i} \right) + \frac{1}{2\pi} \sqrt{\frac{\mu_0}{2\sigma_c\omega}} \left(\frac{2}{d_i} + \frac{2}{d_o} \right)$	$\frac{\mu_0}{\pi} \left(\frac{1}{4} + \operatorname{acosh} \left(\frac{D}{d} \right) \right)$

TABLE 4.1: Frequency dependent resistance and inductance in coaxial lines and twin leads

Both properties can be effectively introduced in Maxwell's curl equation for the magnetic field, that can be written as:

$$\nabla \times \mathbf{H} = j\omega\epsilon'\mathbf{E} + (\omega\epsilon'' + \sigma_d)\mathbf{E} \quad (4.12)$$

and the loss tangent is defined as the lossy to lossless coefficients in 4.12:

$$\tan \delta = \frac{\omega\epsilon'' + \sigma_d}{\omega\epsilon'} \quad (4.13)$$

where usually $\sigma_d \ll \omega\epsilon''$ at the frequencies of interest, so that it is safe to assume that

$$\tan \delta \simeq \frac{\epsilon''}{\epsilon'} \quad (4.14)$$

Finally, this parameter is easily introduced in the circuit model in Figure 4.2 by simply assuming that $G = \omega C \tan \delta$.

4.6 TDR simulation with arbitrarily profiled parameters

In this Section, a novel custom made TL simulation algorithm, designed around TDR systems, named LineLab, is introduced. LineLab models TLs as a sequence of N_x elementary cells (Figure 4.2). The distributed primary line parameters are considered, in general, different from cell to cell and, therefore, they are an arbitrary function of the position on the line x . This is exactly the case of distributed sensing systems where, e.g., ϵ_r changes along the line and so, as a consequence, does the C parameter.

Considering the frequency domain telegraph equations, derived in 4.5, any dispersion model can be easily implemented for each parameter, together with its profile along the line. In particular, the generic telegraph equations of Eq. (4.11) are hereby considered. Doing so, as will be explained later, greatly eases the computational burden of the simulation.

To solve numerically the equations, a suitable range of frequencies and a consistent elementary cell length Δx need to be chosen. Both choices can be essentially arbitrary, as long as the third constraint in (4.3) holds.

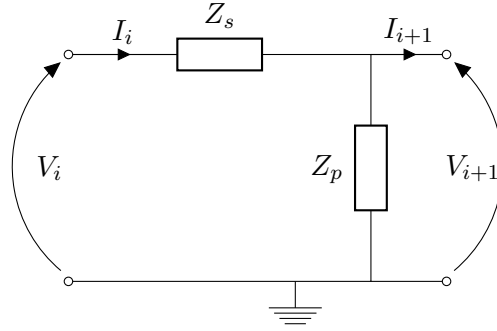


FIGURE 4.5: Simplified elementary cell

and for $i = N_x + 1$

$$Y(f)^{(i=N_x+1)} = \begin{bmatrix} \ddots & & -Y_s^{(N_x-1)} & & 0 \\ -Y_s^{(N_x-1)} & Y_s^{(N_x-1)} + Y_p^{(N_x-1)} + Y_s^{(N_x)} & & & -Y_s^{(N_x)} \\ 0 & & -Y_s^{(N_x)} & & Y_s^{(N_x)} + Y_p^{(N_x)} + Y_L \end{bmatrix} \quad (4.17)$$

where Y_L is a generic load impedance.

Finally, the frequency response of the line $H(x, f) = V(x, f)/V_S$ must be derived and, therefore, the vector \mathbf{J} of current stimuli must be written. With respect to Figures 4.1 and 4.5, the elements of this vector are all zeros except for $\mathbf{J}^{(i=1)} = V_S/R_S$, because there is only one independent current source at the first node of the network.

The vector of voltages along the line is then derived by applying Ohm's law in terms of admittance and solving the tridiagonal system

$$Y \cdot \mathbf{V} = \mathbf{J} \quad (4.18)$$

4.6.2 Fast tridiagonal solver

It has been shown in Eq. (4.16), (4.15) and (4.17) that the admittance matrix Y is tridiagonal, allowing one to solve the system (4.18) with extremely efficient algorithms.

In LineLab, the system (4.18) is solved by means of a simplified form of Gaussian elimination, known as Thomas algorithm, whose stability is assured by the composition of the admittance matrix [72]. Such algorithm has also been slightly modified to enhance computational efficiency. Considering that, in most applications, the only required solution is $\mathbf{V}^{i=1}$, i.e. the response at the beginning of the line, one may consider the equivalent linear problem

$$\mathcal{T} \cdot \Phi = \mathbf{I} \quad (4.19)$$

where

$$\begin{cases} \mathcal{T} = J_{N_x+1} Y J_{N_x+1} \\ \Phi = J_{N_x+1} \mathbf{V} \\ \mathbf{I} = J_{N_x+1} \mathbf{J} \end{cases} \quad (4.20)$$

and J_{N_x+1} is the backward identity matrix.

The Thomas algorithm is applied to the tridiagonal problem (4.19) and, considering that $\Phi^{i=N_x+1} \equiv \mathbf{V}^{i=1}$, the backward substitution phase of the solver is arrested at its first step.

Benchmarks have been performed and the simulation times of the proposed solver have been compared to those of a FDTD algorithm. To keep benchmark data consistent, simulations have been run for an increasing number of time domain samples while keeping the number of elementary cells fixed to 1000, with LineLab running on 4 simultaneous threads. Results are depicted in Figure 4.6.

As stated in the Introduction, the frequency domain simulation has an inherently higher computational cost, more specifically because each frequency requires its own loop, but still computation times lay in quite an acceptable range, even for heavily oversampled simulations. Such loops are, on the other hand, completely independent of each other and, therefore, the computation time is expected to decrease almost linearly with the number of simultaneous threads on which LineLab runs.

4.6.3 Final remarks about the simulation algorithm

The results of [65] can be easily reproduced by using a suitable Fourier representation of the stimulus signal I_S , computing the corresponding $V(x, f)$ at the first node, and transforming the result to a time domain signal with an inverse Fourier transformation.

Some final remarks need to be made about the advantages of the proposed simulation approach:

- the frequency response of the line allows one to simulate measurement results from a wide range of instruments, provided that a suitable Fourier-like decomposition of stimuli is possible;
- the behavior of the line can be investigated at any of its node, if needed;
- any load impedance can be applied without modifying the algorithm;
- it is straightforward to define custom profiles for the primary parameter and to implement suitable dispersion models;
- also point mismatches (e.g. capacitive faults) can be easily implemented, thus providing a useful modeling tool also for power grids and telecommunication networks.

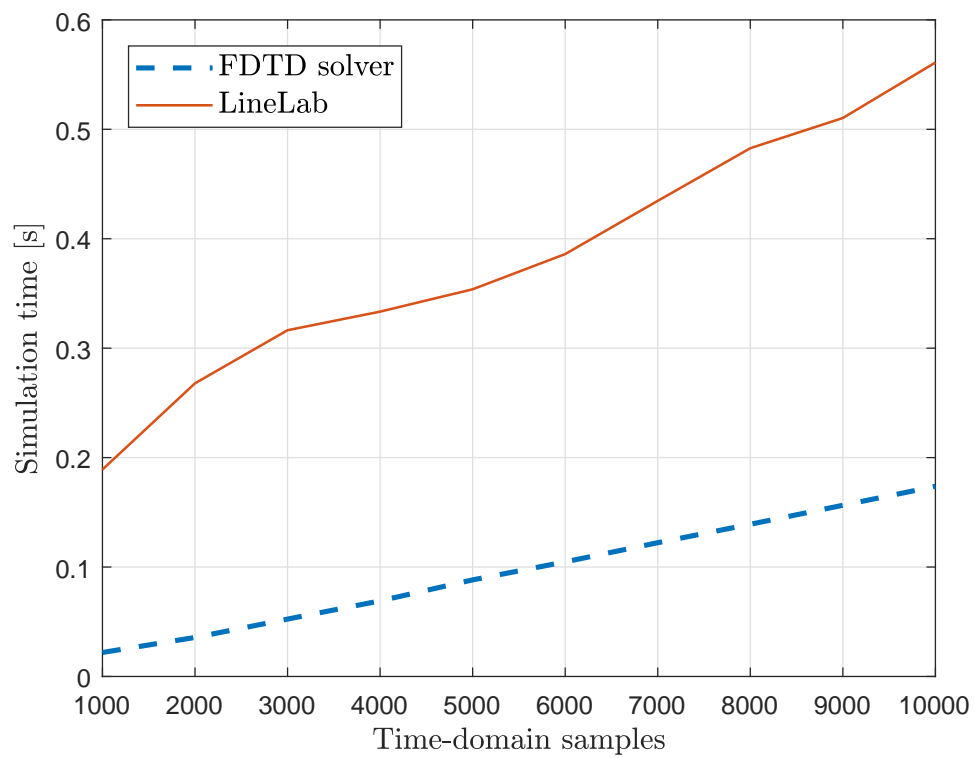


FIGURE 4.6: Simulation times for fixed number of elementary cells
 $N_x = 1000$

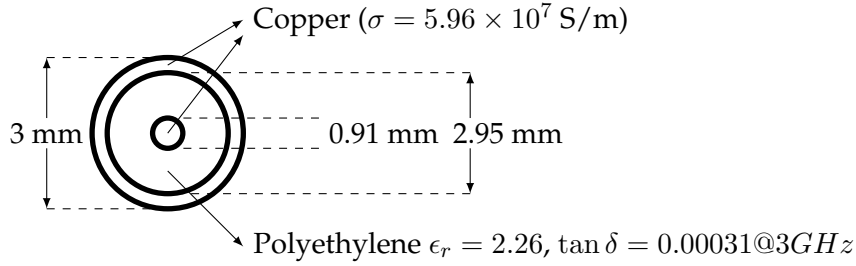


FIGURE 4.7: Cross section of the simulated coaxial line

4.6.4 Simulation outputs

In this Section some relevant simulation outputs are shown and briefly discussed. Since virtually any scenario can be simulated with the proposed approach, the chosen outputs emulate those of actual instrumentation.

Every simulation output is obtained from the frequency response of the line $H(x, f)$, computed as described in Section 4.6.1. To keep the discussion focused on the simulation algorithm, all the results are referred to the frequency response at the beginning of the line, i.e.

$$H^{(1)}(f) = \frac{V^{(1)}(f)}{V_S} \quad (4.21)$$

where $V^{(1)}(f)$ is simply the first element of the vector \mathbf{V} that solves the system (4.18), and $V_S = R_S I_S$, with reference to Figure 4.1. Even so, any other simulation output can easily be obtained as well.

4.6.5 Reference transmission line

All the results hereby discussed have been obtained by simulating the same 1 m long coaxial line with the same cross section as a common RG58-CU cable, except from the outer jacket that can safely be neglected. Conductor and dielectric losses are taken into account by considering typical values for copper and polyethylene parameters respectively, and simulation results are also presented for the lossless case, i.e. where skin effect and dielectric losses are neglected, thus stressing how losses affect frequency domain outputs and, which is of foremost importance, TDR waveforms.

Reference values for the geometry of the sample coaxial line are provided in Figure 4.7. On the other hand, regarding material-specific parameters:

Polyethylene $\tan \delta = 0.00031@3GHz$

$$\epsilon_r = 2.26@3GHz$$

Copper $\sigma = 5.96 \times 10^7$ S/m

4.6.6 Frequency domain results

In Figure 4.8 the magnitude and phase of the S_{11} scattering parameter for the model of a 50Ω coaxial cable are shown. These simulated curves emulate measurements performed with any Vector Network Analyzer. The complex values of S_{11} (for a two-port network) (or of the Return Loss RL for the considered one-port model) are directly derived from $H^{(1)}(f)$ as

$$S_{11}(f) = 2\frac{V^{(1)}(f)}{V_S} - 1 = 2H^{(1)}(f) - 1 \quad (4.22)$$

In the considered model, the line is left open-ended ($Z_L \rightarrow \infty$), therefore for a lossless cable (dashed line) $|S_{11}| = 0$ dB, and for a more realistic model, that includes the skin effect and dielectric losses simulation, $|S_{11}|$ decays with the frequency.

Although LineLab has been specifically developed for time domain simulations, once S_{11} has been computed, it also computes other frequency domain outputs if needed. LineLab automatically computes the Voltage Standing Wave Ratio and the group delay.

Simulator validation and feature comparison with commercial software packages

The developed simulation algorithm has been validated against identical line models implemented in commercial simulation software. This validation step also allows to investigate the state of the art of TDR simulation and to highlight the advantages and disadvantages of the presented simulation approach. COMSOL Multiphysics (1D Transmission Line module) and AWR Microwave Office (MWO) have been chosen for the comparison as they offer way different modeling work flows and simulation algorithms. Both software packages immediately allow to perform frequency domain simulations, however they do not allow to straightforwardly pass to the time domain for the purpose of TDR simulation with a custom stimulus. Therefore, the comparison has been performed on the basis of only S_{11} , considering that elementary Fourier analysis allow to compute the time domain response of the modeled line.

Simulations results are reported in Fig. 4.9 for an open ended unit length (1 m) RG-58 CU coaxial cable. The proposed MATLAB simulator behaves correctly with simple models, also showing an outstanding computational performance if compared with COMSOL Multiphysics. MWO is the fastest simulator among those tested, but, on the other hand, lacks any profiling feature, hence not being able to model distributed sensing systems.

The performances of the proposed algorithm have also been benchmarked and the time required, on an average laptop, to solve for a single frequency (admittance matrix assembly plus tridiagonal system solution) is $1.5 \mu\text{s}$ per cell. More detailed information and comparisons among the tested simulators are reported in Table 4.2.

Please note that MWO natively supports Time Domain Reflectometry simulation, but it does not allow one to suitably define the spectrum of propagating signal,

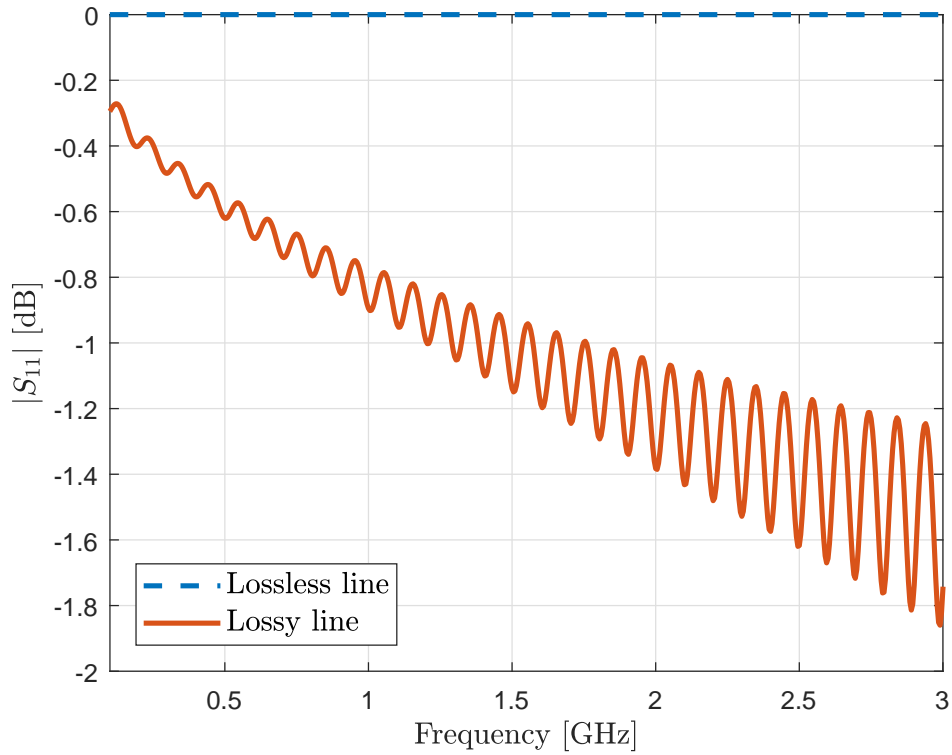
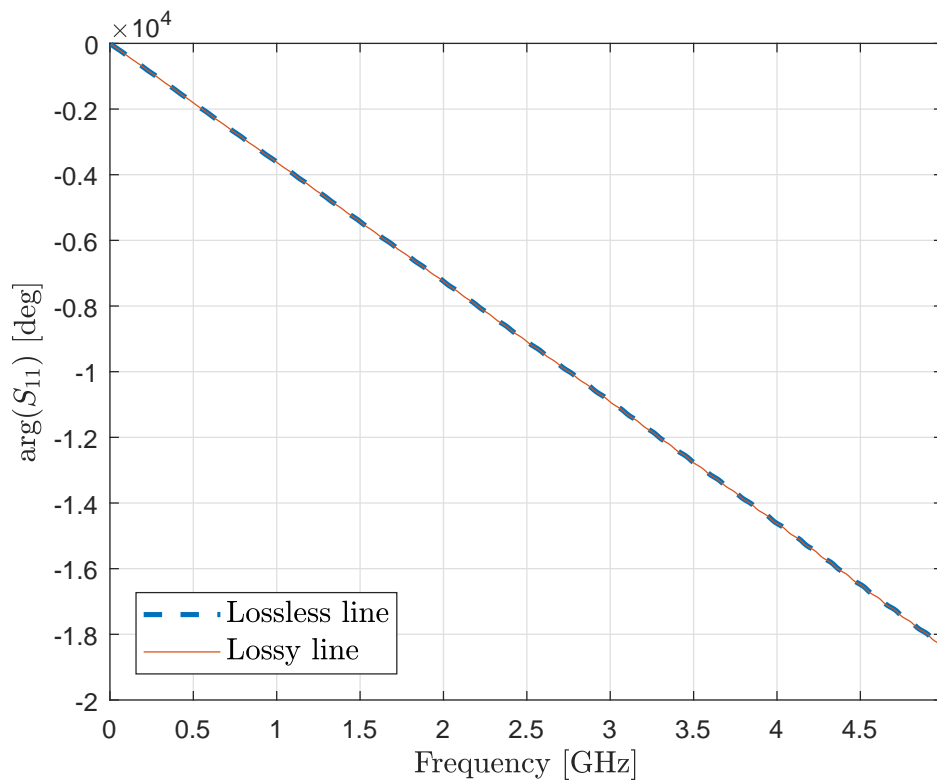
(a) $|S_{11}|$ (b) $\arg(S_{11})$

FIGURE 4.8: Reflection coefficient at reflectometry port (S_{11}) for a simulated 1 m long coaxial cable left open-ended

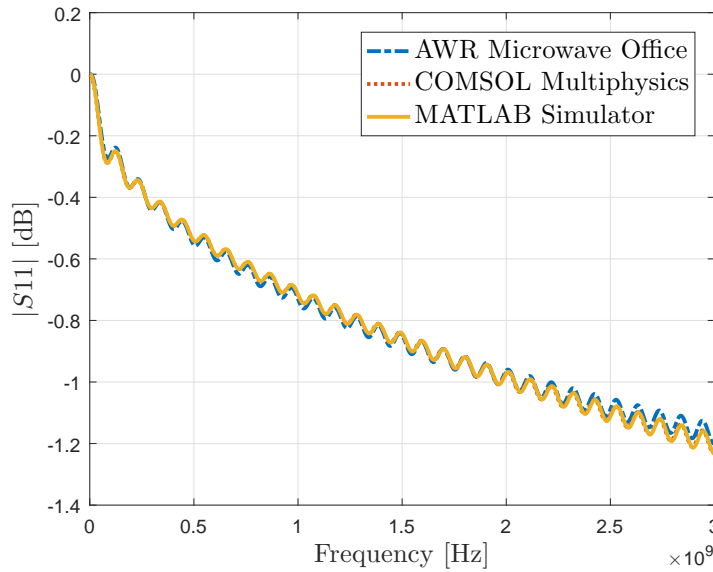


FIGURE 4.9: $|S_{11}|$ simulation for a 1 m long coaxial cable (RG-58 CU) performed in different simulation environments.

TABLE 4.2: Simulator features comparison

	MWO	COMSOL	LineLab
Speed	Fastest	Slowest	Fast
Optimization module(s)	✓	✓	✓
Custom LRGC profiles	✗	✓	✓
Custom dispersion	✗	✓	✓
TDR simulation	✓	✗	✓

which is an indispensable feature for the realistic simulation of a complete TDR system. At the same time, COMSOL allows to customize the profile of primary parameters along the line and their dispersion functions. However, no default dispersion model is provided by default for the 1D Transmission Line model and, therefore, each dispersion function as for skin effect and Debye dielectric relaxation needs to be manually outlined.

4.6.7 Time domain results

Once the line has been simulated in the frequency domain, any time domain result can be obtained by means of FFT-based algorithms. For the results presented in this Section, the Fast Fourier Transform is directly applied, because it is safely applicable to the considered signals, for which it is also the fastest numerical transform algorithm.

In the simplest possible situation, i.e. where measurements are taken exactly at the beginning of the line, the time domain response of the TL is

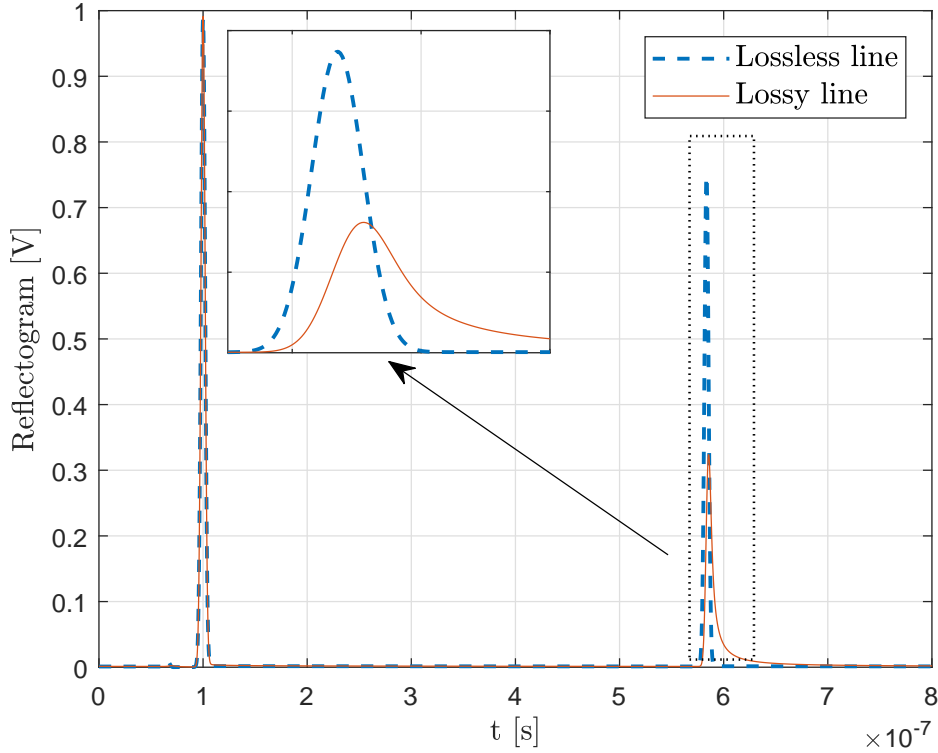


FIGURE 4.10: Time Domain Reflectometry on a 50m long coaxial cable, using a synthetic Gaussian pulse as stimulus signal

$$v^{(1)}(t) = \mathcal{F}^{-1} \left[H^{(1)}(\omega) \mathcal{F}[v_S(t)] \right] \quad (4.23)$$

The first interesting result in the time domain takes cue from [65], in that a time domain reflectometer (TDR) is simulated. In Figure 4.10, the TDR waveform obtained by applying a Gaussian pulse stimulus signal to a 50m long coaxial line is represented. In the Figure, the dotted line depicts the TDR waveform that is obtained when skin effect and dielectric losses are not simulated, meanwhile the continuous line also simulates the skin effect and, therefore, the reflected pulse is wider, with a different shape, and is lower in amplitude.

Many commercial TDR instruments (e.g. the widespread Campbell Scientific TDR200 [73]) use step-like signals instead of pulses as stimulus, which are not easily representable in the Fourier domain. However, their derivatives are pulse-like signals and, because of the linearity of the simulated system, the step response of the line may be simply computed by means of numerical integration, as shown in Figure 4.11. Analogous procedures can be followed for any non low-pass stimulus.

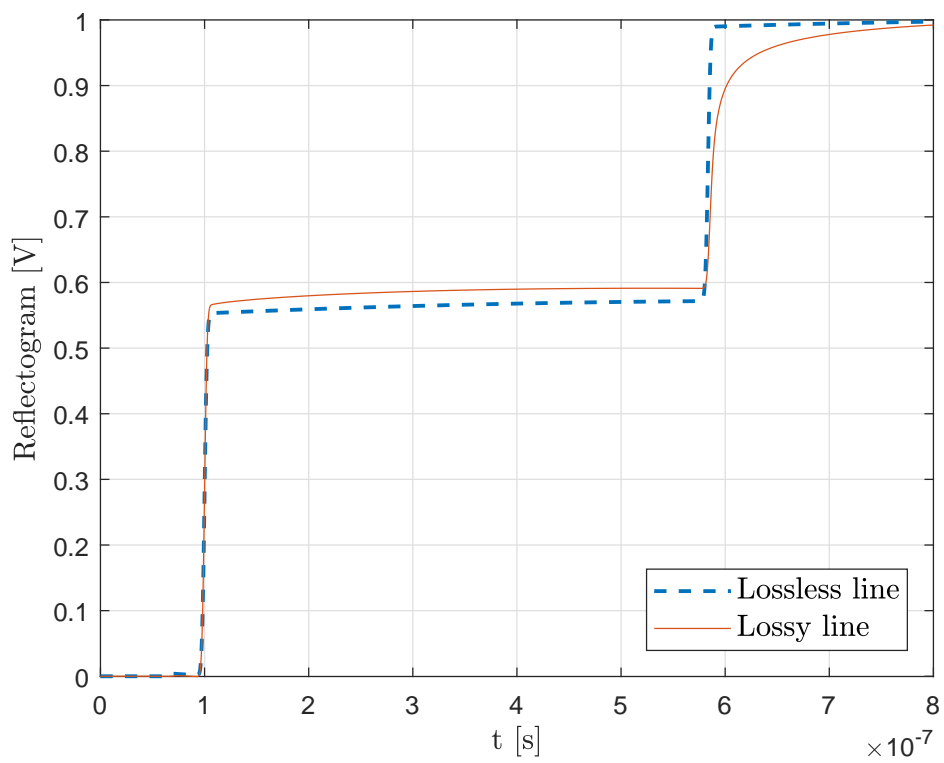


FIGURE 4.11: Time Domain Reflectometry on a 50m long coaxial cable with step-like stimulus, obtained by numerical integration of the pulse response

Simulation settings and setup precautions The frequencies at which $H^{(1)}(\omega)$ must be computed, and the number N_x of discrete cells in which the line must be discretized, depend on the particular stimulus signal $v_S(t)$ and on the line length.

Let us assume that $v_S(t)$ is made of N_t equispaced samples in the range $[0, t_{max}]$, with N_t even. Therefore, $H^{(1)}(\omega)$ must be computed at the frequencies $[0, 1, \dots, N_t/2] \cdot \Delta f$, where $\Delta f = 1/t_{max}$. The cell length is chosen conveniently small with respect to λ_{min} , exactly as discussed for FDTD algorithms (Section 4.4.1):

In the developed software it is also possible to override the default settings and perform simulations on any needed frequency range, with custom cell length. For this case, some basic warnings about possibly inconsistent simulation results are generated, e.g. simulation results at $\lambda \leq 10 \cdot \Delta x$ are marked as inconsistent.

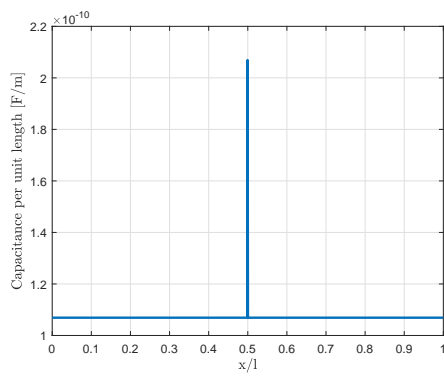
The proposed simulator can accurately model any TDR measurement system where transitions between the reflectometer and the probe have been “calibrated out”. This means that the stimulus signal which will give the most realistic time domain simulation of the reflectogram must be measured on a load matching the source impedance, i.e. directly at the reflectometer port. Moreover, if there are cables, transitions and so forth preceding the DUT, such elements in the signal chain must be always taken into account, and, therefore, they must be included in the Transmission Line model. This very last issue will be thoroughly discussed in Chapter 5.

4.7 Case studies

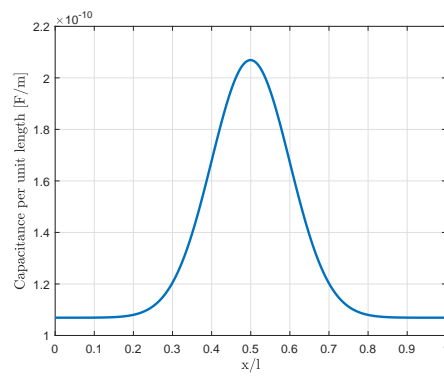
Four case studies will be hereby presented, and the primary parameter profiles relevant to each case are shown in Figure 4.12, namely:

- Concentrated capacitive fault
- Distributed Gaussian profile of capacitance
- Step-like capacitive faults
- Distributed rectangle-like resistive fault

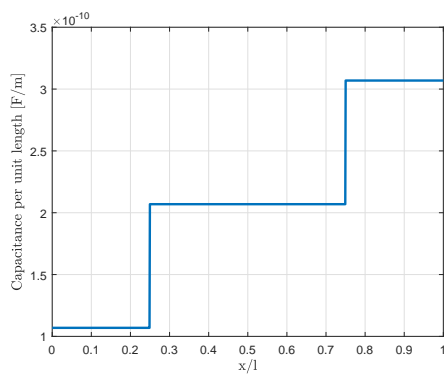
Such profiles are simple yet effective models that on one hand enable faithfully reproducing real-life TDR measurements and, on the other hand, give an intuitive and practical overview about the effects of distributed faults on TDR waveforms. More in detail, a concentrated capacitive fault, which is the simplest possible profile that can be studied, can be reproduced in real life by directly connecting a capacitor in parallel to any TL (e.g. two coaxial cables joint by means of a T connector). The Gaussian capacitive fault helps getting a first idea about the influence of a distributed, however “fading”, impedance mismatch influences reflectograms. The step-like capacitive faults, instead, model the interfaces between layered materials with different dielectric constants. Finally, an example of resistive fault is introduced that models a worn portion of TL, so that the effect of resistance per unit length variations on reflectograms can also be understood.



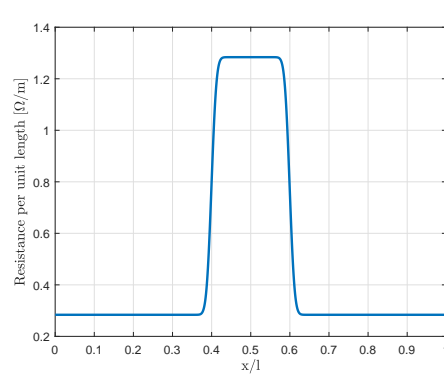
(a) Concentrated capacitive fault



(b) Gaussian profile of capacitance per unit length



(c) Step-like capacitive faults



(d) Rectangle-like profile of resistance per unit length

FIGURE 4.12: Case studies for the analysis of non-homogeneous Transmission Lines

4.7.1 Concentrated capacitive fault

This is the simplest possible case study. It is essentially trivial to understand what happens to the reflectogram in this case, because the fault is assumed to be concentrated in a single point of the line.

Even so, it is interesting to observe that, although the feature introduced by the capacitive fault is well visible, the velocity of propagation of the stimulus signal is not considerably altered by the fault, i.e. the reflected pulse in the reflectograms (dashed red line and solid blue line in 4.13(b)) are almost indistinguishable. In order to appreciate the small variation of propagation velocity, a stimulus signal with broader bandwidth should be used.

4.7.2 Distributed Gaussian profile of capacitance

In this case study, the shape of the fault is almost symmetric, but the reflected pulse is delayed and slightly changed in shape, due to the reactive nature of the fault. In other words, the capacitive fault results in a short length of transmission line with smaller propagation velocity, where the traveling wave slows down.

4.7.3 Step-like capacitive faults

In Figure 4.15 simulation results are reported for two interfaces located at $l_f^{(1)} = 0.25l$ and $l_f^{(2)} = 0.75l$ respectively.

In this case, the pulse reflected by the open termination is strongly delayed and changed in shape, and the interfaces are clearly visible on the reflectogram. It is also interesting to point out that, although $\Delta\epsilon_r^{(1)} = \Delta\epsilon_r^{(2)}$, the second interface appears way smaller than the first. The reflection coefficient at the interfaces between layered materials is

$$\Gamma = \frac{Z_j - Z_i}{Z_j + Z_i} \quad (4.24)$$

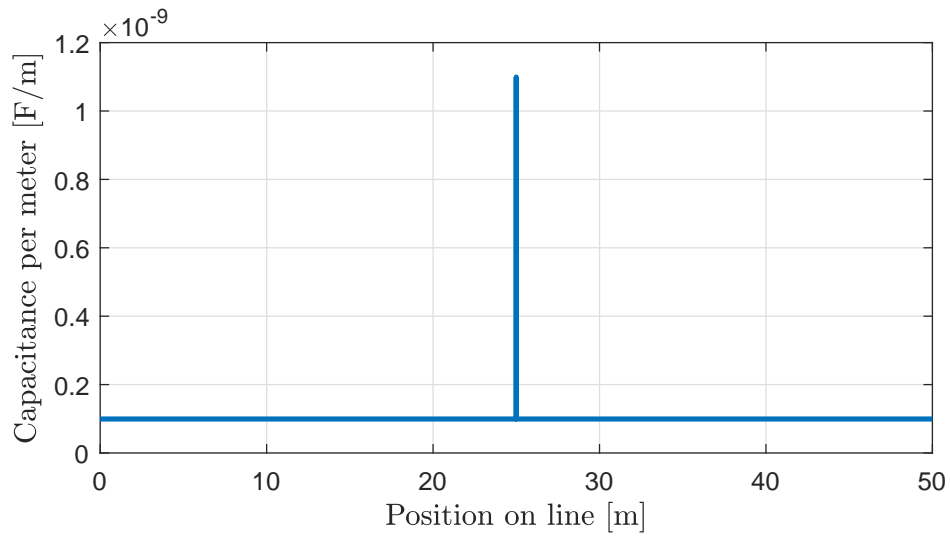
where $i = 1, 2$ and $j = i + 1$. The characteristic impedance of each section of the line is $Z_i = \sqrt{L_i/C_i}$, therefore, assuming that L is uniform along the line, the same $\Delta\epsilon_r$ produces different features on the reflectogram, as clearly visible in Figure 4.15(b).

4.7.4 Distributed rectangle-like resistive fault

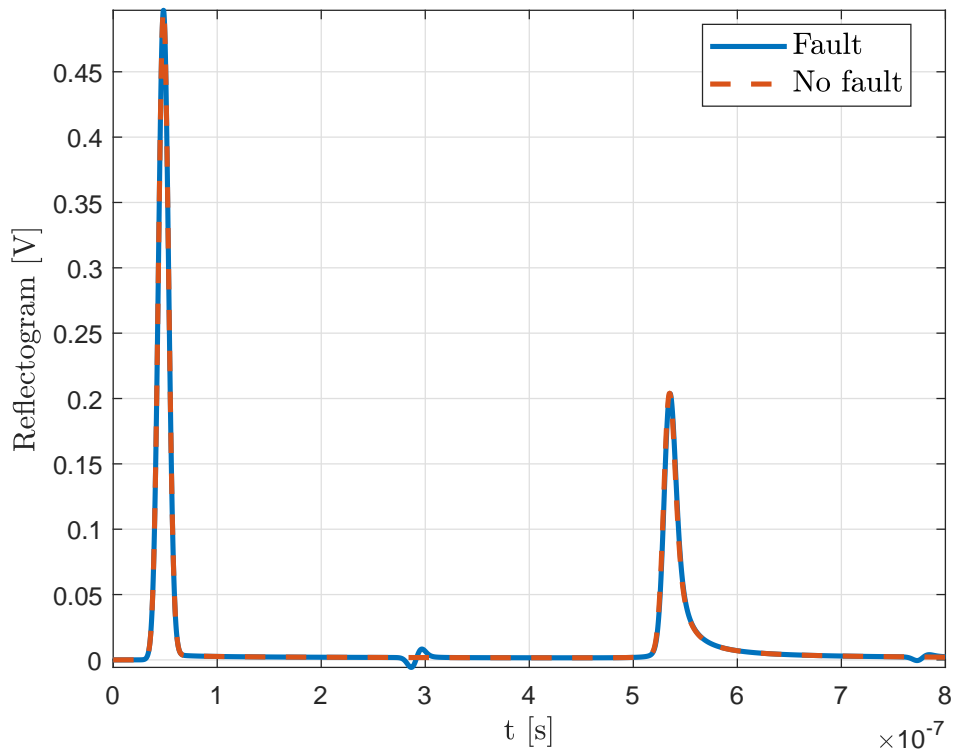
A damaged or worn section of a cable can be modeled with a resistive mismatch in its TL model. In Figure 4.16, a 10 m long distributed fault on a 100 m long line is simulated using the proposed frequency/time domain approach.

The increased resistance per unit length is clearly visible on the reflectogram as a raised waveform segment roughly located halfway between the stimulus signal and the reflected pulse. Although the given profile (Figure 4.16(a)) is perfectly symmetric, its effect on the TDR signal is not, due to dispersion.

Moreover, the reflected pulse in the damaged line is scaled with respect to that in the line with no faults; however, it is not delayed nor its shape is changed.

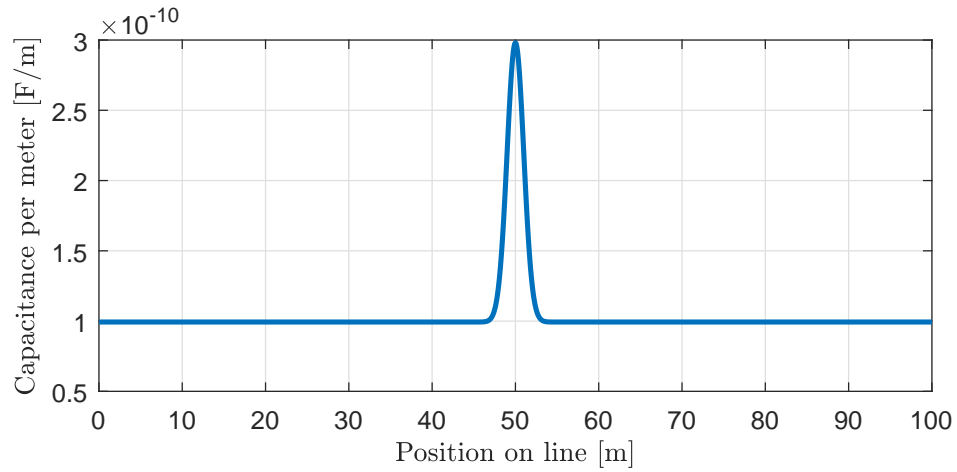


(a) Concentrated capacitive fault

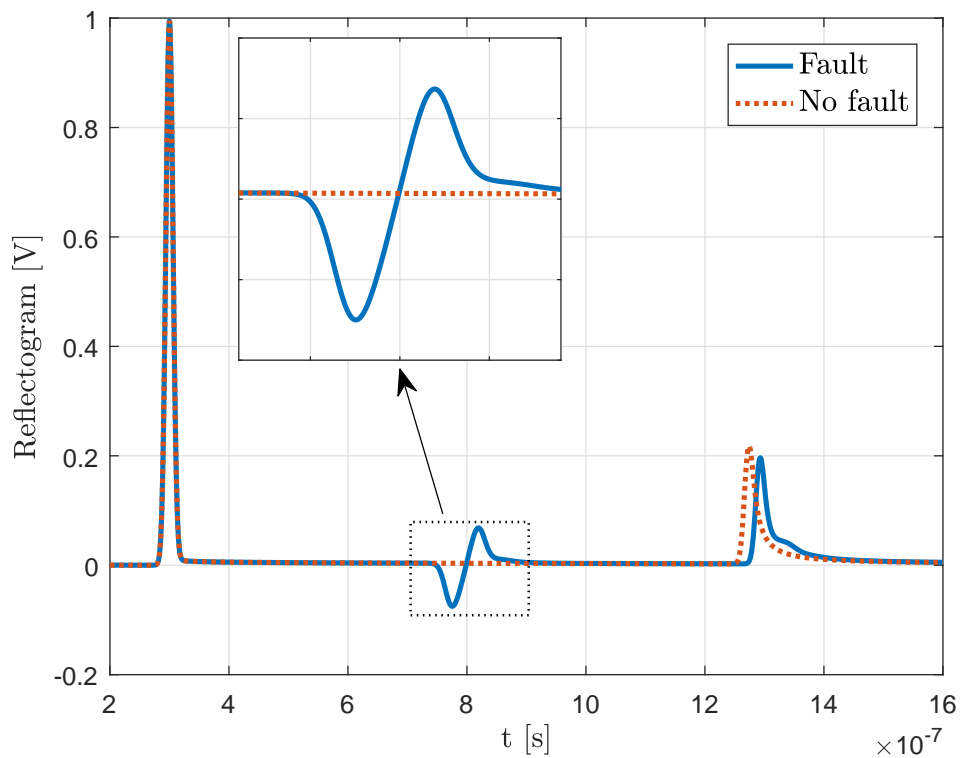


(b) Reflectogram for a concentrated capacitive fault

FIGURE 4.13: Concentrated capacitive fault in a 50m long line, centered at $l_f = 25\text{m}$

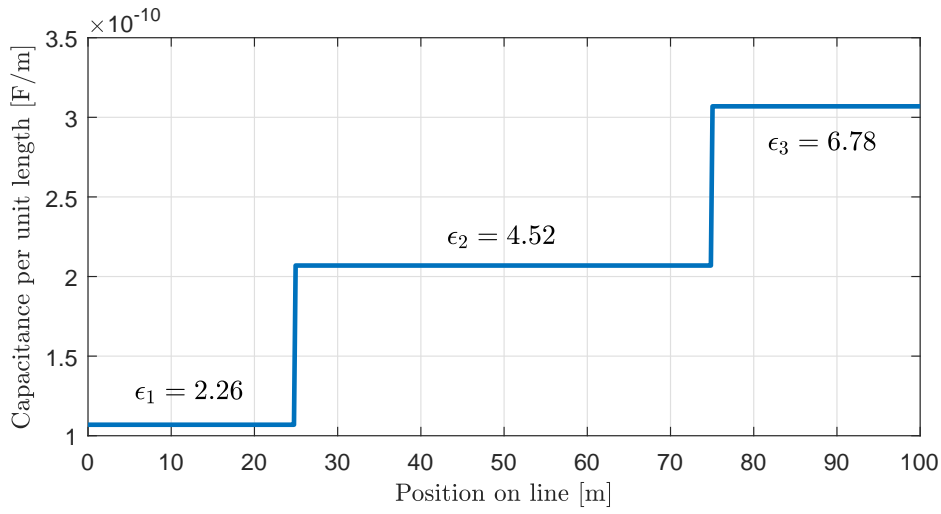


(a) Distributed capacitive fault profile

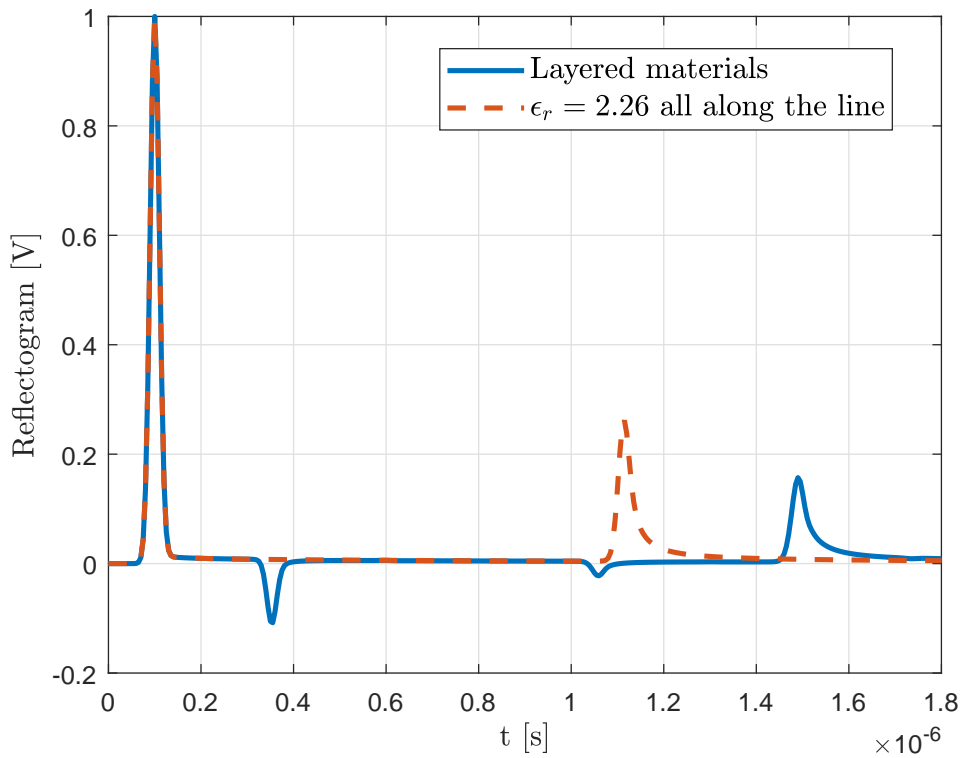


(b) Reflectogram for a distributed capacitive fault

FIGURE 4.14: Distributed capacitive fault in a 100m long line, centered at $l_f = 50\text{m}$

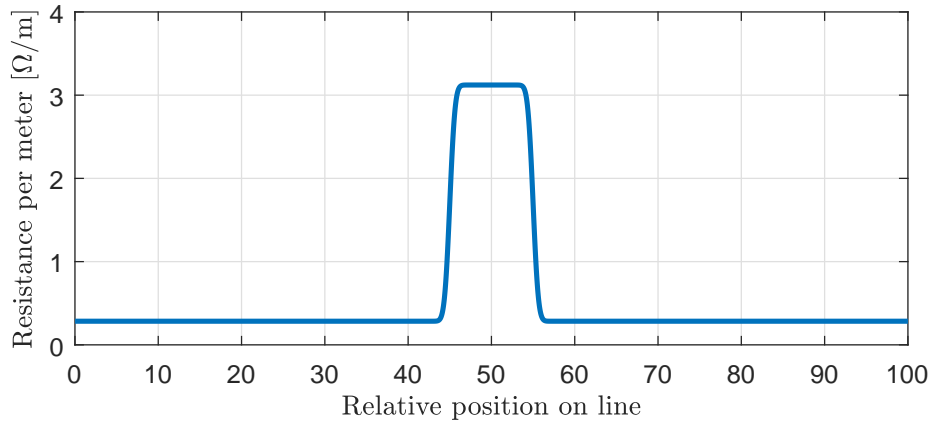


(a) Distributed capacitance profile for three layered materials

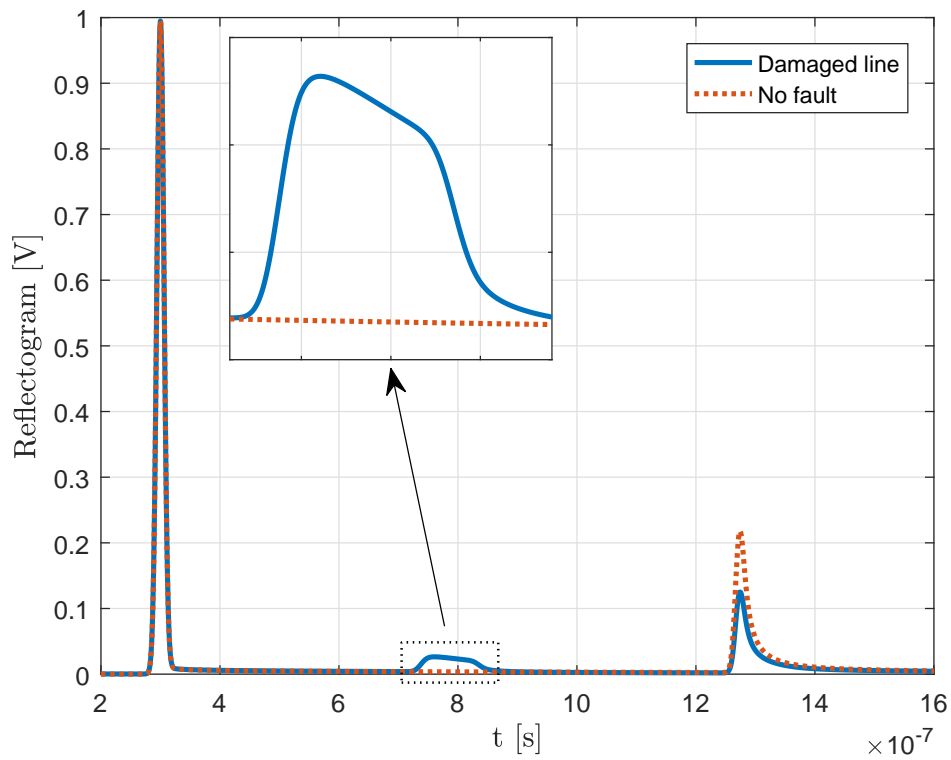


(b) Reflectogram for three layered materials (continuous line) and reflectogram for a line without mismatches

FIGURE 4.15: Interfaces between materials with different ϵ_r located at $l_f^{(1)} = 0.25l$ and $l_f^{(2)} = 0.75l$, with $l = 100\text{m}$



(a) Distributed resistive fault profile



(b) Reflectogram for a distributed resistive fault

FIGURE 4.16: Distributed resistive fault in a 100m long line, centered at $l_f = 50$ m

Chapter 5

Calibration of the TDR setup for simulation-based measurements

Quite often, the desired reference plane is NOT where you are able to measure the device, because the device must be mounted in a test fixture in order to measure it. If you know the approximate length of the test fixture you can perform a “poor-man’s de-embedding” procedure to move the reference plane of the measurement toward the device

MICROWAVES 101

5.1 Overview of the time domain calibration problem

In Chapter 4 a general purpose hybrid time-frequency domain simulation algorithm for non-homogeneous Transmission Lines has been introduced. In Section 4.6.7, the procedure to obtain time domain results from frequency domain simulation is discussed and, specifically, Equation 4.23 describes how the simulated TDR waveform can be derived. The dataset needed to be available when computing this time domain response is simply made of

$H^{(i)}(\omega)$ The frequency response of the line at the reflectometry port (node i)

$v_S(t)$ A time domain representation of the stimulus signal.

A treacherous ambiguity arises when extending the two-port representation of Figure 4.1 so that every component of a typical TDR measurement system is taken into account. The most generic setup has been depicted as a block diagram in Figure 1.4, from which the missing elements can be retrieved and analyzed:

- An equivalent network of connectors and transitions
- A non ideal internal impedance for the generator
- The impedance of the digitizer.

Given these considerations, a more comprehensive model of typical TDR measurement setups can be derived. Such model is represented in Figure 5.1. The *Connectors* two-port networks model the full cascade of connectors, transitions and cables that stand between the generator and the measurement ports on one side and between the measurement port and the TDR probe input on the other.

In TDR measurement setups employing commercial Time Domain Reflectometers, one may usually assume that the first *connector* network and the Z_M impedance are negligible. Such components, in fact, would model internal connections in the instrument that are obviously not accessible nor introduce relevant effects in the measurement model. Usually, instead, the second network represents an important issue, and major spurious reflections occur at the *TDR port*.

There are, indeed, certain conditions in which such issues can (almost) be neglected, that is:

- Z_S , the characteristic impedance of the *Connectors* network(s) are matched, i.e. the reflection coefficients at the *generator port* and at the *TDR port* are ~ 0
- The length of the interconnections is neglectable with respect to the length of the TDR probe
- The minimum wavelength of interest is greater than the length of the interconnections.

If all the conditions hold, the *connectors* network(s) can be neglected and the calibration procedure is way simpler. This case is discussed in Section 5.2. Reflectograms reported in [5], [8], [12], [22] and many other works are produced with this category of experimental setups. In the cited papers, however, it is safe to ignore the effect of interconnections because their electrical length (up to tens of centimeters) is orders of magnitude lower than the electrical length of the probes (up to hundreds of meters). Spurious reflections are well visible, however, from a distributed measurement viewpoint, their effect is limited to introducing a “blind spot” at the beginning of the TDR probe.

However, in many applications [17], [18], [31], [74] probes that are even shorter than the cable used to connect them to test equipment are employed. A typical example directly referring experimental practice is given in Figure 5.2, where a rod-like probe for the measurement of soil dielectric properties is sketched. The typical length of the probe goes up to tens of centimeters, while coaxial interconnections can be several meters long.

Referring Figure 5.1, a reasonable model for a measurement setup involving a Time Domain Reflectometer and the probe in Figure 5.2, that is widely used in soil measurement applications, must involve the second *Connectors* network, that at least takes into account the delay introduced by the coaxial cable.

In the most general case, instead, where one or more conditions are not met, the calibration procedure requires more steps, that are discussed in Section 5.3.

On a side note, most measurement setups introduced in this Chapter will not rely on commercial TDR units. This choice has been made to underline the generality of the presented approach and its versatility in that even “unconventional”

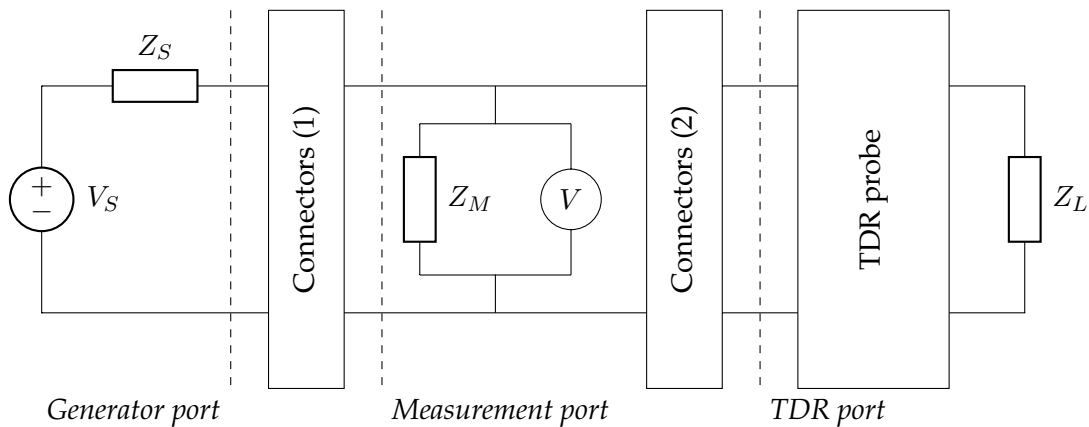


FIGURE 5.1: Realistic model of a TDR measurement setup

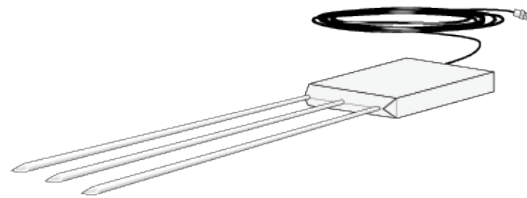


FIGURE 5.2: Campbell Scientific CS605 3-Rod TDR Probe with RG58 Cable [75]

reflectometry-based distributed sensing systems can be easily simulated with a suitably built model that translates complex EM configurations into simple and easy-to-solve electrical circuits.

Moving reference planes Readers that are well accustomed to Vector Network Analyzer measurements of S-parameters will immediately realize that the calibration problem covered in this Chapter is closely related to *reference plane shifting*. It is indeed true that Time Domain Reflectometry is tightly correlated to the measurement of S_{11} in Vector Network Analysis. As in VNA measurements, however, it often happens that the desired reference plane (that is the *TDR port* in Figure 5.1) is not directly accessible for practical reasons.

Basically, moving reference planes means “compensating” the effect of networks standing between the current reference plane and the desired one, so that measured data only reflects the influence of the Device Under Test. Almost any RF/Microwave simulation suite allows to perform this task intuitively.

Unfortunately, when only time domain measurements are available as in the framework of this thesis, this task is not straightforward as in VNA practice. In the Sections that follow, the simulation approach to distributed sensing proposed in Chapter 4 will be applied to real life measurement setups that range from the

simplest situation where only interconnections influence the measurements to the most general case of Figure 5.1. The theory of two-port devices will be applied to “calibrate out” the effects of connectors and other unknown impedances.

Validation of calibration procedures All the procedures outlined in this Chapter are strongly measurement-oriented and, therefore, experimental results on relevant case studies are presented. In order to validate the proposed calibration methods, measured and simulated waveforms need to be compared, and a unique, scalar error figure needs to be chosen.

Let $v_{meas}^{(i)}$ and $v_{sim}^{(i)}$ be the i -th samples of the measured and simulated reflectograms respectively. The accuracy of each calibrated measurement will be assessed with the following error figure:

$$e_{TDR} = \sqrt{\frac{\sum_i [v_{meas}^{(i)} - v_{sim}^{(i)}]^2}{\sum_i [v_{meas}^{(i)}]^2}} \quad (5.1)$$

that is the ratio between the Euclidean norms of the error vector and the vector of measured samples.

This quantity is normalized to the norm of the measured signal, thence enabling easy comparison among calibration results.

At this point, one important matter regarding the proposed approach must be discussed. This approach to distributed measurements *implies calibration* or, in other words, it would not make sense to perform without even acquiring the stimulus signal. The concept of uncalibrated measurements that is typical of VNA practice cannot, therefore, be applied. It can, however, be extended to the case where only the stimulus signal is calibrated, neglecting interconnections and other non-ideal behaviors. This case is covered in Section 5.2, and will be used as a term of comparison for more complex calibration procedures.

Use and misuse of the word “calibration” The “calibration” entry of the International vocabulary of metrology (VIM) [76] quotes as follows:

calibration

operation that, under specified conditions, in a first step, establishes a relation between the **quantity values** with **measurement uncertainties** provided by **measurement standards** and corresponding **indications** with associated measurement uncertainties and, in a second step, uses this information to establish a relation for obtaining a **measurement result** from an indication

[...]

NOTE 2 Calibration should not be confused with **adjustment of a measuring system**, often mistakenly called “self-calibration”, nor with **verification** of calibration.

The “adjustment of a measuring system”, on the other hand, quotes:

adjustment of a measuring system

adjustment

set of operations carried out on a **measuring system** so that it provides prescribed indications corresponding to given **values** of a **quantity** to be measured

[...]

NOTE 2 Adjustment of a measuring system should not be confused with **calibration**, which is a prerequisite for adjustment.

Following the VIM, one might object that this Chapter is actually dedicated to the “adjustment of TDR measuring systems”. This is true indeed, however an ambiguity arises because the information obtained with the procedures hereby indicated is used to “prepare” the system for the actual measurement step, that is something closely related to proper **calibration**.

All this considered, the word **calibration** is going to be used, although somehow improperly, in the remaining Sections of this Chapter.

5.2 Stimulus calibration

Let us now consider the simplest possible TDR configuration. Back in Chapter 4, and specifically in Figure 4.1, the two-port model of a distributed sensing system has been given, underlying that, for real life setups, this would be an oversimplified model. Let us also consider an experimental setup where the DUT is orders of magnitude longer than the cable that connects the signal generator to the probe input port (Figure 5.3(a)). In Figures 5.3(b) and 5.3(c), unconventional yet effective TDR setups employing the aforementioned cables are represented.

In the first configuration, an Agilent 33250A 80 MHz Arbitrary Waveform generator with BNC output is used to generate a pulse-like stimulus that is fed to a $\sim 50\text{m}$ long RG58-CU coaxial cable left open ended through a $\sim 0.3\text{m}$ long RG58-CU interconnection cable. In this case it can safely be assumed that the generic model in Figure 5.1 can be simplified as shown in Figure 5.4(a).

Considering that v_S cannot be measured directly and assuming that both Z_S and Z_M are known quantities, a good estimate of v_S is obtained by simply disconnecting the TDR probe, as in Figure 5.4(b) and acquiring the voltage at the measurement port. By applying the voltage divider equation in the frequency domain, we get

$$V_M = V_S \frac{Z_M}{Z_M + Z_S} \quad (5.2)$$

From which, with trivial manipulations, V_S can be obtained:

$$V_S = \frac{Z_M + Z_S}{Z_M} V_M \quad (5.3)$$

Equation 5.3 depends on the measured waveform and on both the generator and the measurement port impedances, therefore it can be applied to any measurement configuration in which interconnections are negligible. One can also observe that,

when high-impedance acquisition instrumentation is employed (i.e. $Z_M \gg Z_S$), $V_S \simeq V_M$.

This simple technique, however, helps taking into account also the reactive parts of Z_S and Z_M . Not doing so might, in some practical applications, result in non-negligible errors when comparing simulated and measured waveforms.

5.2.1 Experimental results for v_s

To conclude the discussion on this basic time domain calibration procedure, two examples of oscilloscope-based reflectometry setups will be calibrated and waveforms will be shown. MATLAB code snippets will be used alongside equations to keep the discussion as pragmatic as possible. Full code listings that have been used to generate the results hereby presented are also included in Appendix A.

Basically, performing the v_s only calibration procedure simply consists in implementing Equation 5.3. The voltage divider can be, in fact, interpreted as a simple transfer function, that can be straightforwardly applied in the frequency domain to a Fourier representation of the measured waveform v_M :

$$H(\omega) = \frac{Z_M + Z_S}{Z_M} \quad (5.4)$$

In the most general case, Z_M and Z_S both depend on the frequency, so the simplest way to take this dependency into account is to represent them as anonymous functions, e.g.:

$$Z_m = @(w) 1 ./ (1/Rm + 1i*w*Cm);$$

Z_m represents the parallel resistance (R_m) - capacitance (C_m) model for an oscilloscope channel. A similar approach can be adopted, if needed, to model the source impedance Z_s that, for the Agilent 33250A Arbitrary Waveform Generator, can simply be assumed as a 50Ω resistor, so that, in the most general case:

$$H = (Z_m(w) + Z_s(w)) ./ Z_m(w);$$

This transfer function must then be applied to the non-shifted FFT of the measured signal, therefore its values at negative frequencies must be mirrored and appended to the H variable:

$$H = [H; 0; conj(H(end:-1:2))];$$

So that, finally, the transfer function can be applied and the time domain signal can be computed by means of the Inverse FFT function:

$$\begin{aligned} V_m &= \text{fft}(v_m) / \text{length}(v_m); \\ V_s &= H .* V_m; \\ v_s &= \text{ifft}(V_s) * \text{length}(V_s); \end{aligned}$$

Experimental results are depicted in Figure 5.5, where the dashed line represents the measured waveform, while the solid one is its calibrated counterpart. The calibration has been performed on a Tektronix MSO71254C oscilloscope, with $50\Omega/5\text{pF}$ channel input impedance. The actual setup is depicted in Figure 5.3(b).



(a) Photo of a 50m long RG58-CU coaxial cable (DUT) and a 30cm long RG316 coaxial cable (connector)

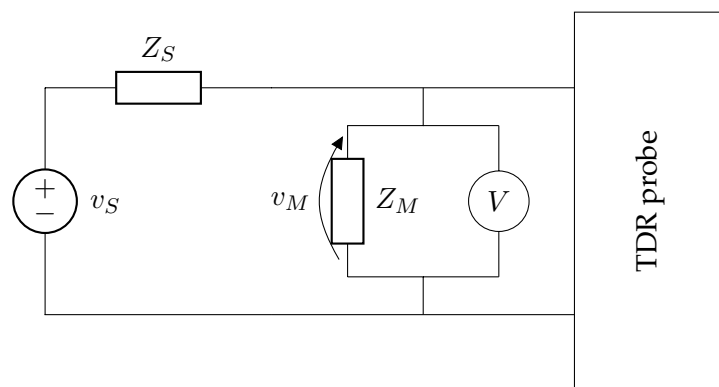


(b) TDR setup with an Arbitrary Waveform Generator (pulse signal with ~ 10 ns width) and an oscilloscope channel

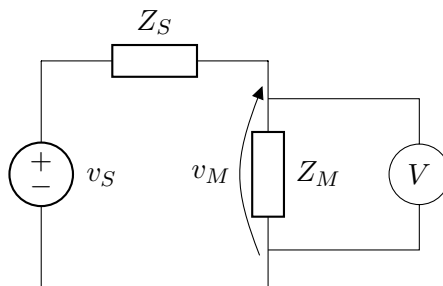


(c) TDR setup with a fast edge (~ 200 ps rise time) generator and an oscilloscope channel

FIGURE 5.3: Basic TDR setup with negligible interconnections



(a) TDR circuit



(b) Calibration circuit

FIGURE 5.4: TDR network model and calibration circuit (negligible interconnections)

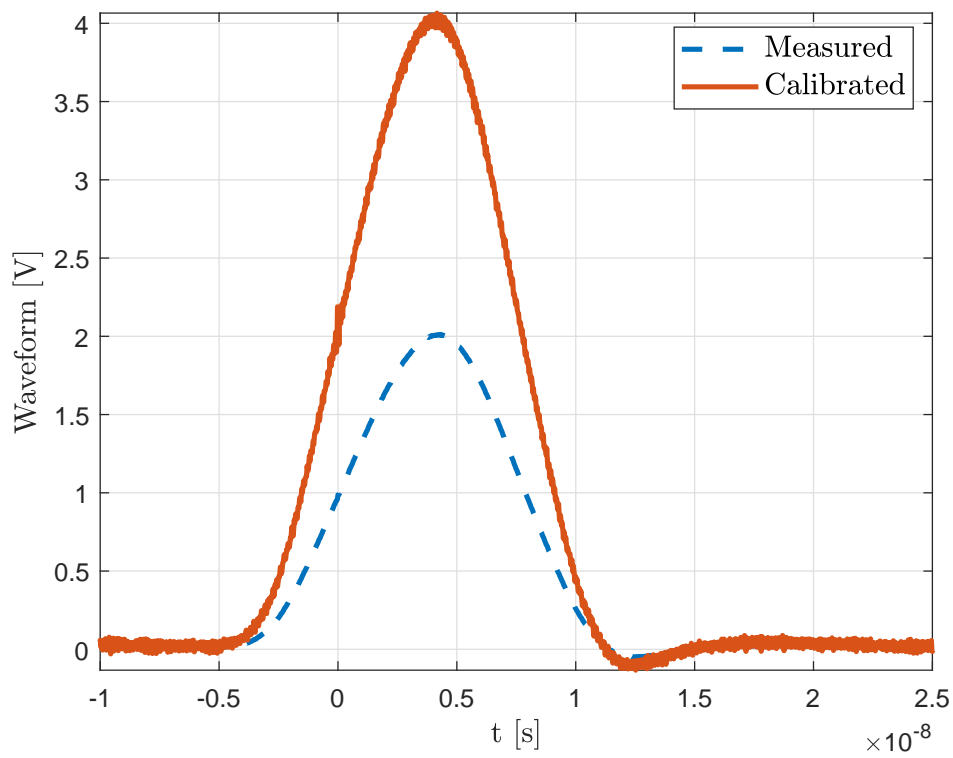


FIGURE 5.5: Calibration of an 8ns pulse stimulus supplied by Agilent 33250A AWG through a short RG58-CU cable

TABLE 5.1: Simulation parameters for a ~ 50 m long RG58-CU coaxial cable

Parameter	Value [unit]	Description
Model	coax	Transmission line model
l	51.4 m	Cable length
r_i	0.455 mm	Internal connector radius
r_o	1.475 mm	Dielectric radius
t	0.01 mm	Shield thickness
ϵ_r	2.1	Relative permittivity of the dielectric
$\tan \delta$	0.00028 3 GHz	Loss tangent of the dielectric
σ_c	5.97×10^7 S/m	Copper conductivity

Sample application of v_s only calibration The procedure hereby presented has been applied to the case study depicted in Figure 5.3(b), neglecting both the cable that connects the Arbitrary Waveform Generator to the oscilloscope and the T-connector. The parameters used for the simulation are reported in Table 5.1, and the experimental results are shown in Figure 5.6.

The error figure obtained as in Equation 5.1 from the waveforms in Figure 5.6(a) is $e_{TDR} \simeq 0.28$. As clearly visible in Figure 5.6(b), the main source of error lays in the second-order reflection. This is due to the fact that the (however small) impedance mismatch introduced, at the measurement port, by the T-connector and by the shorter cable has been neglected. The error can be further reduced by taking into account the delay introduced by the ~ 20 cm long cable.

From Figure 5.6(a) an important feature of the proposed approach arises, that is the possibility, with unconventional TDR setups, to exploit any required number of secondary reflections to refine the model in the calibration phase and achieve more accurate results at run time, i.e. when actual measurements are performed.

5.3 Full featured calibration procedure

In this Section, every component in Figure 5.1 will be taken into account, and a full calibration procedure for both v_S and the connectors network will be outlined. This complex situation finds immediate application to some real-life reflectometry-based configurations:

- Non-negligible mismatch between generator and probe
- Custom made TDR setups based on cheap stimulus hardware (e.g. fast logic gates)
- TDR probes only accessible via non-negligible intermediate Transmission Lines
- Any combination of the previous conditions.

For the first case, the need to introduce the “connectors network” in the model arises; such network might be another Transmission Line that, however, is not part of the

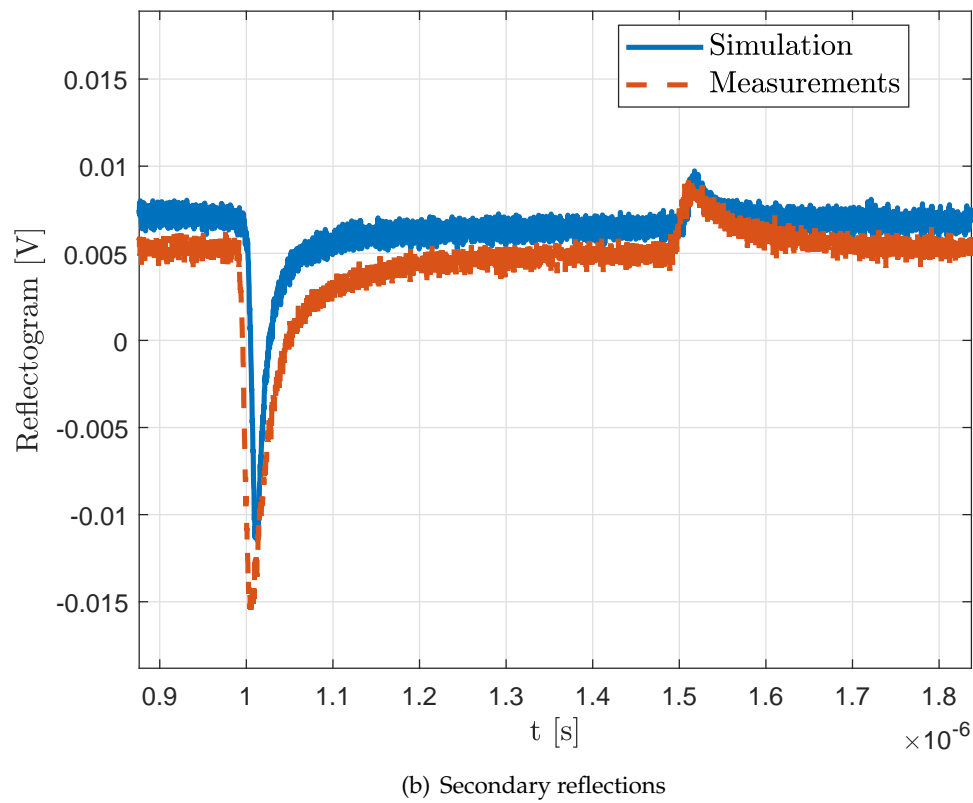
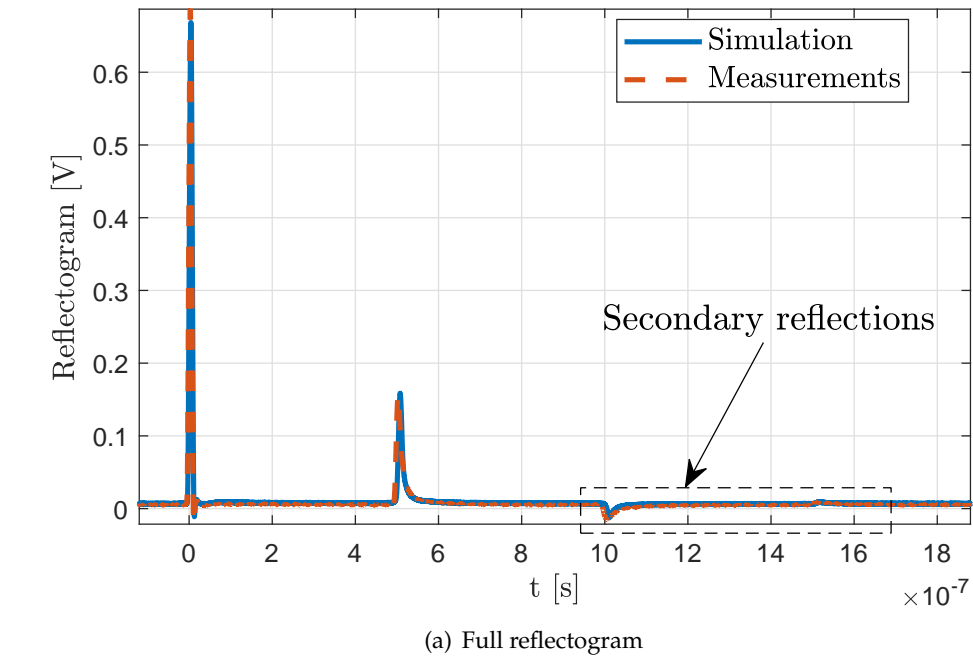


FIGURE 5.6: TDR waveform measured on a $\sim 50\text{m}$ long RG58-CU coaxial cable with a $\sim 10\text{ns}$ wide pulse-like stimulus (Fig. 5.5)

sensing hardware and, therefore, can be assumed not to change under normal operating conditions.

The second case requires the estimation of the internal impedance of the stimulus generator. This condition arises any time hardware cheaper than a laboratory-grade AWG or a commercial TDR unit are used to drive the TDR probe.

Finally, the third case requires a shift of the reference plane. This situation arises in many setups already presented in literature (e.g. [5]) and is seldom treated as an issue, since the mismatch between the TDR probe and the intermediate TL produces a peculiar issue in the reflectogram that can be approximately used to point out the beginning of the probe directly from the reflectogram. As previously discussed, this way of processing reflectograms may be well suited for some specific cases, but finds its implicit limitation in generic distributed sensing applications, where the propagation velocity of the stimulus in the probe is not constant.

5.3.1 Connectors network calibration

This is the first and possibly trickiest calibration task. Calibrating out the effects of the Connectors network consists in introducing a suitable circuit representation of the network in the overall simulation model, thence taking into account how it shapes and delays the stimulus and the reflections at its ports due to impedance mismatches with the generator and the TDR probe, if any.

There are at least two ways to obtain this circuit representation:

- Preliminary simulations
- VNA measurements

The first approach can be followed if a Vector Network Analyzer is not available or if the Connectors network is a standard cable of some sort, whose electrical parameters and geometry are considered perfectly known. This way of proceeding, however, may lead to non negligible inaccuracies, as shown in Figure 5.7. In the Figure, the measured magnitude of the S_{11} parameter is compared with its simulated values obtained with software simulations employing the data provided by the manufacturer of the cable [77]. Other Figures, including $\angle S_{11}$ and S_{21} are omitted for the sake of brevity. Although the orders of magnitude show a good match, using simulated instead of measured data may lead to inaccuracies in the calibrated stimulus.

Therefore, finally, it is highly recommendable, when possible, to perform direct VNA measurements on the Connectors network. Such results must then be converted to impedance matrices if they need to be employed in further calibration steps, as will be shown in the next Section. To do so in presence of complex source and load impedances is nontrivial, and a suitable method such as that proposed by Frickey [78] must be applied.

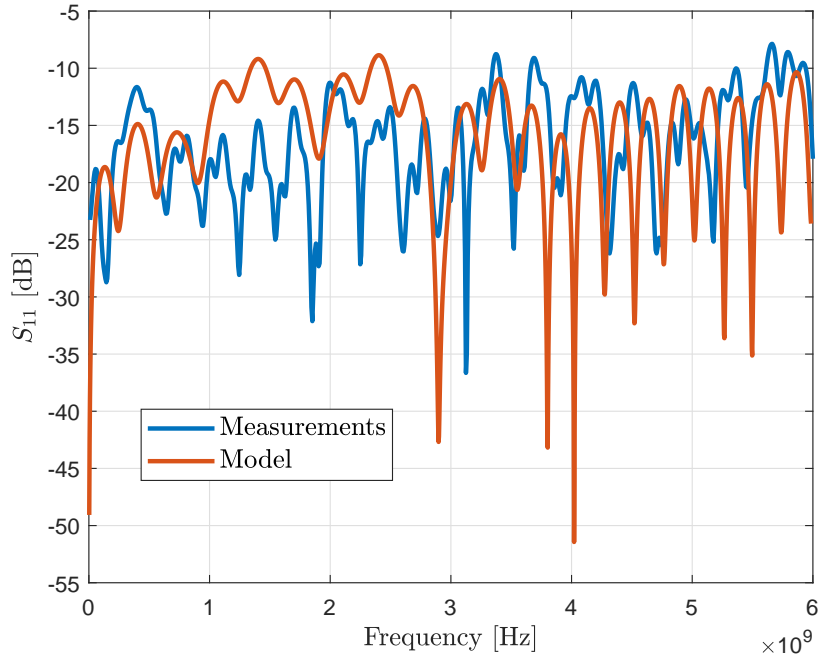


FIGURE 5.7: $|S_{11}|$ for a 40 cm long RG316-U cable: model versus actual measurements

5.3.2 Generator internal impedance calibration

The calibration equivalent circuit is shown in Figure 5.8. In this case, the Z-parameters matrix has been chosen for the connectors network, because it greatly simplifies the computations. In this case, both V_S and Z_S are unknown.

By applying Kirchoff's voltage laws to both meshes in the circuit, the following two equations are promptly obtained:

$$\begin{cases} V_S = (Z_S + z_{11}) I_1 + z_{12} I_2 \\ z_{21} I_1 = (z_{22} + Z_L) I_2 \end{cases} \quad (5.5)$$

Assuming that all the z_{ij} parameters are known from previous measurements or model of the interconnections, it can be pointed out that the System 5.5 has two Equations and four unknowns (I_1, I_2, Z_S, V_S). The voltage across the load impedance, however, can be directly measured, therefore the current I_2 can be obtained as

$$I_2 = -\frac{V_M}{Z_L} \quad (5.6)$$

There is still one more degree of freedom that needs to be eliminated. This can be achieved by performing two measurement with different load impedances, as shown in Figure 5.9. Letting, therefore, $Z_L^{(1)}$ and $Z_L^{(2)}$ be, in general, any non-equal

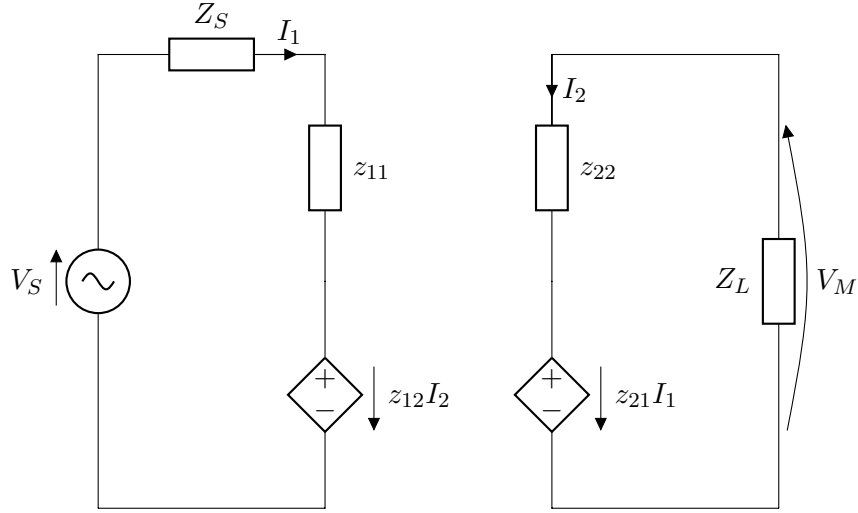


FIGURE 5.8: Calibration equivalent circuit for the estimation of v_S and Z_S

load impedances, and using Equation 5.6, the System 5.5 becomes

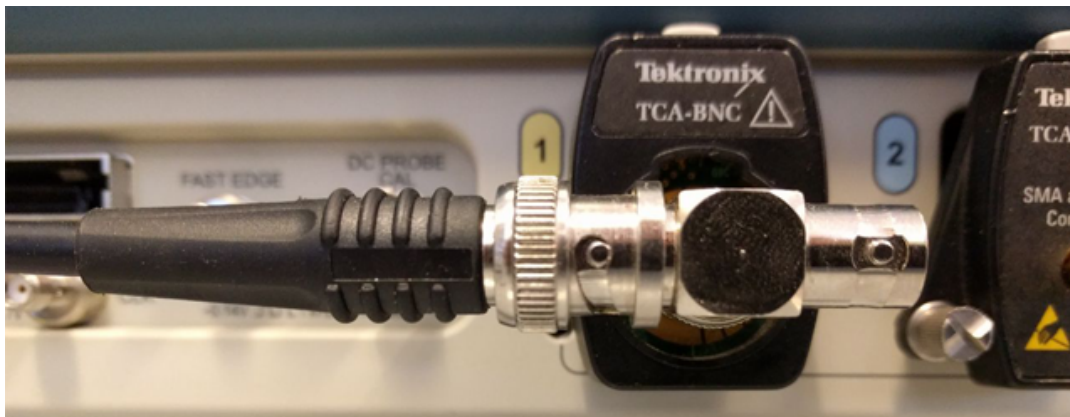
$$\begin{cases} V_S = (Z_S + z_{11}) I_1^{(1)} + z_{12} I_2^{(1)} \\ z_{21} I_1^{(1)} = (z_{22} + Z_L^{(1)}) I_2^{(1)} \\ V_S = (Z_S + z_{11}) I_1^{(2)} + z_{12} I_2^{(2)} \\ z_{21} I_1^{(2)} = (z_{22} + Z_L^{(2)}) I_2^{(2)} \\ I_2^{(1)} = V_M^{(1)} / Z_L^{(1)} \\ I_2^{(2)} = V_M^{(2)} / Z_L^{(2)} \end{cases} \quad (5.7)$$

System 5.7 has a single unique solution. First, the currents flowing in both meshes can be explicitly derived using Equations 2, 4, 5 and 6 of 5.7:

$$\begin{cases} I_1^{(1)} = \frac{z_{22} + Z_L^{(1)}}{z_{21} Z_L^{(1)}} V_M^{(1)} \\ I_1^{(2)} = \frac{z_{22} + Z_L^{(2)}}{z_{21} Z_L^{(2)}} V_M^{(2)} \\ I_2^{(1)} = V_M^{(1)} / Z_L^{(1)} \\ I_2^{(2)} = V_M^{(2)} / Z_L^{(2)} \end{cases} \quad (5.8)$$

Finally, from Equations 1 and 3 of 5.7, the required variables V_S and Z_S can be derived:

$$\begin{cases} Z_S = \frac{z_{11}(I_1^{(2)} - I_1^{(1)}) + z_{12}(I_2^{(2)} - I_2^{(1)})}{I_1^{(1)} - I_1^{(2)}} \\ V_S = (Z_S + z_{11}) I_1^{(1)} + z_{12} I_2^{(1)} \end{cases} \quad (5.9)$$

(a) $Z_L = Z_M$ (b) $Z_L = Z_M \parallel Z_C$ FIGURE 5.9: Two configurations for v_S and Z_S calibration

Sample application of v_S and Z_S calibration As already discussed, the simultaneous calibration of v_S and Z_S is required when measurements or a suitable model for the interconnections between the generator and the TDR probe are already available and the generator itself needs to be characterized. This could be the case of any unconventional TDR setup based on fast logic gates or fast edge generators (as in Figure 5.3(c)). The only data available regarding the fast edge generator in the Figure, e.g., are, quoting the oscilloscope manual,

Front panel. SMA connector provides fast edge signal. 1 kHz $\pm 20\%$; 810 mV (base to top) $\pm 20\%$ into ≥ 10 k Ω load; 440 mV $\pm 20\%$ into a 50 Ω load

There is no information about the internal impedance of the generator and, moreover, the declared uncertainties are definitely unsuitable to produce a good model of the stimulus (step-like) signal.

The signal has been measured, as shown in Figure 5.9, with two load configurations:

- Measurement port impedance only ($Z_L = Z_M$)
- Measurement port in parallel to a 50 Ω termination ($Z_L = Z_M \parallel Z_C$)

No data about the 50 Ω termination were available, therefore a VNA (National Instruments NI PXIe-5632) was used to measure its impedance from 10 MHz up to a few GHz (Figure 5.10). More in detail, the VNA has been used to measure the S_{11} scattering parameter referred to $Z_0 = 50\Omega$, and the impedance of the terminator has been computed with the relation

$$Z_C = Z_0 \frac{1 + S_{11}}{1 - S_{11}} \quad (5.10)$$

This information has been used as a lookup table for the MATLAB implementation of Equations 5.8 and 5.9, that resulted in the waveforms plotted in Figure 5.11.

The waveforms in the Figure are actually the derivatives of the step signal physically generated by the fast-edge generator. Treating them instead of the original signal does not influence any consideration made on the devices under test because the system is considered linear.

There are a few interesting features that need to be pointed out. First, the calibration has been performed by assuming, for a RG316-U cable similar to that in Figure 5.3(c) but ~ 40 cm long, a coaxial line model with the typical geometry and electrical parameters given in its datasheet [77]. Such model has been built with a slightly modified version of LineLab, with which the impedance matrix has been directly computed by applying the classic superposition principle to the Z-representation of a two-port network:

$$\begin{aligned} z_{11} &= \left. \frac{V_1}{I_1} \right|_{I_2=0} & z_{12} &= \left. \frac{V_1}{I_2} \right|_{I_1=0} \\ z_{21} &= \left. \frac{V_2}{I_1} \right|_{I_2=0} & z_{22} &= \left. \frac{V_2}{I_2} \right|_{I_1=0} \end{aligned} \quad (5.11)$$

The computed network introduces an approximate delay of 1.95ns, that matches the length of 40cm at a propagation velocity of 200×10^6 m/s.

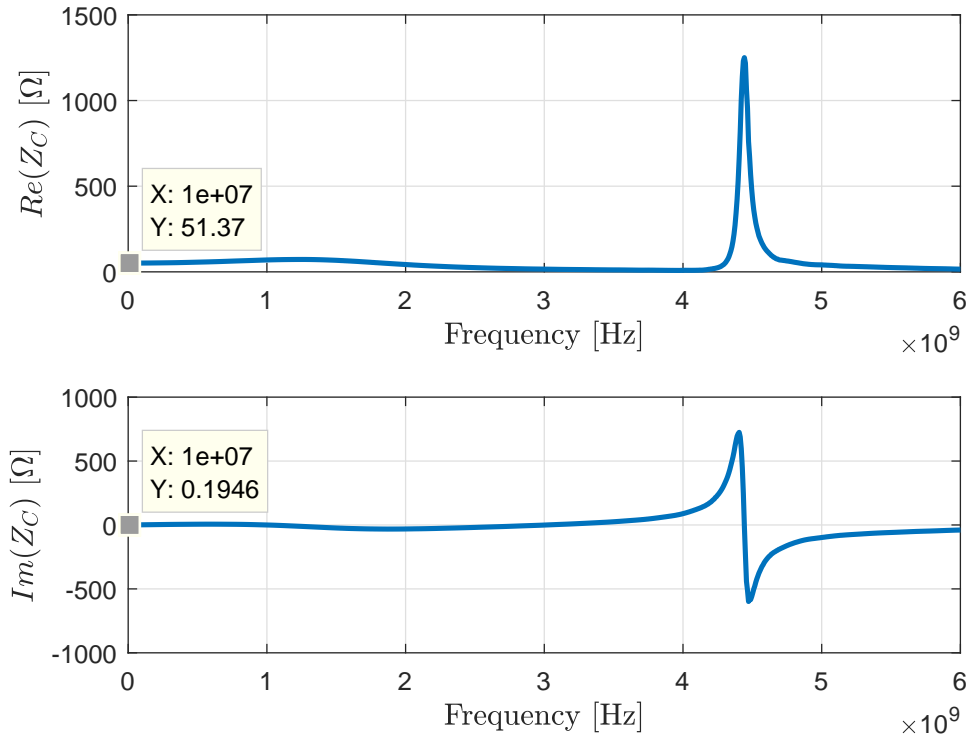


FIGURE 5.10: Measured (NI PXIe-5632 VNA) terminator impedance

Moreover, the estimated source impedance shows real part around 45Ω , that is compatible with the specifications given by the oscilloscope manual (810 mV into high-impedance loads and 440 mV into 50Ω).

5.3.3 Shifting the reference plane

For this last case, only some examples will be given because, given the architecture of the LineLab Simulator, it simply requires to perform any other calibration step and to compute the response of the modeled system at a port different than the first, that can be programmatically set. Furthermore, in order to reduce the computational effort, the interconnection can be reduced to a two-port admittance network, as shown in Section 5.3.1.

Although this procedure has been included in the calibration Section, it may be considered completely optional, as it only helps compensating the effect of the rightmost “connectors” network (Figure 5.1) and focusing on the TDR probe directly in the time domain.

A synthetic example is shown in Figure 5.12. In the Figure, the leftmost “connectors” network of Figure 5.1 is neglected, while the rightmost one is a 1m long coaxial cable, and the TDR probe is a 10m long bi-wire. This configuration is typical of TDR systems where the TDR probe cannot be directly accessed (e.g. is buried).

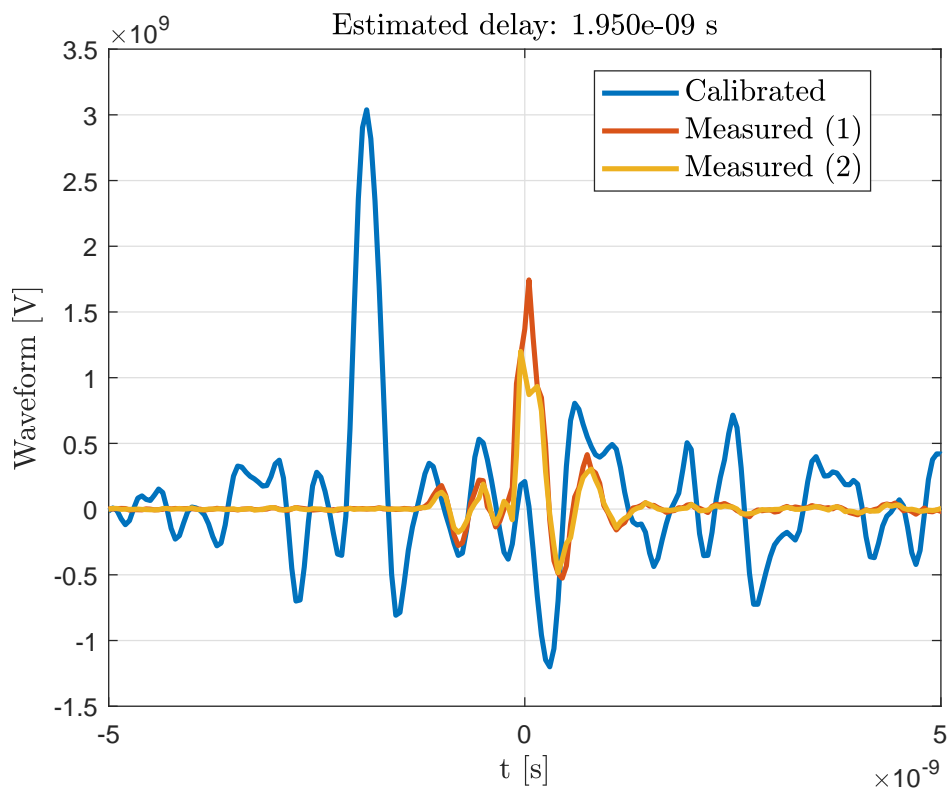


FIGURE 5.11: Measured derivatives of the step-like stimulus signal from the fast edge generator of Tektronix MSO71254C oscilloscope and its calibrated counterpart

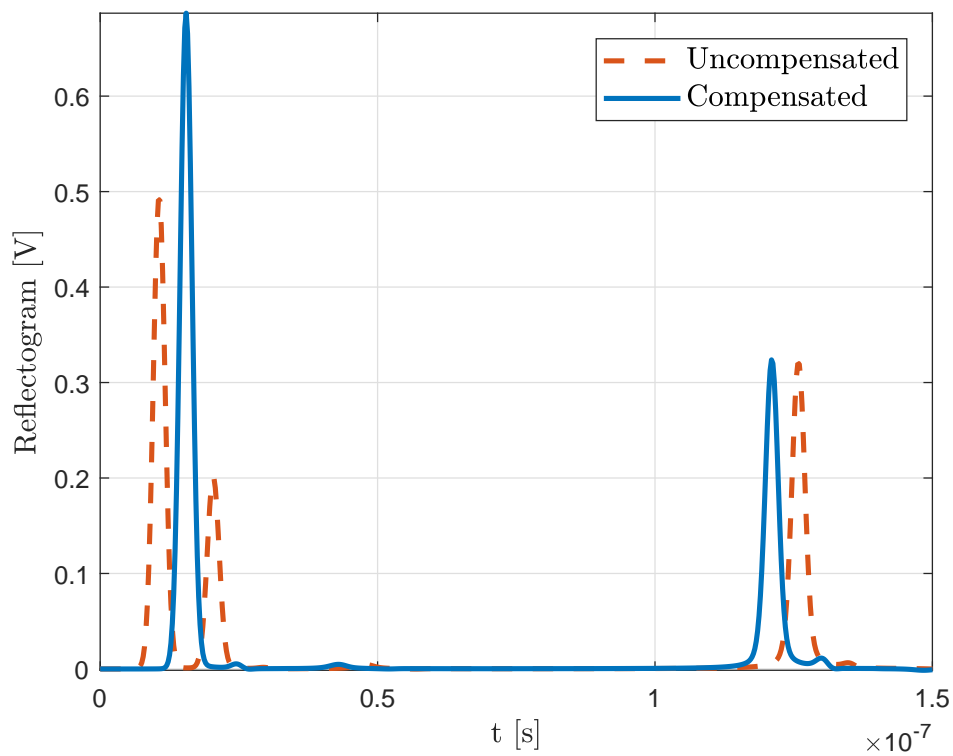


FIGURE 5.12: Compensated and uncompensated reflectograms simulated with a 1m long coaxial line preceding a 10m long bi-wire. The solid line simulates the time domain response taken by shifting the reference plane to the interface between the lines

Chapter 6

Simulation-based reconstruction of distributed parameters

Dare to rise, when all voices behind you say you can't get there, ignore them and move on... it's not about the talents and gifts you have; it's about how wise you optimize them!

ISRAELMORE AYIVOR, LEADERS' WATCHWORDS

6.1 Introduction

In this Chapter, the fully calibrated TDR system model built with the approach presented in Chapters 4 and 5 will be used to reconstruct TL parameters. Optimization algorithms have been applied to this problem and they will be thoroughly presented and compared.

The most interesting quantities that can be estimated are, of course, the primary parameters of the line $L(x, \omega)$, $R(x, \omega)$, $G(x, \omega)$, $C(x, \omega)$, all of which are, in general, real functions of the position on the line x and of the angular frequency ω . For example, the dielectric constant profile along a TDR probe is solely related to the capacitance per unit length if dielectric losses are neglected, or is related to both C and G if the losses are taken into account.

The process of reconstructing a set of parameters that, used in a suitable mathematical model, faithfully reproduce measured TDR waveforms is called *TDR inversion* [79]. Generally speaking, for the set of problems under analysis, the inversion process can intuitively be outlined with an iterative algorithm. Let:

θ	Set of parameters under estimate
$v_m(t)$	Measured reflectogram
$v_s(t)$	TDR stimulus signal

The Inversion follows, in general, Algorithm 1. The actual implementation of the Algorithm may heavily depend on the choice of the parameter set θ for the specific application and, obviously, also on the assumptions that are made on them.

The general Algorithm 1 essentially describes a classic optimization routine. Optimization algorithms are a category of iterative procedures that find a set of parameters $\Theta = [\Theta_1, \Theta_2, \dots, \Theta_n]$ that are defined optimal in some sense. For the problem of TDR inversion as schematized above, the problem can be straightforwardly associated with the minimization of some scalar error function e_{TDR} that is somehow related to the distance between measured and simulated reflectograms. In other words, the best set of parameters Θ is the one that, given as input to the TL simulator introduced in Section 4.6 of Chapter 4, achieves the best “imitation” of the measured reflectogram.

Algorithm 1 TDR data assimilation algorithm

```

1: procedure TDR INVERSION( $\theta_0, v_m(t), v_s(t)$ )           ▷  $\theta_0$  initial guess for  $\theta$ 
2:    $\epsilon_{end} \leftarrow 1e - 6$                              ▷ Convergence value
3:    $\epsilon \leftarrow 1$ 
4:    $\theta_c \leftarrow \theta_0$ 
5:   while true do
6:      $v_c \leftarrow \text{LineLab}(\theta_c, v_s(t))$              ▷ Simulation of a TDR waveform
7:      $\epsilon \leftarrow f(v_c, v_m)$                        ▷  $f(\cdot)$  represents a convergence criterion
8:     if  $\epsilon < \epsilon_{end}$  then
9:       break
10:    end if
11:     $\theta_c \leftarrow \text{NewParamSet}(\cdot)$                ▷ New  $\theta_c$  for next iteration
12:  end while
13:   $\theta_{out} \leftarrow \theta_c$                            ▷ Final estimation of the parameters set
14: end procedure

```

6.2 Choice of the parameters set

In Chapter 4 the idea of simulating arbitrary profiles of the primary parameters has been outlined, and in this Chapter the final connection between TL simulation and distributed measurements will be established. First, a brief recall of what is the information that could, in the distributed sensing framework, be extracted from reflectograms. The (local) variations of the four primary parameters can be related to a broad range of phenomena, e.g.

$L(x, \omega)$ fault modeling in distribution networks [80]

$R(x, \omega)$ worn or broken cables [81]

$C(x, \omega)$ variation in the dielectric properties of a material (e.g. in leak detection [5] and diagnostic on concrete structures [2], etc.)

$G(x, \omega)$ transmission line shunt conductance characterization [82]

and many more. Considering the simulation algorithm, it immediately becomes evident that extracting the profiles, even just one of them, without making any assumption is unfeasible. This would, in fact, mean, in the discrete world, estimating

the value of the parameter under test for each of the N_x elementary cells that make up the TDR probe model, typically more than 10^4 .

Instead, it is feasible and safe to assume that the parameter under test follows simpler mathematical models that are chosen on the basis of application-driven workflows. Such models can be completely different depending on what are the features sought by the designer.

In the following Sections some sample applications will be introduced, also taking into account the case studies proposed in Section 4.7, and the workflow leading to the choice of the parameters set will be outlined. Frequency-dependent behaviors will not be considered in the examples, however they can and must be taken into account, when needed, by adopting similar workflows as those introduced for position-dependent variations.

Two important conventions This Chapter deals with variations of the primary parameters on a given Transmission Line, assumed to have been *completely characterized in resting condition*. This means that at least two conventions can be established:

- The x coordinate can be expressed relatively to the (known) length of the line
- The profiles of the primary parameters can be expressed as relative variations with respect to their base values

Therefore, the following conditions will hold throughout the rest of the Chapter:

$$\begin{cases} x \in [0, 1] \\ \Delta X = \frac{X}{X_0} - 1 \end{cases} \quad (6.1)$$

where X can be R , L , G or C and X_0 its value in resting condition.

Finally, if absence of specific indication, the discretization of the proposed mathematical model does not present any relevant issue, therefore it is assumed that the discussion carried out considering $[0, 1]$ a continuous set can be trivially translated into the discrete context.

6.2.1 Concentrated capacitance faults

This is the simplest possible case study, where the choice of the set of parameters is straightforward. Although very simple, this case can also be applied to real life scenarios, such as the detection of faults in power Transmission Lines [83]. The mathematical expression for this profile is

$$\Delta C(x) = \sum_{i=1}^N A_i \delta(x_i) \quad (6.2)$$

where $\delta(x_i)$ is Dirac's delta function centered in x_i . If the expected number N of faults is known a priori, the parameter set for this estimation problem is

$$\Theta = [x_1, \Delta C_1, x_2, \Delta C_2, \dots, x_N, \Delta C_N] \quad (6.3)$$

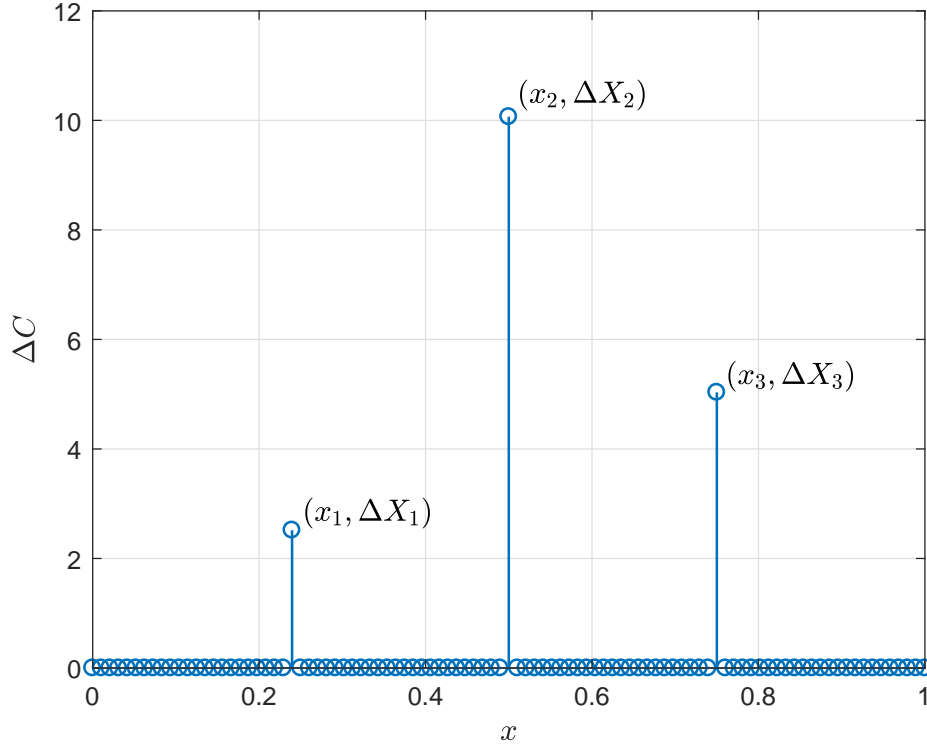


FIGURE 6.1: Capacitance profile with three concentrated faults

In this simple case, however, it is not mandatory to know how many faults are expected to be found if ΔX_i are allowed to be zero and N is assumed to be large enough. It has been, however, observed that although this is a reasonable assumption, it sometimes can cause the optimization routines to fail or to find suboptimal results trying to force the “activation” of more faults than needed.

While the location parameters, as stated in Equation 6.1, range from 0 to 1, the search domain for the amplitude parameters ΔC_i depends on the specific application.

6.2.2 Profile of capacitance as sum of Gaussian curves

In the simplest case, the capacitance profile can be expressed as follows:

$$\Delta C(x) = A \exp\left(\frac{x - \mu}{2\sigma^2}\right) \quad (6.4)$$

The set of parameters that need to be optimized, therefore, becomes simply

$$\Theta = [A, \mu, \sigma] \quad (6.5)$$

A lot could be told about the choice of the search domain for these three parameters. A single Gaussian curve is a simple yet effective model for a distributed fault that has a well defined center and somehow spreads around it. Therefore, the σ parameter cannot be expected to be higher than, say, 0.1 that is, however a completely arbitrary limitation.

The range for ΔC , instead, depends on the materials under test, but its choice is quite easy. Let us, e.g. consider the leak detection problem: normally, $\epsilon_r \sim 2.5$ for dry soil and $\epsilon_r \sim 40$ for wet soil, so the margins for ΔC are trivially computed. More advanced considerations about such margins can be made if FEM modal simulations are performed on the cross section of the TDR probe (as briefly pointed out in Appendix ??). The computation of the effective dielectric constant ϵ_{eff} as function of the dielectric constant of the soil surrounding the probe can provide more detailed information and improve the performance of the optimization algorithms.

An interesting feature of Gaussian curves is that they can be composed and summed up to form smooth profiles. In Figure 6.2 two different scenarios are depicted. In the first (Fig. 6.2(a)) the two Gaussian curves do not overlap, while in the second (Fig. 6.2(b)) they do, and the resulting profile has a completely different shape. In both cases, the parameters set is

$$\Theta = [\mu_1, \sigma_1, A_1, \mu_2, \sigma_2, A_2] \quad (6.6)$$

For the applications in which the capacitance is expected to increase with respect to a base value, this solution can be very versatile and, as it will be shown later on, optimizing the aforementioned parameters achieves very good performance in terms of convergence.

6.2.3 Staircase-like profile of capacitance

In this case, the expression of $C(x)$ is

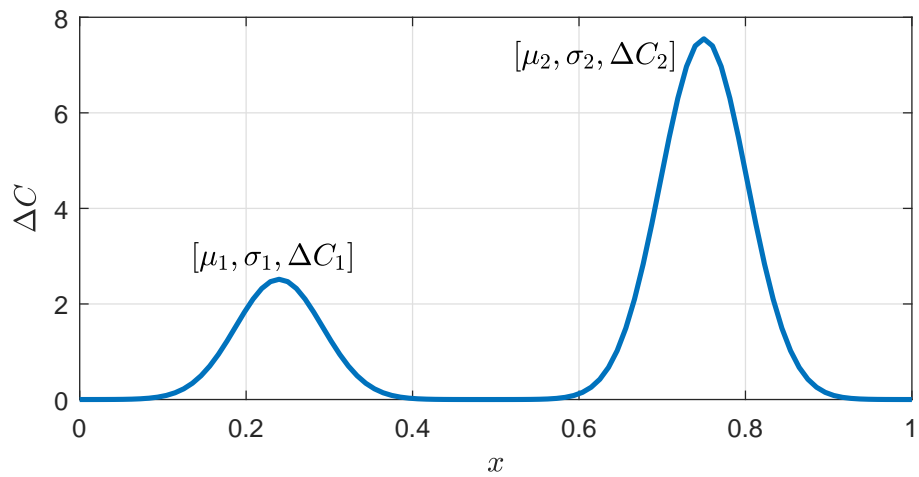
$$C(x) = C_0 + \sum_{i=1}^{i=N} A_i \text{step}(x_i) \quad (6.7)$$

In most applications the number N of capacitance steps, i.e. the number of interfaces between layered materials, is known a priori, therefore in this case the set of $2N$ parameters to be optimized is

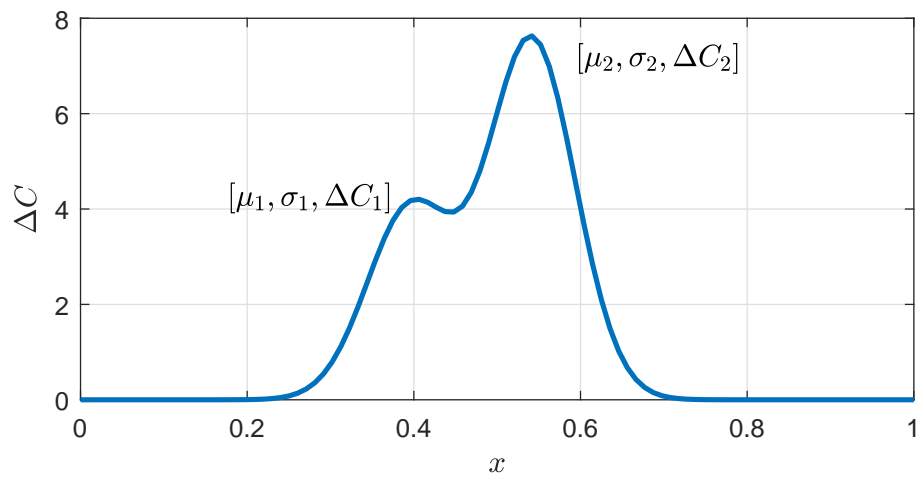
$$\Theta = [\Delta C_1, x_1, \Delta C_2, x_2, \dots, \Delta C_N, x_N] \quad (6.8)$$

Usually an abrupt change of dielectric constant provides a good enough model for real life applications (e.g. layered materials in petrochemical industry [10]), however a third parameter quantifying a transition zone between layers may be as well introduced, as shown in Figure 6.3(b), so that the set of parameters to be optimized becomes

$$\Theta = [\Delta C_1, x_1, \xi_1, \Delta C_2, x_2, \xi_2, \dots, \Delta C_N, x_N, \xi_N] \quad (6.9)$$



(a) Two separate Gaussian faults



(b) Two overlapping Gaussian faults

FIGURE 6.2: Composing a generic capacitance profile using Gaussian curves

Also in this case, the model can find an interesting extension to more general profiles. If, for instance, the ξ are assumed to be relatively high (e.g. $\xi \in [0.05, 0.1]$) and x_i are close enough to each other, generic sigmoid smooth profiles can be modeled, as found in wet soils when the TDR probes are placed vertically. In such cases, in fact, one expects to find a layer of completely dry soil at the top and an increasingly higher content of water when looking deeper underground.

6.2.4 Generic smooth profile of capacitance

Finally, the most generic case is introduced, that can be related to applications where no reasonable model can be assumed, i.e. no specific features are expected to be found in the sought profile. Let us, e.g., consider precision agriculture applications [84], in which one aims to measure the content of water of cultivated soil on large scales (tens to hundreds of meters). If, for instance, the goal is to keep this profile as uniform as possible, one does not expect the profile of capacitance along a TDR probe to have a totally erratic behavior. Instead, such profile is expected to be smooth.

For this and similar applications, the profile of capacitance (or any other needed parameter) can safely be approximated with its Fourier series expansion, as in Equation 6.10

$$\Delta C(x) = c_0 + \sum_{i=1}^{N_h} [a_i \cos(2\pi i x) + b_i \sin(2\pi i x)] \quad (6.10)$$

with $x \in [0, 1]$ as usual.

Unfortunately, no particular assumptions can be made in this case, whose solution is absolutely nontrivial. It must be granted that $\Delta C(x) \geq -1 \forall x$, otherwise the simulator would encounter negative capacitance per unit length that would be unphysical.

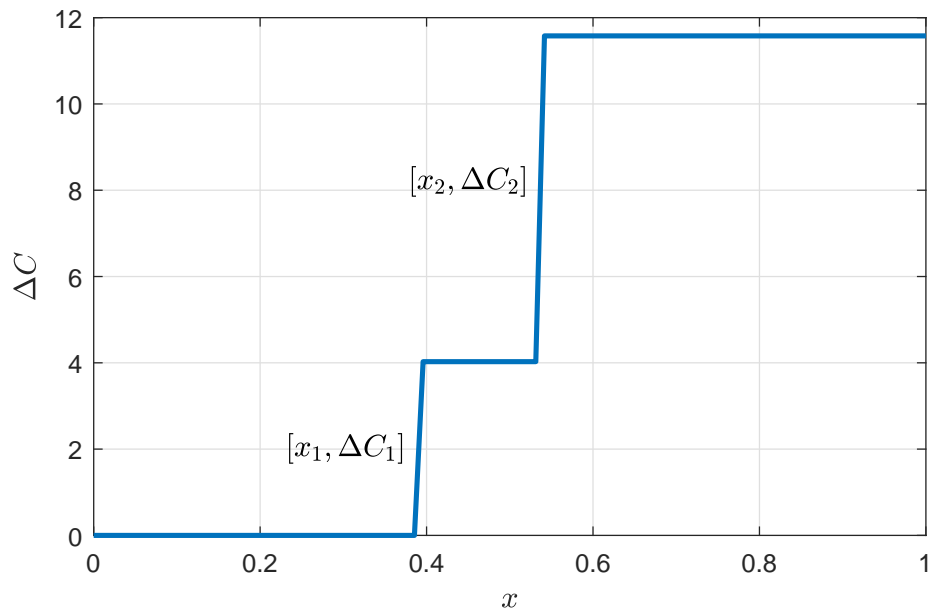
An advantage of this approach to modeling profiles is that almost any arbitrary profile can be obtained with a fairly small number of parameters. The size of the parameter set is $2N_h + 1$ where N_h is the number of terms after which the Fourier expansion is arrested.

6.3 Target function

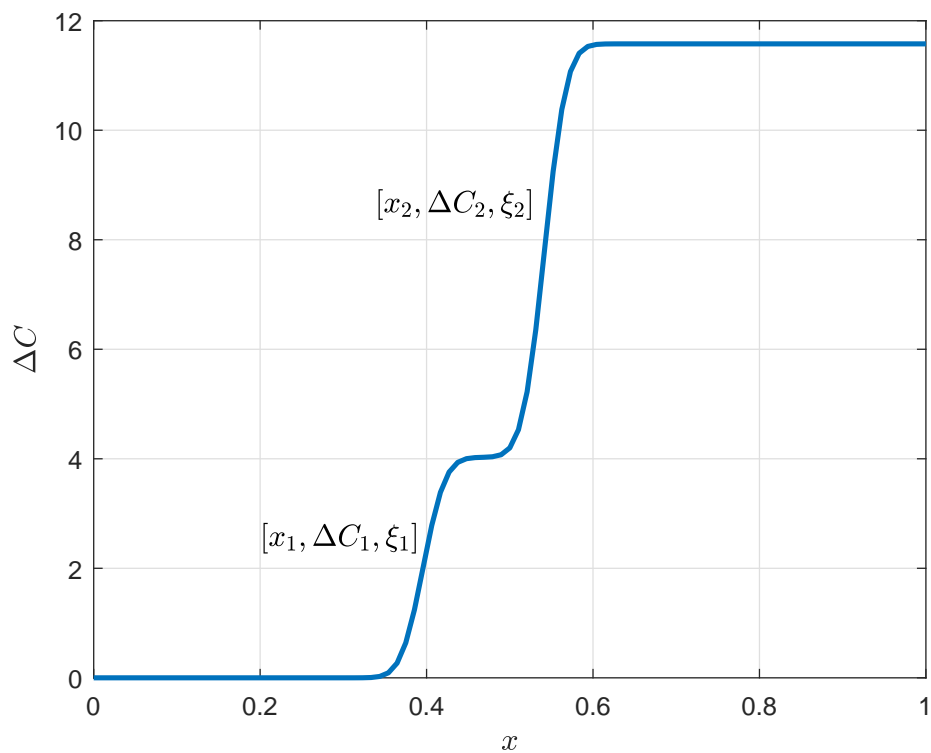
The comparison between two time domain waveforms is a well understood matter that applies to many fields, from speech recognition to biological signal analysis. There are, therefore, many similarity measures [85] that could be adopted to compute a so called “distance” between measured and simulated reflectograms.

The problem of choosing a suitable metric of distance to be used as target function for the optimization algorithms is at the same time a critical and difficult issue, given that such function must satisfy at least two criteria:

- Fast to be computed
- Should not be prone to local minima



(a) Abrupt changes in the dielectric constant of layered materials



(b) Smooth changes in the dielectric constant of layered materials

FIGURE 6.3: Staircase-like capacitance profiles

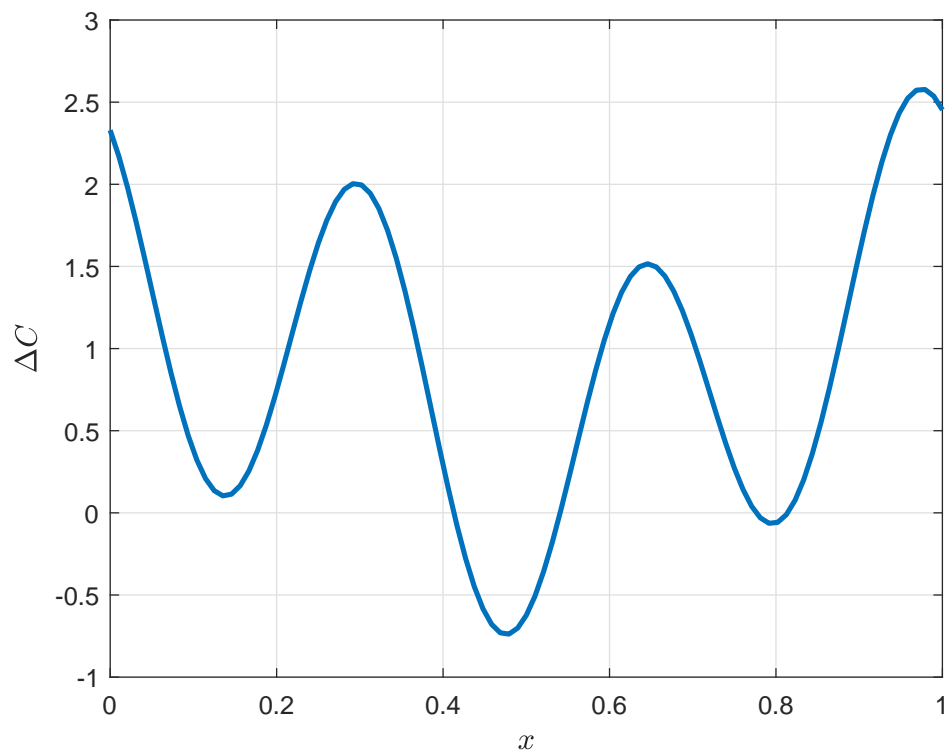


FIGURE 6.4: Generic smooth profile of capacitance

In Section 5.1, an error figure has been introduced for the assessment of the accuracy of calibration techniques. It has been found that it can be computed in negligible time and performs quite well, therefore a slightly modified version of the same error figure will be used as target function for the experimental results that will be presented in the next Section, i.e.

$$e_t = \left(\frac{\sum_i [v_{meas}^{(i)} - v_{sim}^{(i)}]^2}{\sum_i [v_{meas}^{(i)}]^2} \right)^{0.1} \quad (6.11)$$

where the 0.1 power instead of the simple square root, empirically found, eases the search for the global minimum.

Although this target function already provides satisfactory results, more complex and possibly robust target functions are still to be investigated, namely:

- Cross-correlation
- Dynamic time warping [86]

The cross-correlation, that is similar to the convolution of the two compared reflectograms, might be the simplest and most robust of the three, however a normalization criterion should be introduced. Moreover, the cross-correlation function is a time series itself and, therefore, some kind of feature or secondary measure on it should be found and used as definitive (scalar) value for the target function. However the maximization of cross-correlation has recently been applied in a speech recognition application [87], therefore it may be worth trying also in reflectogram matching.

The dynamic time warping, usually adopted in speech recognition and biometric data processing algorithms [88], [89], has been explicitly developed to measure the distance between time series and, therefore, could be an optimal choice, also because many efficient implementations (exhibiting as low complexity as $O(N)$) are currently available [90].

6.4 Synthetic optimization results

In this Section some examples of optimization results for the reconstruction of suitably selected profiles in a completely synthetic environment are presented. Such case studies serve as a proof of concept for the presented methodology and provide a preliminary overview about the potential applications of the reconstruction technique.

Although not meant to be completely exhaustive, the synthetic optimization results hereby presented, as the simplified models for distributed parameter profiles described in Section 6.2 aim to outline a general approach to distributed parameter reconstruction that is based on some basic principles, namely

- Accurate modeling of the measurement setup

- Acquisition and “calibration” of the stimulus signal
- Identification of a simplified parametric model for the profile(s) under test
- Choice of a suitable search range for the parameters that need to be optimized

In a completely synthetic environment, the first two principles are given for granted, while the last two are tested against increasingly more complex problems and some conclusions will be drawn. Error evaluations will also be performed with respect to true or expected values of the estimated parameters. As a general remark, letting θ be the true value of a parameter and $\hat{\theta}$ its estimated value, the relative error on the estimate of θ is

$$er_{\theta} = \frac{\theta - \hat{\theta}}{\theta} \quad (6.12)$$

In the following Sections, this error will be expressed as a percentage of θ ($100 \times er_{\theta}$).

A brief outline of Differential Evolution algorithms Although a specific discussion about optimization algorithms goes far beyond, it is important to give at least a rough idea about how the chosen algorithm works. The DE approach has already been applied to Electromagnetics [91], especially focusing on antenna synthesis [92], [93] and inverse scattering problems [94].

In Figure 6.5, the flowchart for a conventional DE algorithm is outlined. Conceptually speaking, DE optimizes a problem using a population of candidate solutions and creating new candidates by combining the existing ones. The candidate solutions that exhibit the best fitness (i.e. are considered closer to the sought minimum) are then kept.

DE [95] is a metaheuristic, as no assumption is made about the problem being optimized. One of the reasons because a DE algorithm was chosen for the presented application is that DE algorithms treat the optimization problem as a black box and, therefore, are gradient-free. This is an excellent feature because, given the broad variety of parameter sets, a formulation (even numerical) of the gradient of the target function (Equation 6.11) is completely unfeasible.

A shorthand is that, as any metaheuristic, also DE algorithms *do not guarantee that the global minimum is always found*: this heavily depends on the choice of the search space and of the target function. Such choice is, in turn, heavily problem-dependent, so that, for TDR reconstruction, the assumptions on profile models are a matter of utmost importance.

6.4.1 Simple Gaussian profile

Three examples of Gaussian profile reconstruction are hereby presented. The reflectograms produced by such profiles are reported in Figure 6.6(b) and, in this context, represent the available measurement data.

Among the unlimited possibilities, it has been chosen to keep the width and the amplitude of the Gaussian features fixed while moving its position along the line. Therefore, finally, the parameters that have been reconstructed, expressed in the form $[\mu, \sigma, A]$ as in 6.5 are

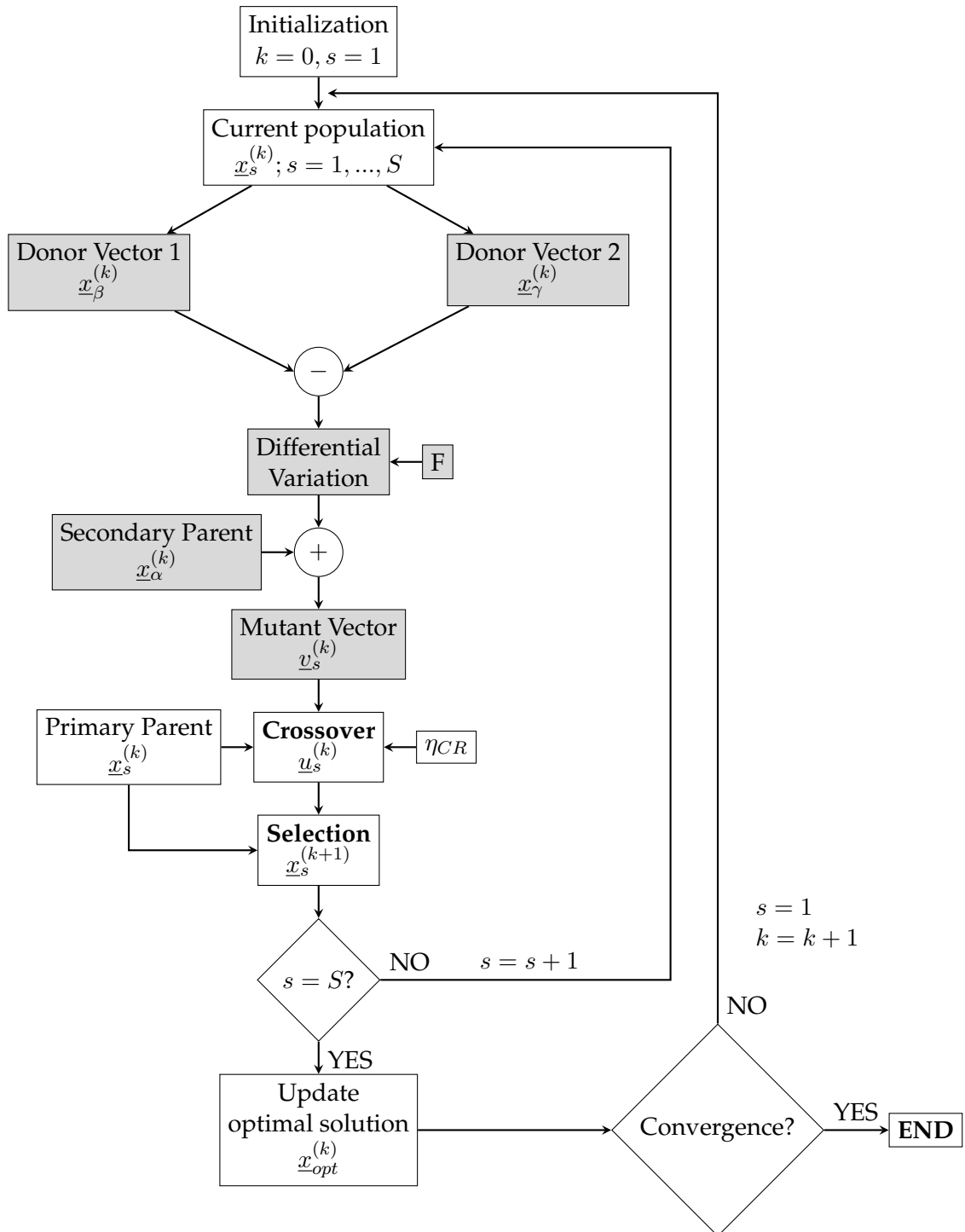
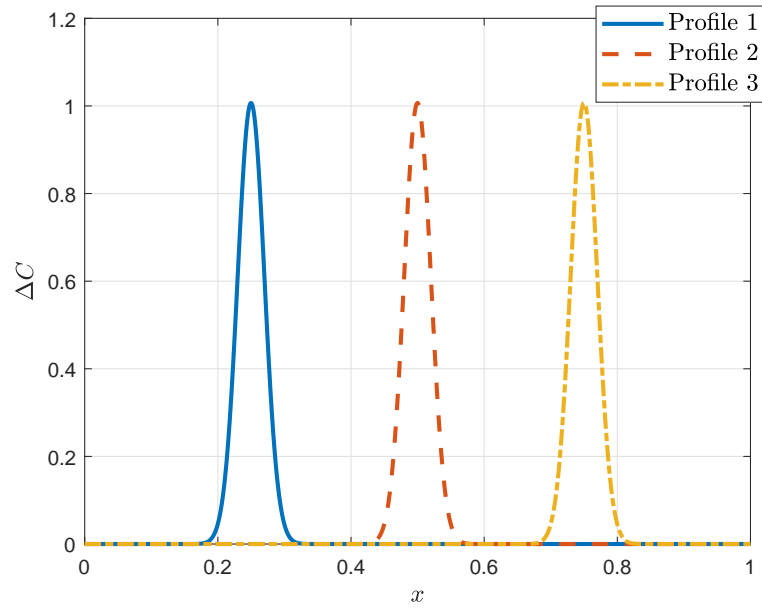
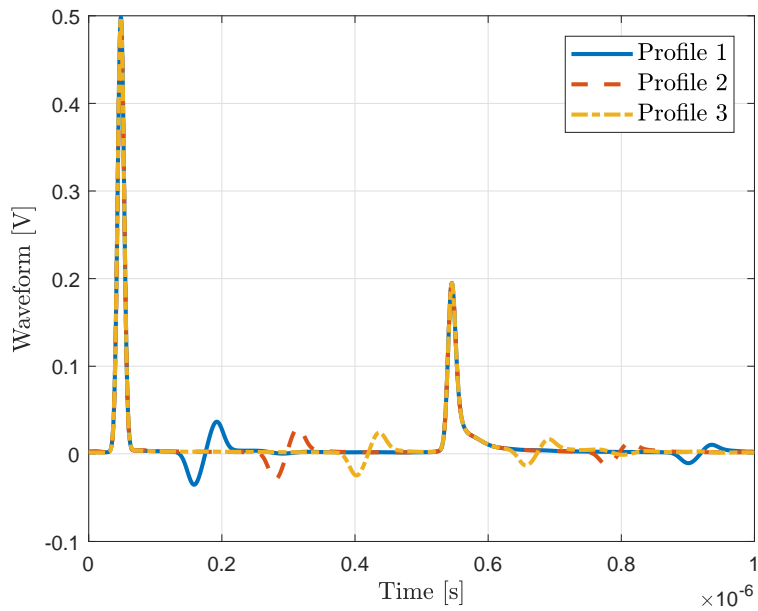


FIGURE 6.5: A conventional Differential Evolution flowchart [91]



(a) Capacitance per unit length profiles



(b) Synthetic measurement data

FIGURE 6.6: Synthetic measurement data for the reconstruction of simple Gaussian profiles: profiles to be reconstructed and simulated TDR measurements

TABLE 6.1: Optimization results for simple Gaussian profile 1

Parameter	True values	Reconstructed	Error [%]
μ_1	0.25	0.2498	0.07
σ_1	0.02	0.0199	0.36
A_1	1	1.0000	0.00

TABLE 6.2: Optimization results for simple Gaussian profile 2

Parameter	True values	Reconstructed	Error [%]
μ_2	0.5000	0.5003	0.06
σ_2	0.0200	0.0202	1.34
A_2	1.0000	1.0000	0.00

Profile 1 [0.25, 0.02, 1]

Profile 2 [0.50, 0.02, 1]

Profile 3 [0.75, 0.02, 1]

Optimization results with the jDE algorithm and search domains for each parameter are summarized in Tables 6.1, 6.2 and 6.3. The percentage errors in the Tables have been computed as in Equation 6.12.

All the optimization problems have been solved 8 times each, so that issues related to stochastic effects could show up, but all runs showed almost identical results. The errors reported in the Tables clearly show that the global minimum has been successfully found within the 5×10^4 computational budget.

Best fitness (target function) values are also plotted in Figure 6.7. Looking at the Figure, it appears obvious that fairly satisfactory results could have been obtained with half the computational budget. This considered, many improvement strategies for the optimization routine could be thought and applied, involving both convergence strategies and target function.

6.4.2 Two overlapping Gaussian profiles

In this Section three examples of reconstruction of capacitance profiles built by summing up Gaussian curves such as those presented in the previous examples are presented. Also in this case, widths and amplitudes have been kept constant while moving the bell-like curves, but here the goal was to bring them closer until they overlapped. This synthetic experiment provides an excellent proof of concept regarding

TABLE 6.3: Optimization results for simple Gaussian profile 2

Parameter	True values	Reconstructed	Error [%]
μ_2	0.7500	0.7501	0.01
σ_2	0.0200	0.0199	0.69
A_2	1.0000	1.0000	0.00

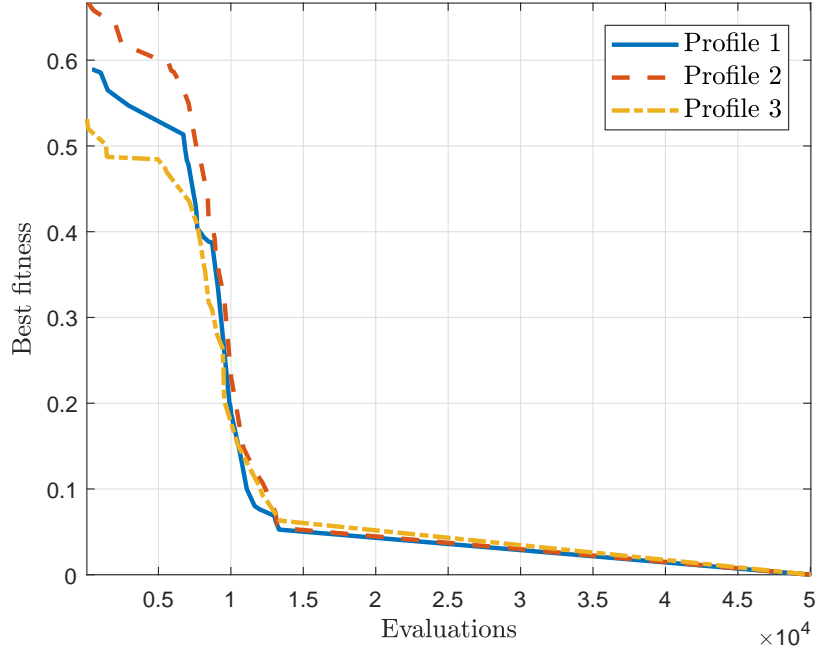


FIGURE 6.7: Best fitness versus number of evaluations in jDE for the reconstruction of the Gaussian profiles of Tables 6.1, 6.2 and 6.3

the capabilities of the proposed approach to the estimation of arbitrary smooth profiles.

The true values of the parameters to be reconstructed, expressed in the form $[\mu_1, \sigma_1, A_1, \mu_2, \sigma_2, A_2]$ as in 6.6, are

Profile 1 $[0.25, 0.02, 1, 0.75, 0.02, 1]$

Profile 2 $[0.25, 0.02, 1, 0.55, 0.02, 1]$

Profile 3 $[0.45, 0.02, 1, 0.55, 0.02, 1]$

Also in this case the reconstruction results are almost perfect, i.e. the global minimum has been successfully found within the 5×10^4 computational budget. It should be noted, however, that in this case it is not true that the computational budget can be significantly decreased while still obtaining satisfactory results.

Otherwise said, the accuracy of the reconstructed profile that can be achieved by lowering the computational budget is poorer. There can be, however, applications for which the accuracy requirements are not so strict.

Finally, in Figure 6.9 some intermediate reconstruction results for the problem presented in 6.6 are reported. It is interesting to notice that, even in this complex situation where the curves overlap significantly, the algorithm has been able to lock on the first peak of the sought profile almost immediately, which may be of utmost importance in many applications (e.g. leakage detection).

TABLE 6.4: Optimization results for two overlapped Gaussian profiles (1)

Parameter	True values	Reconstructed	Error [%]
μ_1	0.25	0.2498	0.09
σ_1	0.02	0.0200	0.17
A_1	1	1.0000	0.00
μ_2	0.75	0.7498	0.03
σ_2	0.02	0.0202	0.96
A_2	1	1.0000	0.00

TABLE 6.5: Optimization results for two overlapped Gaussian profiles (2)

Parameter	True values	Reconstructed	Error [%]
μ_1	0.25	0.2499	0.03
σ_1	0.02	0.0198	0.90
A_1	1	1.0000	0.00
μ_2	0.55	0.5500	0.01
σ_2	0.02	0.0199	0.40
A_2	1	1.0000	0.00

TABLE 6.6: Optimization results for two overlapped Gaussian profiles (3)

Parameter	True values	Reconstructed	Error [%]
μ_1	0.45	0.4505	0.11
σ_1	0.02	0.0198	1.23
A_1	1	1.0000	0.00
μ_2	0.55	0.5494	0.10
σ_2	0.02	0.0196	2.09
A_2	1	1.0000	0.00

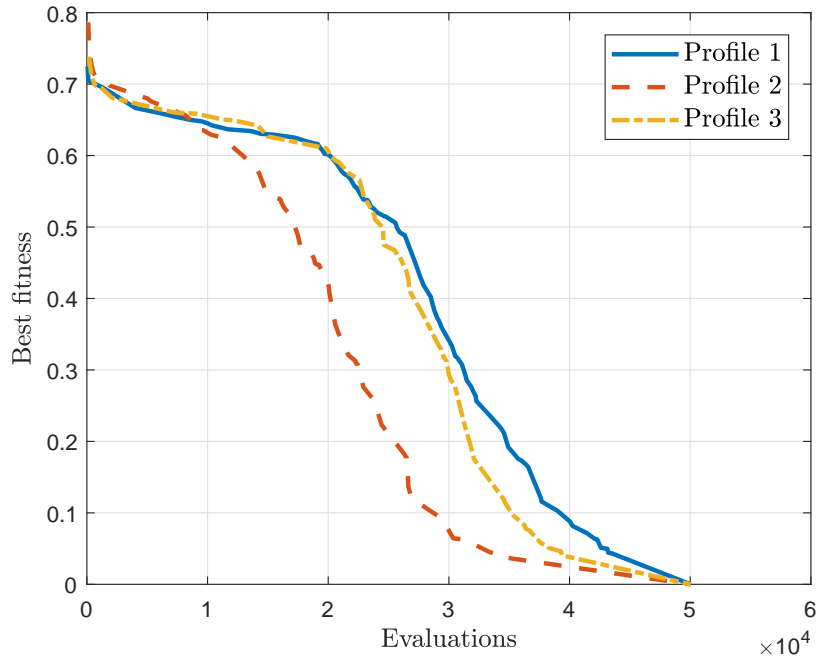


FIGURE 6.8: Best fitness versus number of evaluations in jDE for the reconstruction of the Gaussian profiles of Tables 6.4, 6.5 and 6.6

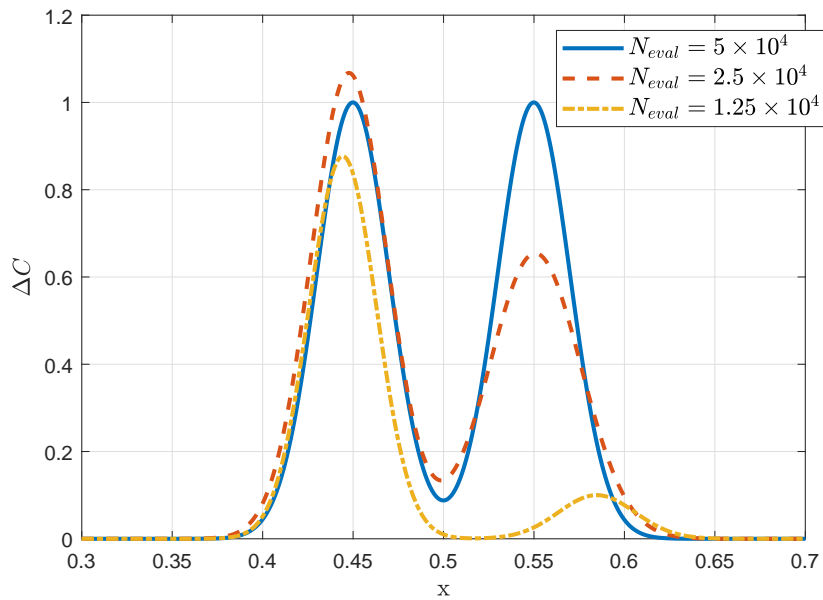


FIGURE 6.9: Intermediate optimization results for the problem outlined in Table 6.6



FIGURE 6.10: Junction between 5 m long RG58-CU coaxial cables

6.5 Experimental results

Actual TDR measurements were performed employing an unconventional TDR setup, as in Figure 5.3(b). This choice has been made to prove that the proposed TDR inversion method is robust and sound even in presence of non standard measurement models. All the case studies hereby presented are related to the estimation of capacitance profiles with one or more faults. More specifically, the exact model for the chosen measurement setup is that in Figure 5.1 if the “Connectors 2” network is neglected.

Six 5 m long RG58-CU male BNC terminated coaxial cables were connected together with BNC T-connectors (two female and one male termination), as shown in Figure 6.10. Following the modeling approach discussed in the previous Chapters and using the cross section data from the cable manufacturer (cf. Figure 4.7 and [96]), the line model under resting conditions was built and the resulting simulated reflectogram is shown in Figure 6.12 compared with actual measurements. The error figure computed in resting conditions is $e_0 = 0.27$.

T-connectors have been chosen for cable junctions so that capacitive faults made with BNC to banana adapters, as in Figure 6.11, could be easily introduced and removed. The banana terminations allowed, in fact, to introducing the 10 pF capacitor that would increase the amplitude of the capacitive fault in the reflectograms. Moreover, approximate measurements of the total capacitance of the “fault devices” (Figure 6.11) have been performed using an Escort ELC-3131D LCR meter, obtaining:

- F1 device: 3.4 ± 0.5 pF
- F2 device: 14.3 ± 0.6 pF

These measurements allow evaluating the accuracy of the proposed inversion method not only to pinpoint the location of faults and their shape, but also to evaluate their amplitude, i.e. to estimate the exact value of capacitance per unit length along the TDR probe.

The dataset has been built by moving the F2 device between the five junctions, from the closest one to the measurement port to the farthest. As shown in Figure 6.13, the jDE algorithm has converged for each case study in the dataset. Basically



FIGURE 6.11: “F1” (left) and “F2” (right) capacitive fault devices

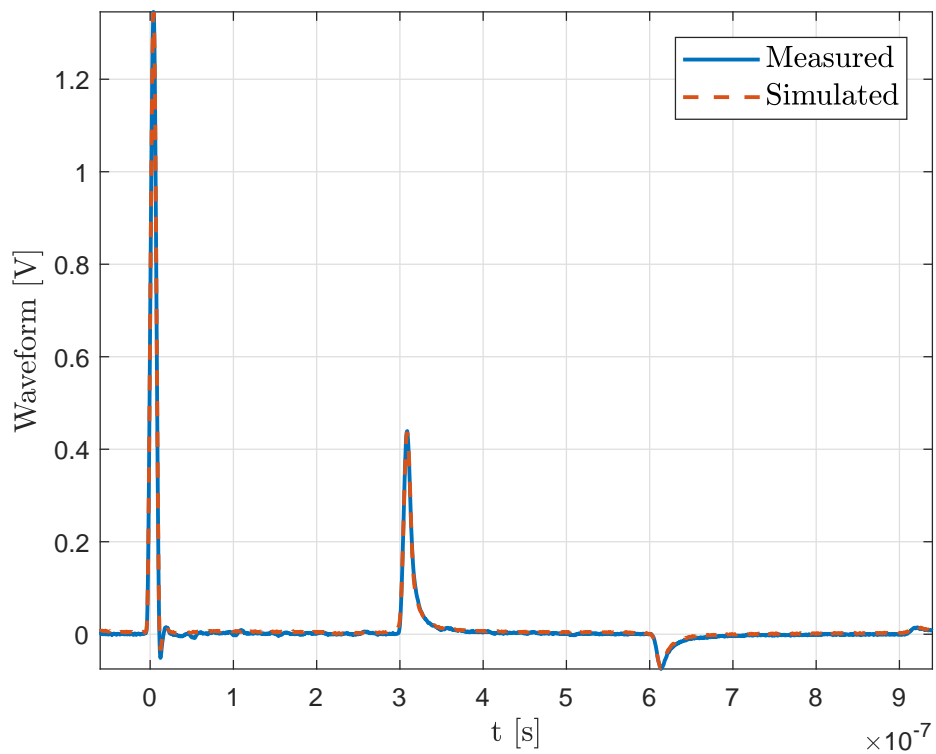


FIGURE 6.12: Measured and reconstructed reflectogram on the 30 m long coaxial line without faults

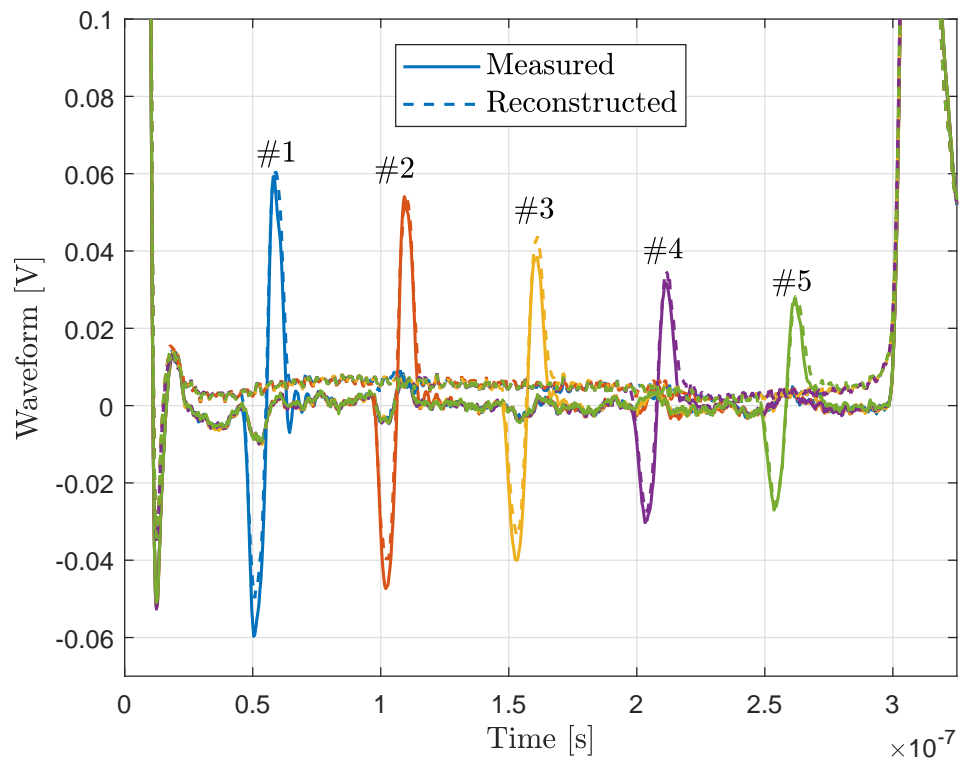


FIGURE 6.13: Measured versus reconstructed TDR waveforms for the first dataset, detail on relevant reflectogram features

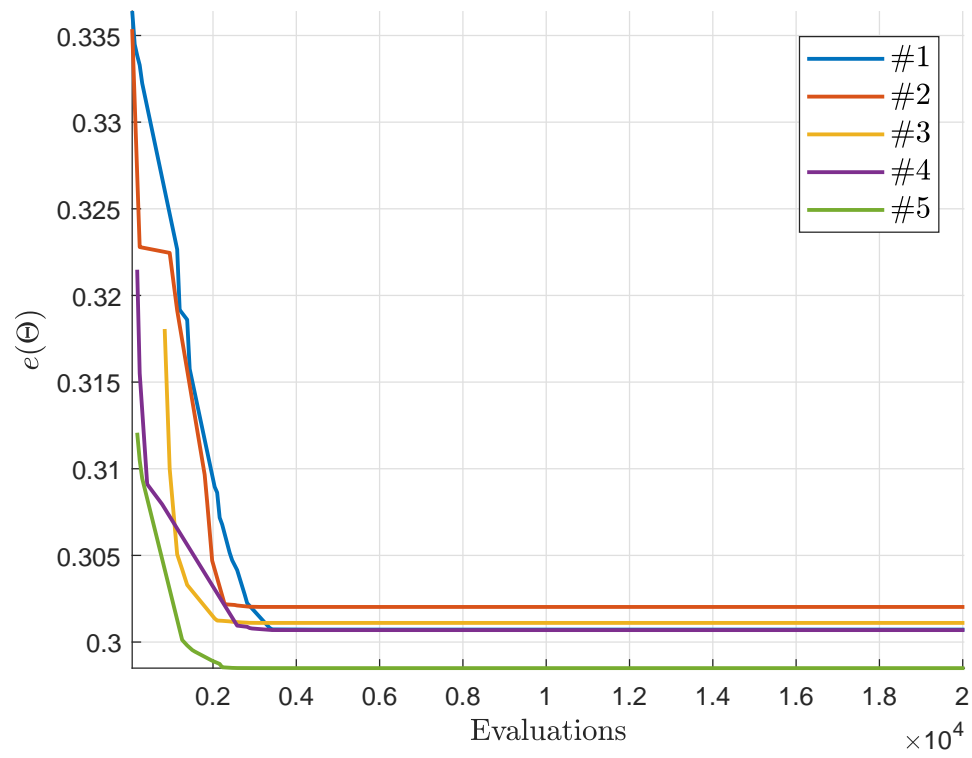


FIGURE 6.14: Target function values for the first dataset

convergence has been reached immediately after ~ 2000 evaluations of the target function (Figure 6.14) for every case study, i.e. after less than 5 minutes, considering that the algorithm has been execution on four threads with a 2nd generation Intel i7 mobile CPU.

More advanced studies are in progress, involving reflectograms taken on the same line with two faults, obtained with different positions of F1 and F2 devices.

Chapter 7

Conclusions and future work

You never change things by fighting the existing reality. To change something, build a new model that makes the existing model obsolete

RICHARD BUCKMINSTER FULLER

In this thesis a full featured workflow for the implementation of integrated TDR-based diagnosis and monitoring systems has been proposed.

First, the usage of TDR probes with other measurement techniques than TDR, i.e. capacimetry and Time-of-Flight, has been introduced as a continuous, real-time monitoring technique. This way, simple alerts in case of anomalies would trigger further, more specific analyses based on reflectometry.

Then, the TDR technique has been thoroughly examined and discussed with specific regard to distributed sensing applications, i.e. where some parameter must be profiled along an elongated Sensing Element. The simplest approach to TDR processing, based on direct reflectogram analysis, has been presented with newly introduced, automated signal processing techniques. This approach can safely be applied in some simple, controlled scenarios, where the direct analysis of features on reflectograms gives enough information about the parameter under test.

In the core part of this thesis, the TDR inverse problem is dealt with. A custom, reflectometry oriented frequency and time domain Transmission Line simulator has been presented as simulation tool, and the jDE optimization algorithm has been successfully applied to solve the inverse problem in both synthetic and real life scenarios. It is true indeed that optimization algorithms can be exceptionally computationally demanding; therefore, the proposed approach is best suited to be implemented in a modern cloud-based architecture, in which the TDR unit on the field is an IoT-enabled device that performs measurements and gathers data to be processed in the cloud. The problem of measurement system calibration has been discussed as well. Generic TDR setups have been modeled and the effects of cables and transitions has been taken into account by means of the well-established theoretical foundations of network theory.

The outcomes of the proposed processing techniques are in each case satisfactory and pave the way towards the implementation of integrated TDR-based measurement setups for a broad range of applications. More specifically, the advanced calibration techniques proposed in this thesis enable characterizing non conventional

TDR units based on simple electronics (e.g. fast logic gates and high-performance digitizers), thus resulting in low-cost TDR measurement systems. Besides, the results of this thesis may be straightforwardly used to implement a custom made device with many practical advantages, e.g.:

- Permanent installation on the field
- Implementation of advanced network features for client-server measurement system architectures
- Complete characterization for accurate reflectogram post processing
- On-board integration of other measurement techniques (e.g. capacimetry) and direct reflectogram processing for real-time monitoring purposes.

Appendix A

MATLAB implementations of the simulation algorithm

A.1 Foreword

In this Appendix the MATLAB code with which the presented simulation algorithms have been implemented is provided. A brief discussion introduces every Section, and comments are also introduced in the codebase.

As general caveat, since the development of the presented software is still in progress, this Appendix is intended to be illustrative and non-exhaustive. Up to date code, documentation and notes can be found on the Git repository of the LineLab project [60].

A.2 Line builder module

This module prepares the Transmission Line model for the simulator. Here multiple lines can be concatenated and the profiles of the primary parameters are defined.

In the code below a line made by a bi-wire and a coaxial cable is modeled. In the example, the coax has a smooth rectangle shaped resistive fault centered at 25% of its length, while the other profiles are disabled. Please note that, if the `'shape'` field is set to `'disabled'`, any other profile parameters will be ignored.

Further information about how to define line and profile properties will be given in the next Sections.

```
%% Init
clear, close all
clc

% File path and name for line model
savefile = './line_models/line.mat';

%% Define the model and save it
% Define any number of chained lines and put them in the
  line_model cell
% array
rg58 = struct( ...
```

```

'linemodel', 'coax', 'ri', 0.255e-3, 'ro', 0.76e-3, 't', 0.27
    e-3, 'l', 100, ... % Line model and geometry
'epsilon_r', 2.26, 'esrtoggle', true, 'tan_d', 0.00031, '
    debyetoggle', false, ... % Dielectric properties
'sigma', 5.96e7, 'skintoggle', true, ... % Conductor
    properties
'Lprofile', struct('shape', 'disabled'), ...
'Rprofile', struct('shape', 'gauss_rect', 'position', 0.5, '
    width', 0.2, 'amplitude', 3, 'rise', 0.01), ...
'Gprofile', struct('shape', 'disabled'), ...
'Cprofile', struct('shape', 'disabled', 'position', 0.25, '
    width', 0.02, 'amplitude', 100e-12) ...
);

biwire = struct( ...
'linemodel', 'biwire', 'd', 1e-3, 'D', 2e-3, 'l', 10, ... %
    Line model and geometry
'epsilon_r', 2.1, 'esrtoggle', true, 'tan_d', 0.002, '
    debyetoggle', false, ... % Dielectric properties
'sigma', 5.96e7, 'skintoggle', true, 'sigma_d', 1e-15, ... %
    Conductor properties
'Lprofile', struct('shape', 'disabled'), ...
'Rprofile', struct('shape', 'disabled', 'position', 0.5, '
    width', 0.2, 'amplitude', 1, 'rise', 0.01), ...
'Gprofile', struct('shape', 'disabled'), ...
'Cprofile', struct('shape', 'disabled', 'position', 0.5, '
    amplitude', 1000e-12, 'width', 0.1) ...
);

line_model = {rg58, biwire};

save(savefile, 'line_model')

```

A.3 LineLab frequency domain simulation module

This code computes the frequency response of the line modeled as described in the previous Section. Many subroutines are called here that will be presented later. LineLab is optimized for parallel computing, therefore if any `parpool` is available, frequency domain simulations are executed in a `parfor` loop. In its current version, LineLab checks the availability of a `parpool` and, if none available, performs simulations of a single thread.

This module can also compute typical frequency domain parameters such as the VSWR, the S_{11} scattering parameter, and the group delay, that are quite common in VNA practice. In the code hereby provided, the `plot_s11` flag chooses whether to plot S_{11} at the end of the simulation.

The program can also plot the profiles of the primary parameters if needed. In that case, the `plot_profiles` flag must be set to true.

```
%% Init
clear, close all
clc

tic % Start execution timer

savefile = './lines/line.mat'; % File path and name for
    simulated line

disp('LineLab >> Frequency domain simulation module')
addpath('./lib')

% Figures
plot_profiles = false;
plot_s11 = false; Z0 = 50;
tdr_toggle = true;

% Stimulus file
% If calibration data are available, they must be provided
    here as:
% - Zsource, omega_s: generator impedance
% - Zmeas, omega_m: measurement port impedance
%stimulus_file = './measurements/tek/agilent_no_load_cal.mat
    ';
stimulus_file = 'no_signal';
%cal_data = load(stimulus_file);
cal_data = struct();

% Line model
line_model_file = './line_models/rg58cu_50m.mat';

%frequency_mode = 'signal';
frequency_mode = 'custom';

% Measurement node, intended as the interface between
    subsequent lines
% E.g.:
% 0 -> at the beginning of the first line
% 1 -> between line 0 and 1
% 2 -> between line 1 and 2
measurement_port = 0;

% Used in custom frequency mode
```

```

t_max = 50.00e-7;
Nh = 1999;
%t_max = 10*20*Nh/1000/200e6;

%% Source, measurement port and load parameters
% Source impedance
if isfield(cal_data, 'Zsource')
Zsource = @(w) interp1(cal_data.omega_s, cal_data.Zsource, w)
;
else
Zsource = @(w) 50 + 1i*w*0;
end
% Measurement port impedance
if isfield(cal_data, 'Zmeas')
Zmeas = @(w) interp1(cal_data.omega_m, cal_data.Zmeas, w);
else
Zmeas = @(w) 1e9 ./ (1 + 1i*w*0e-12*1e9);
end
% Load impedance
if isfield(cal_data, 'Zload')
Zload = @(w) interp1(cal_data.omega_l, cal_data.Zload, w);
else
Zload = @(w) 50 ./ (1 + 1i*w*0e-12*1e9);
end

%% Basic line parameters

load(line_model_file)

if isfield(cal_data, 'connectors')
network_topology = [cal_data.connectors, line_model];
else
network_topology = line_model;
end

% Primary parameters and maximum propagation velocity
[L0_line , R0_line, C0_line, G0_line, l] =
    TLprimaryParameters(network_topology);
v_line = max(sqrt(1 ./ (L0_line .* C0_line)));

%% Simulation parameters
% Also check TLfrequencySpan documentation)
sim_params = struct( ...
'freqmode', frequency_mode,...
'stimulusfile', stimulus_file,...

```

```

'v_line', v_line, ...
'l', sum(l), ...
'tmax', t_max, ...
'Nh', Nh ...
);

%% Simulation parameters
freq_params = TLfrequencySpan(sim_params);

% Array length check
if freq_params.Nx >= 30e3
array_check = questdlg(sprintf('LineLab >> Current settings
    require the simulation of %d cells. Continue anyway?',
    freq_params.Nx), 'LineLab long array');
if ~strcmp(array_check, 'Yes')
disp('LineLab >> Simulation aborted');
return
end
end

%% Profiling parameters

disp('LineLab >> Computing custom profiles for primary
    parameters')

% Extracting relevant quantities from freqParams struct
Nh = freq_params.Nh;
Nx = freq_params.Nx;
dx = freq_params.dx;
omega = freq_params.omega;

% Computing parameter profiles
Nxi = round(Nx*l/sum(l));
% FIXME find a cleaner solution to ensure sum(Nxi) = Nx
if sum(Nxi) - Nx ~= 0
Nxi(1) = Nxi(1) - (sum(Nxi) - Nx);
end

L_line = zeros(1,Nx);
C_line = zeros(1,Nx);
R_line = zeros(1,Nx);
G_line = zeros(1,Nx);
for i = 1:length(Nxi)
if i == 1
istart = 1;

```

```

else
istart = Nxi(i-1)+1;
end

L_line(istart:istart+Nxi(i)-1) = L0_line(i) +
    TLcomposeProfile(Nxi(i), network_topology{i}.Lprofile);
R_line(istart:istart+Nxi(i)-1) = R0_line(i) +
    TLcomposeProfile(Nxi(i), network_topology{i}.Rprofile);
C_line(istart:istart+Nxi(i)-1) = C0_line(i) +
    TLcomposeProfile(Nxi(i), network_topology{i}.Cprofile);
G_line(istart:istart+Nxi(i)-1) = G0_line(i) +
    TLcomposeProfile(Nxi(i), network_topology{i}.Gprofile);
end

%% Solution (numeric)
% Performing frequency domain simulations
stopwatch = toc;

if measurement_port == 0
measurement_node = 1;
else
measurement_node = round(sum(1(1:measurement_port)) / sum(1)
    * Nx);
end

VrefH = zeros(Nh, 1);
if(isempty(gcf('nocreate')))
disp('LineLab >> Performing frequency domain simulations (
    single thread)')
for kw = 1:Nh
% Source, measurement and load impedances
YS_w = 1/Zsource(omega(kw)); Ymeas_w = 1/Zmeas(omega(kw));
    Yload_w = 1/Zload(omega(kw));
% Series dispersion
YL = TLskinEffect(Nxi, network_topology, omega(kw), R_line,
    L_line) / dx;
% Parallel dispersion
YC = TLepsilonDispersion(Nxi, network_topology, omega(kw),
    G_line, C_line) * dx;
VrefH(kw) = TlsolveCircuit(YS_w, Ymeas_w, YL, YC, Yload_w,
    measurement_node);
end
else
disp('LineLab >> Performing frequency domain simulations (
    multi thread)')

```

```

parfor kw = 1:Nh
% Source, measurement and load impedances
YS_w = 1/Zsource(omega(kw)); Ymeas_w = 1/Zmeas(omega(kw));
    Yload_w = 1/Zload(omega(kw));
% Series dispersion
YL = TLskinEffect(Nxi, network_topology, omega(kw), R_line,
    L_line) / dx;
% Parallel dispersion
YC = TLepsilonDispersion(Nxi, network_topology, omega(kw),
    G_line, C_line) * dx;
VrefH(kw) = TlsolveCircuit(YS_w, Ymeas_w, YL, YC, Yload_w,
    measurement_node);
end
end

% DC response
% FIXME causes a lot of trouble: deprecate?
if sum(R_line) ~= 0 || sum(G_line) ~= 0
VrefH0 = TlsolveCircuit(1/Zsource(0), 1/Zmeas(0), 1./R_line,
    G_line, 1/Zload(0), measurement_node);
else
if isinf(Zload(0))
VrefH0 = 1;
else
VrefH0 = Zload(0) / (Zload(0) + Zsource(0));
end
end

% Merging DC and AC responses
freq_params.omega = [0; freq_params.omega]; VrefH = [VrefH0;
    VrefH];

fprintf('LineLab >> Simulation completed in %f s\n', toc -
    stopwatch)

%% Save data
disp('LineLab >> Saving simulation data on disk')

% Variables to be saved
vars = {'sim_params', 'network_topology', 'freq_params', ...
    'Zload', 'Zsource', 'Zmeas', 'VrefH'};
save(savefile, vars{:})

stopwatch = toc;

```

```

fprintf('LineLab >> Simulation completed. Total time elapsed:
      %d min %d sec\n', ...
floor(stopwatch/60), round(mod(stopwatch, 60)))

%% Performing additional operations

% TODO all these quantities basically depend on just VrefH
  and omega. They might be computed by a single function, e.
  g. TLpostProcess(omega, VrefH, quantity)

% S11
IrefH = (1 - VrefH) ./ Zsource([0; omega]);
a = 0.5*(VrefH + Z0*IrefH) / sqrt(real(Z0));
b = 0.5*(VrefH - Z0*IrefH) / sqrt(real(Z0));

S11 = b ./ a;

% Voltage Standing Wave Ratio
VSWR = (1+abs(S11)) ./ (1-abs(S11));

% Group delay
tg = - diff(unwrap(angle(S11))) ./ diff(freq_params.omega);

%% Plotting useful variables

% RLCG profiles
if plot_profiles
hProfiles = TLplotProfiles(R_line, L_line, C_line, G_line, 1)
;
end

% S11
if plot_s11
hS11 = TLplotComplex(freq_params.omega, S11, 'plotmode', 'mag
  ', 'fontsize', 12);
end

%% Close program
rmpath('./lib')

if tdr_toggle
TLtdrsim
end

```

A.4 LineLab time domain simulation module

In this Section the code that actually produces simulated TDR waveforms is presented. It loads the results produced by the frequency domain simulation module (in particular the line response V_h) and applies them to any (synthetic or measured) stimulus signal.

```
%% Init
clear, clc

disp('LineLab >> Time Domain simulation module')
addpath('./lib')

%% Setting up filenames and loading needed data
line_file = './lines/line.mat';
measurement_file = './measurements/tek/agilent_50m.mat';

disp('LineLab >> Loading simulated line parameters')
load(line_file)

%% Set stimulus signal
% This cell may be used to override the default stimulus
% provided by the
% datafile containing the line response. Uncomment ONLY the
% desired mode

%stimulusMode = 'datafile'; % Default stimulus or
% synthStimulus if none provided in the line file
stimulusMode = 'synthetic'; % Synthetic stimulus with
% parameters given in the synthStimulus struct
%stimulusMode = 'measured'; % Overrides the default stimulus
% with another measured signal loaded from the
% stimulusOverride path

% Check a list of available signal shapes in the help of
% TLsourceSignal
% Delay and width factors are referred to the whole
% simulation time
synthStimulus = struct('shape', 'gauss_pulse', ...
'delayfactor', 0.1, 'widthfactor', 0.01, ...
'amplitude', 1);

%% Signal loading or synthesis
disp('LineLab >> Configuring stimulus signal')

switch stimulusMode
```

```

case 'datafile'
wave = load(sim_params.stimulusfile);
tsig = wave.t;
Vs = wave.v;

case 'synthetic'
tsig = freq_params.t; tsig = tsig - tsig(1);

% Extracting relevant line parameters
% TODO adapt to multiline
line_velocity = sim_params.v_line;
line_length = 0;
for i = 1:length(network_topology)
line_length = line_length + network_topology{i}.l;
end
t_expected = 2*line_length/line_velocity;

Vs = TLsourceSignal(synthStimulus.shape, tsig, ...
synthStimulus.delayfactor * t_expected, synthStimulus.
widthfactor * t_expected, ...
synthStimulus.amplitude);
case 'measured'
wave = load(sim_params.stimulusfile);
tsig = wave.t;
Vs = wave.v;

otherwise
error('LineLab - TDR simulation module: invalid stimulus mode
')
end

%% Time domain response computation (FFT)
disp('LineLab >> Computing TDR response')
% TODO implement Fourier analysis consistency validation

% Avoiding odd number of samples
if mod(length(tsig), 2)
tsig = tsig(1:end-1);
Vs = Vs(1:end-1);
end

f = freq_params.omega/(2*pi);
f_max = freq_params.fmax;

if length(tsig) ~= 2*(freq_params.Nh+1)

```

```

% Resampling needed
df_required = 1/range(tsig);
Nh_required = round(f_max / df_required);
f_required = df_required*(1:Nh_required)';

Nt_required = 2*(Nh_required + 1);
t_ = linspace(0, tsig(end), Nt_required); dt = mean(diff(t_))
    ; % Time array and dt
Vs = interp1(tsig, Vs, t_); Vs = Vs';

VrefH = interp1(f, VrefH, f_required, 'spline');
else
Nt = 2*(freq_params.Nh+1);
end

Vs = reshape(Vs, [length(Vs), 1]);

Vs_fft = fft(Vs)/Nt;

H = [VrefH; 0; conj(VrefH(end:-1:2))];
xRef_fft = H .* Vs_fft;
xRef = ifft(xRef_fft)*Nt;

%% Plot time domain response
meas_file = load(measurement_file);
vmeas = meas_file.v;
hTDR = TLplotTDR(tsig, xRef, 'fontsize', 12, 'linewidth', 2,
    'xlim', [0, 0.8e-6]);

%% Ending program

rmpath('./lib')
disp('LineLab >> Time domain simulation completed')

```

A.5 Subroutines and other utilities

At last, code for secondary functions are provided. Such routines are called by the core modules of LineLab and provide many features, ranging from optimal frequency range computation to profile parameter parsing.

On a side note, probably the most important subroutine is also hereby presented, i.e. the fast tridiagonal solver (see Section 4.6.2), that is an efficient implementation of the Thomas algorithm for tridiagonal systems where not every unknown must be computed.

In its current state, the documentation of each function is still incomplete or missing, therefore some simple comments will be given where needed.

A.5.1 Base values for the primary parameters

This function computes the base values for line primary parameters using geometry data provided by the line builder module. Currently only coaxial and bi-wire models are available, however the implementation of custom models is as straightforward as adding another 'case' to the function.

```
function [L0_line , R0_line, C0_line, G0_line, l] =
    TLprimaryParameters(par)
%TLPRIMARYPARAMETERS Computes basic primary parameters for
some simple line models
% Each different line model requires a different set of
parameters, which
% must be provided in the PAR struct. In detail:
%
% - 'coax' line requires
%     - 'l' total length of the line [m]
%     - 'ro' outer conductor radius [m]
%     - 'ri' inner conductor radius [m]
%     - 't' outer conductor thickness [m]
%     - 'epsilon_r' relative dielectric permittivity of the
inner material
%
% - 'biwire' line is WIP
%     - 'l' total length of the line [m]
%     - 'd' diameter of wires [m]
%     - 'D' distance between centers [m]
%     - 'epsilon_r' effective dielectric permittivity of
the surrounding material

epsilon0 = 8.854187817e-12; % Vacuum dielectric permittivity
mu0 = 4*pi*1e-7; % Vacuum magnetic permeability

disp('LineLab >> Computing primary line parameters')

C0_line = zeros(size(par));
L0_line = zeros(size(par));
R0_line = zeros(size(par));
G0_line = zeros(size(par));
l = zeros(size(par));
for i = 1:length(par)
    the_line = par{i};
    switch the_line.linemodel
        case 'coax'
            % Extracting parameters
            sigma = the_line.sigma; % Copper
            conductance
```

```

    ro = the_line.ro;
    ri = the_line.ri;
    t = the_line.t;
    epsilon_r = the_line.epsilon_r;

    C0_line(i) = 2*pi*epsilon0*epsilon_r
        / log(ro/ri); % Distributed
        capacitance [F/m]
    L0_line(i) = mu0/(2*pi) * log(ro/ri);
        % Distributed inductance [H/m]
    R0_line(i) = 1/(pi*ri^2*sigma) + 1/(
        pi*sigma)/((ro + t)^2 - ro^2); %
        Distributed resistance [ohm/m]
    G0_line(i) = 0; % Distributed
        conductance [S/m]

case 'biwire'
    % Extracting parameters
    d = the_line.d;
    D = the_line.D;
    epsilon_r = the_line.epsilon_r;
    sigma_d = the_line.sigma_d;

    C0_line(i) = pi*epsilon0*epsilon_r /
        acosh(D/d); % Distributed
        capacitance [F/m]
    G0_line(i) = pi*sigma_d / acosh(D/d);
        % Distributed conductance [S/m]
    R0_line(i) = 2 / (pi * (d/2)^2 *
        sigma); % Distributed resistance [
        ohm/m]
    L0_line(i) = mu0 / pi * (1/4 + acosh(
        D/d)); % Distributed inductance [H
        /m]

otherwise
    error('Unknown line model ''%s'',
        linemodel)
end
l(i) = the_line.l;

end
end

```

TABLE A.1: Available profile shapes

Shape	Parameters
'disabled'	N/A
'point'	'position', 'amplitude'
'step'	'position', 'amplitude'
'rect'	'position', 'amplitude', 'width'
'gauss_pulse'	'position', 'amplitude', 'width'
'gauss_rect'	'position', 'amplitude', 'width', 'rise'
'gauss_step'	'position', 'amplitude', 'rise'

A.5.2 Primary parameter profile composition

The composition of the profiles is designed to be the most intuitive possible. Each profile is defined by means of a `struct` that contains all needed parameters. Exception made for the `'poly_fourier'` shape, profiles are always described as superimposed individual features, so that virtually any shape can be defined while keeping the technique essentially application-oriented. Therefore, the numeric parameters in the `struct` are arrays whose length represents the number of features to be summed up (e.g. three Gaussian steps as in the case of layered materials need a parameter set made of arrays containing three elements).

Currently available shapes are enumerated in Table A.1. Geometric parameters are always expressed relatively to the length of the line, i.e. their range is always $[0, 1]$.

The `'poly_fourier'` shape behaves in a slightly different way, as it only requires a `'coefficients'` array. The first coefficient is the offset component and the others are respectively cosine (a_i) and sine (b_i) amplitudes, as in the following equation:

$$C(x) = c_0 + \sum_{i=1}^N [a_i \cos(2\pi i x) + b_i \sin(2\pi i x)], x \in [0, 1] \quad (\text{A.1})$$

```
function xp = TLcomposeProfile(Nx, params)
%TLCOMPOSEPROFILE Generates a custom profile for any line
% parameter X
% TLcomposeProfile mainly requires the number Nx of samples
% to be
% computed and a struct with other parameters. Other
% required parameters
% depend on the chosen shape and are provided along with it
% in the struct.
%
% Please note that almost any shape can be cumulated, i.e.
% a profile may
% be obtained that is sum of suitably scaled and shifted
% profiles having
```

```

% the same shape (e.g. the interfaces between three
% different dielectrics
% can be defined by summing up two step or gauss_step
% profiles).
% This feature is accessed by defining arrays of parameters
% in the params
% struct
%
% - 'poly_real':  $X(i) = kf(n+1)*i^n + kf(n)*i^{(n-1)} + \dots$ 
%                $kf(2)*i +$ 
%                $kf(1)$ , with  $1 \leq i \leq Nx$ 
% - TODO implement 'poly_trig' for trigonometric
%   polynomials

% Converting relative parameters to indices
xp = zeros(Nx,1);
switch params.shape
    case 'point'
        for i = 1:length(params.position)
            xp(max([round(params.position(i) * Nx), 1]))
                = params.amplitude(i);
        end

    case 'step'
        for i = 1:length(params.position)
            kfi = max([round(params.position(i) * Nx),
                1]);
            xp(kfi:end) = xp(kfi:end) + params.amplitude(
                i);
        end

    case 'rect'
        for i = 1:length(params.position)
            wfi = max([round(params.width(i) * Nx), 1]);
            kfi = max([round(params.position(i) * Nx),
                1]);
            xp(kfi - round(wfi/2):kfi + round(wfi/2)) =
                ...
            xp(kfi - round(wfi/2):kfi + round(wfi/2))+
                params.amplitude(i);
        end

    case 'gauss_pulse'
        for i = 1:length(params.position)
            wfi = max([round(params.width(i) * Nx), 1]);

```

```

        kfi = max([round(params.position(i) * Nx),
            1]);
        xfi = params.amplitude(i);
        xp = xp + xfi * normpdf((1:Nx)', kfi, wfi) ./
            normpdf(kfi, kfi, wfi);
    end

    case 'gauss_rect'
    for i = 1:length(params.position)
        wfi = max([round(params.width(i) * Nx), 1]);
        kfi = max([round(params.position(i) * Nx),
            1]);
        rfi = max([round(params.rise(i) * Nx), 1]);
        xfi = params.amplitude(i);
        xp = xp + xfi * (normcdf((1:Nx)', kfi - round
            (wfi/2), rfi) - ...
            normcdf((1:Nx)', kfi + round(wfi/2), rfi));
    end

    case 'gauss_step'
    for i = 1:length(params.position)
        kfi = max([round(params.position(i) * Nx),
            1]);
        rfi = max([round(params.rise(i) * Nx), 1]);
        xfi = params.amplitude(i);
        xp = xp + xfi * normcdf((1:Nx)', kfi, rfi);
    end

    case 'poly_fourier'
    coeff = params.coefficients;
    xp = coeff(1)*ones(Nx,1);
    for i = 2:2:length(coeff)
        xp = xp + coeff(i)*cos(2*pi/Nx*(i/2)*(1:Nx)')
            + ...
            coeff(i+1)*sin(2*pi/Nx*(i/2)*(1:Nx)');
    end

    case 'disabled'

    otherwise
    warning('TLcomposeProfile >> Unsupported profile shape '%s''
        ', shape)

    end
end

```

```
end
```

A.5.3 Transverse impedance

This subroutine computes the complex transverse line impedance profile at frequency ω applying the effects defined in the line builder module.

```
function YC = TLepsilonDispersion(Nxi, line_parameters, omega
    , G_line, C_line)
%TLEPSILONDISPERSION Summary of this function goes here
%  TODO only ESR currently implemented

C = zeros(size(C_line));
G = zeros(size(G_line));
for i = 1:length(Nxi)
    if i == 1
        istart = 1;
    else
        istart = Nxi(i-1)+1;
    end

    % Debye model
    if line_parameters{i}.debyetoggle
        % TODO not yet implemented
    else
        % ESR (tan_delta)
        if line_parameters{i}.esrtoggle
            tan_d = line_parameters{i}.tan_d;
            G(istart:istart+Nxi(i)-1) = tan_d*
                omega*C_line(istart:istart+Nxi(i)
                    -1) + G_line(istart:istart+Nxi(i)
                        -1);
            C(istart:istart+Nxi(i)-1) = C_line(
                istart:istart+Nxi(i)-1);
        % No dispersion
        else
            C(istart:istart+Nxi(i)-1) = C_line(
                istart:istart+Nxi(i)-1);
            G(istart:istart+Nxi(i)-1) = G_line(
                istart:istart+Nxi(i)-1);
        end
    end
end

end

YC = 1i*omega*C + G;
```

```
end
```

A.5.4 Longitudinal impedance

This subroutine computes the complex longitudinal line impedance profile at frequency ω applying the effects defined in the line builder module (e.g. the skin effect).

```
function YL = TLskinEffect(Nxi, line_parameters, omega,
    R_line, L_line)
%TLSKINEFFECT Summary of this function goes here
% Detailed explanation goes here

sigma_copper = 5.96e7; % Copper conductance
mu0 = 4*pi*1e-7; % Magnetic permeability

R = zeros(size(R_line));
L = zeros(size(L_line));
for i = 1:length(Nxi)
    if i == 1
        istart = 1;
    else
        istart = Nxi(i-1)+1;
    end

    switch line_parameters{i}.linemodel
        % Coaxial line
        case 'coax'
            if line_parameters{i}.skintoggle
                ri = line_parameters{i}.ri;
                ro = line_parameters{i}.ro
                ;
                Rsheet = sqrt(omega*mu0/(2*
                    sigma_copper));
                R(istart:istart+Nxi(i)-1) =
                    Rsheet*(1/ri + 1/ro)/(2*pi
                    ) + R_line(istart:istart+
                    Nxi(i)-1);
                % TODO implement inductive
                faults
                L(istart:istart+Nxi(i)-1) = (
                    mu0/2/pi*log(ro/ri) +
                    Rsheet / (2*pi*omega)*(1/
                    ri + 1/ro))*ones(size(
                    L_line(istart:istart+Nxi(i)
                    )-1));
```

```

        else
            R(istart:istart+Nxi(i)-1) =
                R_line(istart:istart+Nxi(i)
                    )-1);
            L(istart:istart+Nxi(i)-1) =
                L_line(istart:istart+Nxi(i)
                    )-1);
        end

    case 'biwire'
        if line_parameters{i}.skintoggle
            d = line_parameters{i}.d;
            Rsheet = sqrt(omega*mu0/(2*
                sigma_copper));
            R(istart:istart+Nxi(i)-1) =
                2*Rsheet/(pi*d) + R_line(
                    istart:istart+Nxi(i)-1);
            L(istart:istart+Nxi(i)-1) =
                L_line(istart:istart+Nxi(i)
                    )-1);
        else
            R(istart:istart+Nxi(i)-1) =
                R_line(istart:istart+Nxi(i)
                    )-1);
            L(istart:istart+Nxi(i)-1) =
                L_line(istart:istart+Nxi(i)
                    )-1);
        end
    end
end

YL = 1 ./ (R + li*omega*L);

end

```

A.5.5 Frequency domain parameters

This function computes the frequency domain parameters for the simulation engine. It uses data provided from the stimulus file (if any) or, in 'custom' mode, user provided inputs for the number of harmonics 'Nh' and the total simulation time 't_max'.

```

function freqparams = TlfrequencySpan(par)
%TLFREQUENCYSPAN Computes the frequency span for the line
    response

```

```

%simulation on the basis of the stimulus signal or over a
  custom spectral
%range. TLFREQUENCYSPAN also gives some useful time domain
  outputs
%
% Detailed explanation goes here

freqmode = par.freqmode;
stimulusfile = par.stimulusfile;
v_line = par.v_line;
l = par.l;

switch freqmode
  case 'signal'
    disp('LineLab >> Loading stimulus data file
      and setting up frequencies')

    wave = load(stimulusfile);
    if isempty(find(contains(fieldnames(wave), 't
      '), 1)) || isempty(find(contains(
      fieldnames(wave), 'v'), 1))
      error('Cannot parse stimulus file');
    end

    t = wave.t;

    % Forcing even number of time-domain samples
    if mod(length(t), 2)
      t = t(1:end-1);
    end

    % Computing fft parameters
    t_max = range(t);
    Nh = length(t)/2 - 1;
    df = 1/t_max;
    omega = 2*pi*df*(1:Nh)';

    % TODO spatial discretization might be
      adaptive
    f_max = omega(end)/2/pi;
    lambda_min = v_line / f_max;
    dx = lambda_min / 10;
    Nx = ceil(l/dx);
    dx = l/Nx;

```

```

case 'custom'
    disp('LineLab >> Setting up custom spectral
        range')

    Nh = par.Nh; % Number of frequencies
    t_max = par.tmax; % Total simulation time
    Nt = 2*(Nh+1); % Number of time-domain
        samples
    dt = t_max / Nt; % Time resolution [s]
    t = (0:dt:(Nt-1)*dt);

    df = 1 / t_max; % Frequency resolution [Hz]
    f_max = Nh * df; % Maximum frequency [Hz]

    lambda_min = v_line / f_max; % Minimum
        wavelength [m]
    dx = lambda_min / 10; % TODO customizable
        lambda_factor
    Nx = ceil(1 / dx); % Number of cells
    dx = 1 / Nx; % Spatial resolution [m]
    omega = 2*pi*df*(1:Nh)';

    omega_max = 2*pi*v_line/lambda_min; % FIXME
        for consistency check
end

freqparams = struct( ...
    'fmax', f_max, ...
    'df', df, ...
    'dx', dx, ...
    'omega', omega, ...
    'Nh', Nh, ...
    'Nx', Nx, ...
    'tmax', t_max, ...
    't', t ...
);

end

```

A.5.6 Tridiagonal solver

This is the code that implements the solver algorithm introduced in Section 4.6.2. The `'measurement_node'` parameter is automatically computed by the software before entering the solver, and is used when the TDR port is not located at the beginning of the Transmission Line.

```

function vh = TlsolveCircuit(YS, Ymeas, YL, YC, Yload,
    measurement_node)
%TLSOLVECIRCUIT Summary of this function goes here
% Detailed explanation goes here
Nx = length(YC);

% Adding measurement port (lumped) admittance
YC(measurement_node) = YC(measurement_node) + Ymeas;

% Tridiagonal vectors (flipped for fast solution)
bY = [0, -YL(end:-1:1)];
cY = [-YL(end:-1:1), 0];

aY = zeros(Nx+1, 1) + 1i*0;
aY(1) = YS + YL(1);
aY(2:end-1) = YL(1:end-1) + YC(1:end-1) + YL(2:end);
aY(end) = YL(end) + YC(end) + Yload;
aY = aY(end:-1:1);

n = Nx+1;
f = zeros([n,1]) + 1i*0; f(end) = YS;
v = zeros([n,1]) + 1i*0;
y = v;
w = aY(1);
y(1) = f(1)/w;
for i = 2:n
    v(i-1) = cY(i-1)/w;
    w = aY(i) - bY(i)*v(i-1);
    y(i) = ( f(i) - bY(i)*y(i-1) )/w;
end
if measurement_node > 1
    for i = n-1:-1:n-measurement_node+1
        y(i) = y(i) - v(i)*y(i+1);
    end
    vh = y(i);
else
    vh = y(end);
end
end

```

Bibliography

- [1] A. Cataldo, G. Cannazza, N. Giaquinto, A. Trotta, and G. Andria, "Microwave TDR for Real-Time Control of Intravenous Drip Infusions", *IEEE Transactions on Instrumentation and Measurement*, vol. 61, no. 7, pp. 1866–1873, Jul. 2012, ISSN: 0018-9456, 1557-9662. DOI: [10.1109/TIM.2012.2192346](https://doi.org/10.1109/TIM.2012.2192346). (visited on 06/06/2016).
- [2] A. Cataldo, E. De Benedetto, and G. Cannazza, "Hydration monitoring and moisture control of cement-based samples through embedded wire-like sensing elements", *IEEE Sensors Journal*, 2014, ISSN: 1530-437X. DOI: [10.1109/JSEN.2014.2360712](https://doi.org/10.1109/JSEN.2014.2360712).
- [3] S. Schuet, D. Timucin, and K. Wheeler, "A Model-Based Probabilistic Inversion Framework for Characterizing Wire Fault Detection Using TDR", *IEEE Transactions on Instrumentation and Measurement*, vol. 60, no. 5, pp. 1654–1663, May 2011, ISSN: 0018-9456. DOI: [10.1109/TIM.2011.2105030](https://doi.org/10.1109/TIM.2011.2105030).
- [4] M. Hagedorn, I. G. Platt, and I. M. Woodhead, "Timber characterisation using a non-invasive TDR sensor", in *2009 IEEE Sensors*, Oct. 2009, pp. 984–987. DOI: [10.1109/ICSENS.2009.5398210](https://doi.org/10.1109/ICSENS.2009.5398210).
- [5] A. Cataldo, E. De Benedetto, G. Cannazza, A. Masciullo, N. Giaquinto, G. M. D'Aucelli, N. Costantino, A. De Leo, and M. Miraglia, "Recent advances in the TDR-based leak detection system for pipeline inspection", *Measurement*, vol. 98, pp. 347–354, Feb. 2017, ISSN: 0263-2241. DOI: [10.1016/j.measurement.2016.09.017](https://doi.org/10.1016/j.measurement.2016.09.017). [Online]. Available: <http://www.sciencedirect.com/science/article/pii/S0263224116305206> (visited on 03/07/2017).
- [6] D. A. Robinson, M. G. Schaap, D. Or, and S. B. Jones, "On the effective measurement frequency of time domain reflectometry in dispersive and nonconductive dielectric materials", in *Water Resources Research*, vol. 41, no. 2, Feb. 2005, ISSN: 00431397. DOI: [10.1029/2004WR003816](https://doi.org/10.1029/2004WR003816). (visited on 06/06/2016).
- [7] N. Giaquinto, G. M. D'Aucelli, E. De Benedetto, G. Cannazza, A. Cataldo, E. Piuze, and A. Masciullo, "Criteria for Automated Estimation of Time of Flight in TDR Analysis", *IEEE Transactions on Instrumentation and Measurement*, pp. 1–10, 2015, ISSN: 0018-9456, 1557-9662. DOI: [10.1109/TIM.2015.2495721](https://doi.org/10.1109/TIM.2015.2495721). (visited on 03/29/2016).
- [8] A. Cataldo, E. Piuze, E. De Benedetto, and G. Cannazza, "Experimental Characterization and Performance Evaluation of Flexible Two-Wire Probes for TDR Monitoring of Liquid Level", *IEEE Transactions on Instrumentation and Measurement*, vol. 63, no. 12, pp. 2779–2788, Dec. 2014, ISSN: 0018-9456, 1557-9662. DOI:

- 10.1109/TIM.2014.2318393. [Online]. Available: <http://ieeexplore.ieee.org/document/6810879/> (visited on 05/08/2017).
- [9] N. Hirai, T. Yamada, and Y. Ohki, "Comparison of broadband impedance spectroscopy and time domain reflectometry for locating cable degradation", in *2012 International Conference on Condition Monitoring and Diagnosis (CMD)*, Sep. 2012, pp. 229–232. DOI: 10.1109/CMD.2012.6416417.
- [10] E. Piuze, A. Cataldo, and L. Catarinucci, "Enhanced reflectometry measurements of permittivities and levels in layered petrochemical liquids using an "in-situ" coaxial probe", in *Measurement*, vol. 42, no. 5, pp. 685–696, Jun. 2009, ISSN: 02632241. DOI: 10.1016/j.measurement.2008.11.002. (visited on 06/06/2016).
- [11] S. Galli and K. J. Kerpez, "Single-ended loop make-up identification-part I: A method of analyzing TDR measurements", *IEEE Transactions on Instrumentation and Measurement*, vol. 55, no. 2, pp. 528–537, Apr. 2006, ISSN: 0018-9456. DOI: 10.1109/TIM.2006.870134.
- [12] A. Cataldo, G. Cannazza, E. De Benedetto, and N. Giaquinto, "A TDR-based system for the localization of leaks in newly installed, underground pipes made of any material", *Measurement Science and Technology*, vol. 23, no. 10, p. 105 010, 2012.
- [13] J. Lundstedt, S. Strom, and S. He, "Time-domain signal restoration and parameter reconstruction on an LCRG transmission line", in *1995 URSI International Symposium on Signals, Systems, and Electronics, 1995. ISSSE '95, Proceedings*, Oct. 1995, pp. 323–326. DOI: 10.1109/ISSSE.1995.497999.
- [14] J. Lundstedt and S. He, "A time-domain optimization technique for the simultaneous reconstruction of the characteristic impedance, resistance and conductance of a transmission line", *Journal of Electromagnetic Waves and Applications*, vol. 10, no. 4, pp. 581–601, Jan. 1996, ISSN: 0920-5071. DOI: 10.1163/156939396X01143. [Online]. Available: <https://doi.org/10.1163/156939396X01143>.
- [15] J. Lundstedt and S. Ström, "Simultaneous reconstruction of two parameters from the transient response of a nonuniform LCRG transmission line", *Journal of Electromagnetic Waves and Applications*, vol. 10, no. 1, pp. 19–50, Jan. 1996, ISSN: 0920-5071. DOI: 10.1163/156939396X00199. [Online]. Available: <https://doi.org/10.1163/156939396X00199>.
- [16] M. K. Smail, H. R.E. H. Bouchehara, L. Pichon, H. Boudjefdjouf, A. Amloune, and Z. Lacheheb, "Non-destructive diagnosis of wiring networks using time domain reflectometry and an improved black hole algorithm", *Nondestructive Testing and Evaluation*, vol. 32, no. 3, pp. 286–300, Jul. 2017, ISSN: 1058-9759. DOI: 10.1080/10589759.2016.1200576. [Online]. Available: <https://doi.org/10.1080/10589759.2016.1200576>.

- [17] A. Scheuermann and C. Huebner, "On the Feasibility of Pressure Profile Measurements With Time-Domain Reflectometry", *IEEE Transactions on Instrumentation and Measurement*, vol. 58, no. 2, pp. 467–474, Feb. 2009, ISSN: 0018-9456. DOI: [10.1109/TIM.2008.928876](https://doi.org/10.1109/TIM.2008.928876).
- [18] A. Scheuermann, C. Gonzales, J. Fan, B. Braga, T. Baumgartl, D. Lockington, S. Schlaeger, R. Becker, N. Wagner, and C. Hubner, "Spatial Time Domain Reflectometry (spatial TDR) in geo-environmental engineering", in *Sensors Applications Symposium (SAS), 2014 IEEE*, IEEE, 2014, pp. 237–241. [Online]. Available: <http://ieeexplore.ieee.org/abstract/document/6798953/> (visited on 03/28/2017).
- [19] S. Schlaeger, "A fast TDR-inversion technique for the reconstruction of spatial soil moisture content", *Hydrol. Earth Syst. Sci.*, vol. 9, no. 5, pp. 481–492, Oct. 2005, ISSN: 1607-7938. DOI: [10.5194/hess-9-481-2005](https://doi.org/10.5194/hess-9-481-2005). [Online]. Available: <http://www.hydrol-earth-syst-sci.net/9/481/2005/> (visited on 03/29/2017).
- [20] M. K. Smail, H. R.E. H. Boucekara, L. Pichon, H. Boudjefdjouf, and R. Mehasni, "Diagnosis of wiring networks using Particle Swarm Optimization and Genetic Algorithms", *Computers & Electrical Engineering*, vol. 40, no. 7, pp. 2236–2245, Oct. 2014, ISSN: 0045-7906. DOI: [10.1016/j.compeleceng.2014.07.002](https://doi.org/10.1016/j.compeleceng.2014.07.002). [Online]. Available: <http://www.sciencedirect.com/science/article/pii/S0045790614001803> (visited on 04/21/2017).
- [21] N. Giaquinto, A. Cataldo, G. D Aucelli, E. De Benedetto, and G. Cannazza, "Water detection using bi-wires as sensing elements: Comparison between capacitance-based and Time-of-Flight-Based Techniques", *IEEE Sensors Journal*, 2016. DOI: [10.1109/JSEN.2016.2540299](https://doi.org/10.1109/JSEN.2016.2540299).
- [22] A. Cataldo, G. Cannazza, E. D. Benedetto, and N. Giaquinto, "A TDR-based system for the localization of leaks in newly installed, underground pipes made of any material", in *Measurement Science and Technology*, vol. 23, no. 10, 2012, ISSN: 0957-0233. DOI: [10.1088/0957-0233/23/10/105010](https://doi.org/10.1088/0957-0233/23/10/105010). (visited on 01/24/2017).
- [23] G. M. D'Aucelli, N. Giaquinto, and G. Andria, "LineLab: A Transmission Line Simulator for Distributed Sensing Systems", English, *IEEE Antennas and Propagation Magazine (accepted for publication)*, Aug. 2017.
- [24] S. Sun, D. Pommerenke, J. Drewniak, G. Chen, L. Xue, M. Brower, and M. Koledintseva, "A novel tdr-based coaxial cable sensor for crack/strain sensing in reinforced concrete structures", *IEEE Transactions on Instrumentation and Measurement*, vol. 58, no. 8, pp. 2714–2725, 2009.
- [25] T. Hauschild and F. Menke, "Moisture measurement in masonry walls using a non-invasive reflectometer", *Electronics Letters*, vol. 34, no. 25, pp. 2413–2414, 1998.
- [26] H. Kääriäinen, M. Rudolph, D. Schaurich, K. Tulla, and H. Wiggenhauser, "Moisture measurements in building materials with microwaves", *NDT and E International*, vol. 34, no. 6, pp. 389–394, 2001.

- [27] S. Kharkovsky, M. Akay, U. Hasar, and C. Atis, "Measurement and monitoring of microwave reflection and transmission properties of cement-based specimens", *Instrumentation and Measurement, IEEE Transactions on*, vol. 51, no. 6, pp. 1210–1218, 2002, ISSN: 0018-9456. DOI: [10.1109/TIM.2002.808081](https://doi.org/10.1109/TIM.2002.808081).
- [28] H. Bolvin and A. Chambarel, "Electromagnetic wave propagation in polarizable wet media: Application to a tdr probe", *Measurement Science and Technology*, vol. 18, no. 4, pp. 1105–1109, 2007.
- [29] I. Platt and I. Woodhead, "A 1d inversion for non-invasive time domain reflectometry", *Measurement Science and Technology*, vol. 19, no. 5, 2008.
- [30] U. Kaatzke and C. Hubner, "Electromagnetic techniques for moisture content determination of materials", *Measurement Science and Technology*, vol. 21, no. 8, 2010.
- [31] A. Scheuermann, C. Hübner, H. Wienbroer, D. Rebstock, and G. Huber, "Fast time domain reflectometry (tdr) measurement approach for investigating the liquefaction of soils", *Measurement Science and Technology*, vol. 21, no. 2, 2010.
- [32] M. Lin, J. Thaduri, and A. Abatan, "Development of an electrical time domain reflectometry (etdr) distributed strain sensor", *Measurement Science and Technology*, vol. 16, no. 7, pp. 1495–1505, 2005.
- [33] E. Bruvik, B. Hjertaker, K. Folgero, and S. Meyer, "Monitoring oil-water mixture separation by time domain reflectometry", *Measurement Science and Technology*, vol. 23, no. 12, 2012.
- [34] J. Kolakowski, "Application of ultra-fast comparator for UWB pulse time of arrival measurement", in *2011 IEEE International Conference on Ultra-Wideband (ICUWB)*, Sep. 2011, pp. 470–473. DOI: [10.1109/ICUWB.2011.6058888](https://doi.org/10.1109/ICUWB.2011.6058888).
- [35] Y. C. Chung, N. Amarnath, and C. Furse, "Capacitance and inductance sensor circuits for detecting the lengths of open- and short-circuited wires", *IEEE Transactions on Instrumentation and Measurement*, vol. 58, no. 8, pp. 2495–2502, 2009.
- [36] R. Dean, A. Rane, M. Baginski, J. Richard, Z. Hartzog, and D. Elton, "A capacitive fringing field sensor design for moisture measurement based on printed circuit board technology", *IEEE Transactions on Instrumentation and Measurement*, vol. 61, no. 4, pp. 1105–1112, 2012.
- [37] J. Ong, Z. You, J. Mills-Beale, E. L. Tan, B. Pereles, and K. G. Ong, "A wireless, passive embedded sensor for real-time monitoring of water content in civil engineering materials", *IEEE Sensors Journal*, vol. 8, no. 12, pp. 2053–2058, 2008.
- [38] P. Ramos, M. Fonseca da Silva, and A. Cruz Serra, "Impedance measurement using a least-squares waveform fitting algorithm", in *Precision Electromagnetic Measurements Digest, 2004 Conference on*, 2004, pp. 125–126. DOI: [10.1109/CPEM.2004.305492](https://doi.org/10.1109/CPEM.2004.305492).
- [39] E. Saenz, P. M. T. Ikonen, R. Gonzalo, and S. A. Tretyakov, "On the Definition of Effective Permittivity and Permeability For Thin Composite Layers", *AIP Journal of Applied Physics*, vol. 101, Jun. 2007.

- [40] N. Giaquinto, A. Cataldo, E. Piuzzi, E. De Benedetto, G. M. D'Aucelli, and G. Cannazza, "Diffused capacitance-based sensing for hydric control and watering optimization", in *Proceeding of the 20th IMEKO TC4 International Symposium and 18th International Workshop on ADC Modelling and Testing*, 2014.
- [41] S. Jones, J. Wraith, and D. Or, "Time domain reflectometry measurement principles and applications", *Hydrological Processes*, vol. 16, no. 1, pp. 141–153, 2002.
- [42] N. Giaquinto, G. M. D'Aucelli, E. De Benedetto, G. Cannazza, A. Cataldo, E. Piuzzi, and A. Masciullo, "Accuracy analysis in the estimation of ToF of TDR signals", in *Instrumentation and Measurement Technology Conference (I2MTC), 2015 IEEE International*, IEEE, 2015, pp. 187–192. [Online]. Available: http://ieeexplore.ieee.org/xpls/abs_all.jsp?arnumber=7151263 (visited on 03/29/2016).
- [43] R. Gallorini and N. Abouchi, "A capacitance meter based on an oversampling sigma-delta modulator and its application to capacitive sensor interface", in *The 8th IEEE International Conference on Electronics, Circuits and Systems, 2001. ICECS 2001*, vol. 3, 2001, 1537–1540 vol.3.
- [44] S. Xudong, Z. Jianzhong, J. Tao, and W. Liwen, "Design of aircraft cable intelligent fault diagnosis and location system based on time domain reflection", in *2010 8th World Congress on Intelligent Control and Automation*, Jul. 2010, pp. 5856–5860. DOI: [10.1109/WCICA.2010.5554557](https://doi.org/10.1109/WCICA.2010.5554557).
- [45] C. Furse, "Reflectometry for Structural Health Monitoring", en, in *New Developments in Sensing Technology for Structural Health Monitoring*, ser. Lecture Notes in Electrical Engineering 96, S. C. Mukhopadhyay, Ed., DOI: [10.1007/978-3-642-21099-0_8](https://doi.org/10.1007/978-3-642-21099-0_8), Springer Berlin Heidelberg, 2011, pp. 159–185, ISBN: 978-3-642-21098-3 978-3-642-21099-0. [Online]. Available: http://link.springer.com/chapter/10.1007/978-3-642-21099-0_8 (visited on 06/20/2017).
- [46] A. Cataldo, G. Cannazza, E. De Benedetto, and N. Giaquinto, "A New Method for Detecting Leaks in Underground Water Pipelines", *IEEE Sensors Journal*, vol. 12, no. 6, pp. 1660–1667, Jun. 2012, ISSN: 1530-437X, 1558-1748. DOI: [10.1109/JSEN.2011.2176484](https://doi.org/10.1109/JSEN.2011.2176484). [Online]. Available: <http://ieeexplore.ieee.org/lpdocs/epic03/wrapper.htm?arnumber=6084808> (visited on 06/06/2016).
- [47] Shishuang Sun, D. Pommerenke, J. Drewniak, Genda Chen, Liang Xue, M. Brower, and M. Koledintseva, "A Novel TDR-Based Coaxial Cable Sensor for Crack/Strain Sensing in Reinforced Concrete Structures", *IEEE Transactions on Instrumentation and Measurement*, vol. 58, no. 8, pp. 2714–2725, Aug. 2009, ISSN: 0018-9456, 1557-9662. DOI: [10.1109/TIM.2009.2015706](https://doi.org/10.1109/TIM.2009.2015706). [Online]. Available: <http://ieeexplore.ieee.org/document/5153319/> (visited on 06/20/2017).
- [48] C. P. Nemarich, "Time domain reflectometry liquid level sensors", *IEEE Instrumentation Measurement Magazine*, vol. 4, no. 4, pp. 40–44, Dec. 2001, ISSN: 1094-6969. DOI: [10.1109/5289.975464](https://doi.org/10.1109/5289.975464).

- [49] A. Cataldo, L. Tarricone, F. Attivissimo, and A. Trotta, "Simultaneous measurement of dielectric properties and levels of liquids using a TDR method", *Measurement, Innovative Design and Paradigms in Instrumentation and Measurements*, vol. 41, no. 3, pp. 307–319, Apr. 2008, ISSN: 0263-2241. DOI: 10.1016/j.measurement.2006.11.006. [Online]. Available: <http://www.sciencedirect.com/science/article/pii/S0263224106002296>.
- [50] S. M. Kim, J. H. Sung, W. Park, J. H. Ha, Y. J. Lee, and H. B. Kim, "Development of a Monitoring System for Multichannel Cables Using TDR", *IEEE Transactions on Instrumentation and Measurement*, vol. 63, no. 8, pp. 1966–1974, Aug. 2014, ISSN: 0018-9456. DOI: 10.1109/TIM.2014.2304353.
- [51] J. H. Yu and Y. G. Dong, "A Digitalized Implementation of Time-of-Flight Measurement for Cable Fault Location", EN, *Applied Mechanics and Materials*, vol. 336-338, pp. 88–95, 2013, ISSN: 1662-7482. DOI: 10.4028/www.scientific.net/AMM.336-338.88. [Online]. Available: <https://www.scientific.net/AMM.336-338.88> (visited on 06/20/2017).
- [52] G. C. Topp, J. L. Davis, and A. P. Annan, "Electromagnetic determination of soil water content: Measurements in coaxial transmission lines", en, *Water Resources Research*, vol. 16, no. 3, pp. 574–582, Jun. 1980, ISSN: 1944-7973. DOI: 10.1029/WR016i003p00574. [Online]. Available: <http://onlinelibrary.wiley.com/doi/10.1029/WR016i003p00574/abstract>.
- [53] T. J. Heimovaara, W. Bouten, and J. M. Verstraten, "Frequency domain analysis of time domain reflectometry waveforms: 2. A four-component complex dielectric mixing model for soils", en, *Water Resources Research*, vol. 30, no. 2, pp. 201–209, Feb. 1994, ISSN: 1944-7973. DOI: 10.1029/93WR02949. [Online]. Available: <http://onlinelibrary.wiley.com/doi/10.1029/93WR02949/abstract>.
- [54] D. J. Timlin and Y. A. Pachepsky, "Comparison of Three Methods to Obtain the Apparent Dielectric Constant from Time Domain Reflectometry Wave Traces", en, *Soil Science Society of America Journal*, vol. 60, no. 4, pp. 970–977, 1996, ISSN: 0361-5995. DOI: 10.2136/sssaj1996.03615995006000040003x. [Online]. Available: <https://dl.sciencesocieties.org/publications/sssaj/abstracts/60/4/SS0600040970?access=0&view=pdf> (visited on 06/20/2017).
- [55] C. Parkey, C. Hughes, and N. Locken, "Analyzing artifacts in the time domain waveform to locate wire faults", *IEEE Instrumentation Measurement Magazine*, vol. 15, no. 4, pp. 16–21, Aug. 2012, ISSN: 1094-6969. DOI: 10.1109/MIM.2012.6263978.
- [56] D. L. Donoho, "De-noising by soft-thresholding", *IEEE Transactions on Information Theory*, vol. 41, no. 3, pp. 613–627, May 1995, ISSN: 0018-9448. DOI: 10.1109/18.382009.

- [57] P. J. Pupalaiakis, "Wavelet Denoising For TDR Dynamic Range Improvement", 2011. [Online]. Available: http://cdn.teledynelecroy.com/files/whitepapers/wavelet_denoising_tdr_dynamic_range_improvement.pdf (visited on 06/20/2017).
- [58] A. M. Nicolson, "Forming the fast Fourier transform of a step response in time-domain metrology", *Electronics Letters*, vol. 9, no. 14, pp. 317–318, Jul. 1973, ISSN: 0013-5194. DOI: [10.1049/el:19730228](https://doi.org/10.1049/el:19730228).
- [59] D. M. Pozar, "Microwave engineering", in, 4th ed. Hoboken, NJ: Wiley, 2012, ch. 2, ISBN: 978-0-470-63155-3.
- [60] *Linelab project - git repository*. [Online]. Available: <https://bitbucket.org/misurepoliba/linelab-simulator>.
- [61] R. B. Marks and D. F. Williams, "A General Waveguide Circuit Theory", *Journal of Research of the National Institute of Standards and Technology*, vol. 97, no. 5, pp. 533–562, 1992, ISSN: 1044-677X. DOI: [10.6028/jres.097.024](https://doi.org/10.6028/jres.097.024).
- [62] M. Ansarizadeh, A. Ghorbani, and R. A. Abd-Alhameed, "An approach to equivalent circuit modeling of rectangular microstrip antennas", *Progress In Electromagnetics Research B*, vol. 8, pp. 77–86, 2008.
- [63] J. G. Maloney, K. L. Shlager, and G. S. Smith, "A simple FDTD model for transient excitation of antennas by transmission lines", *IEEE Transactions on Antennas and Propagation*, vol. 42, no. 2, pp. 289–292, Feb. 1994, ISSN: 0018-926X. DOI: [10.1109/8.277228](https://doi.org/10.1109/8.277228).
- [64] S. Asadi and B. Honarbakhsh, "Linear Analysis of High-Frequency Field-Effect Transistors Using the CN-FDTD Method", *IEEE Transactions on Microwave Theory and Techniques*, vol. 65, no. 6, pp. 1946–1954, Jun. 2017, ISSN: 0018-9480. DOI: [10.1109/TMTT.2016.2645566](https://doi.org/10.1109/TMTT.2016.2645566).
- [65] L. Sevgi and C. Uluisik, "A MATLAB-based transmission-line virtual tool: Finite-difference time-domain reflectometer", *IEEE Antennas and Propagation Magazine*, vol. 48, no. 1, pp. 141–145, Feb. 2006, ISSN: 1045-9243. DOI: [10.1109/MAP.2006.1645595](https://doi.org/10.1109/MAP.2006.1645595).
- [66] T. P. Montoya, "Modeling 1-D FDTD transmission line voltage sources and terminations with parallel and series RLC loads", in *IEEE Antennas and Propagation Society International Symposium (IEEE Cat. No.02CH37313)*, vol. 4, 2002, 242–245 vol.4. DOI: [10.1109/APS.2002.1016969](https://doi.org/10.1109/APS.2002.1016969).
- [67] A. Orlandi and C. R. Paul, "FDTD analysis of lossy, multiconductor transmission lines terminated in arbitrary loads", *IEEE Transactions on Electromagnetic Compatibility*, vol. 38, no. 3, pp. 388–399, Aug. 1996, ISSN: 0018-9375. DOI: [10.1109/15.536069](https://doi.org/10.1109/15.536069).
- [68] G. Kristensson, S. Rikte, and A. Sihvola, "Mixing formulas in time domain", Lund Institute of Technology, Sweden, Tech. Rep., 1997, p. 26.

- [69] A. Scarlatti and C. L. Holloway, "An equivalent transmission-line model containing dispersion for high-speed digital lines-with an FDTD implementation", *IEEE Transactions on Electromagnetic Compatibility*, vol. 43, no. 4, pp. 504–514, Nov. 2001, ISSN: 0018-9375. DOI: [10.1109/15.974629](https://doi.org/10.1109/15.974629).
- [70] J. R. Marti, "Accurate modelling of frequency-dependent transmission lines in electromagnetic transient simulations", *Power Apparatus and Systems, IEEE Transactions on*, no. 1, pp. 147–157, 1982.
- [71] "IEEE Standard for Transitions, Pulses, and Related Waveforms", *IEEE Std 181-2011 (Revision of IEEE Std 181-2003)*, pp. 1–71, Sep. 2011. DOI: [10.1109/IEEESTD.2011.6016198](https://doi.org/10.1109/IEEESTD.2011.6016198).
- [72] N. Higham, *Accuracy and Stability of Numerical Algorithms*, ser. Other Titles in Applied Mathematics. Society for Industrial and Applied Mathematics, Jan. 2002, ISBN: 978-0-89871-521-7.
- [73] *TDR200: Time-Domain Reflectometer*. [Online]. Available: <https://www.campbellsci.com/tdr200>.
- [74] O. Dahan, E. V. McDonald, and M. H. Young, "Flexible Time Domain Reflectometry Probe for Deep Vadose Zone Monitoring", en, *Vadose Zone Journal*, vol. 2, no. 2, pp. 270–275, May 2003, ISSN: 1539-1663. DOI: [10.2113/2.2.270](https://doi.org/10.2113/2.2.270). [Online]. Available: <http://vzj.geoscienceworld.org/content/2/2/270> (visited on 03/29/2017).
- [75] Campbell Scientific, *CS Soil TDR Probes*, English, Campbell Scientific, Campbell Scientific. [Online]. Available: https://s.campbellsci.com/documents/us/category-brochures/b_tdr_probes.pdf (visited on 06/29/2017).
- [76] Joint Committee for Guides in Metrology (JCGM), *International vocabulary of metrology – Basic and general concepts and associated terms (VIM)*, English, 2012.
- [77] Pasternack, *RG316-U cable datasheet*.
- [78] D. A. Frickey, "Conversions between S, Z, Y, H, ABCD, and T parameters which are valid for complex source and load impedances", *IEEE Transactions on Microwave Theory and Techniques*, vol. 42, no. 2, pp. 205–211, Feb. 1994, ISSN: 0018-9480. DOI: [10.1109/22.275248](https://doi.org/10.1109/22.275248).
- [79] D. Bänninger, H. Wunderli, M. Nussberger, and H. Flühler, "Inversion of TDR signals—revisited", en, *Journal of Plant Nutrition and Soil Science*, vol. 171, no. 2, pp. 137–145, Apr. 2008, ISSN: 1522-2624. DOI: [10.1002/jpln.200700179](https://doi.org/10.1002/jpln.200700179). [Online]. Available: <http://onlinelibrary.wiley.com/doi/10.1002/jpln.200700179/abstract>.
- [80] X. Feng, L. Qi, and J. Pan, "Fault inductance based protection for DC distribution systems", in *13th International Conference on Development in Power System Protection 2016 (DPSP)*, Mar. 2016, pp. 1–6. DOI: [10.1049/cp.2016.0032](https://doi.org/10.1049/cp.2016.0032).

- [81] A. Laib, M. Melit, B. Nekhoul, K. Kerroum, and K. E. Drissi, "A new hybrid approach using time-domain reflectometry combined with wavelet and neural network for fault identification in wiring network", in *2016 8th International Conference on Modelling, Identification and Control (ICMIC)*, Nov. 2016, pp. 290–295. DOI: [10.1109/ICMIC.2016.7804125](https://doi.org/10.1109/ICMIC.2016.7804125).
- [82] A. B. Fernandes, W. L. A. Neves, E. G. Costa, and M. N. Cavalcanti, "Transmission line shunt conductance from measurements", *IEEE Transactions on Power Delivery*, vol. 19, no. 2, pp. 722–728, Apr. 2004, ISSN: 0885-8977. DOI: [10.1109/TPWRD.2003.822526](https://doi.org/10.1109/TPWRD.2003.822526).
- [83] M. K. Smail, L. Pichon, M. Olivas, F. Auzanneau, and M. Lambert, "Detection of Defects in Wiring Networks Using Time Domain Reflectometry", *IEEE Transactions on Magnetics*, vol. 46, no. 8, pp. 2998–3001, Aug. 2010, ISSN: 0018-9464. DOI: [10.1109/TMAG.2010.2043720](https://doi.org/10.1109/TMAG.2010.2043720).
- [84] A. Cataldo, E. D. Benedetto, G. Cannazza, C. Huebner, D. Trebbels, N. Gi-aquinto, and G. M. D'Aucelli, "Controlling the irrigation process in agriculture through elongated TDR-sensing cables", in *2017 IEEE International Instrumentation and Measurement Technology Conference (I2MTC)*, May 2017, pp. 1–6. DOI: [10.1109/I2MTC.2017.7969761](https://doi.org/10.1109/I2MTC.2017.7969761).
- [85] G. E. P. Ropella, D. A. Nag, and C. A. Hunt, "Similarity measures for automated comparison of in silico and in vitro experimental results", in *Proceedings of the 25th Annual International Conference of the IEEE Engineering in Medicine and Biology Society (IEEE Cat. No.03CH37439)*, vol. 3, Sep. 2003, 2933–2936 Vol.3. DOI: [10.1109/IEMBS.2003.1280532](https://doi.org/10.1109/IEMBS.2003.1280532).
- [86] H. Sakoe and S. Chiba, "Dynamic programming algorithm optimization for spoken word recognition", *IEEE Transactions on Acoustics, Speech, and Signal Processing*, vol. 26, no. 1, pp. 43–49, Feb. 1978, ISSN: 0096-3518. DOI: [10.1109/TASSP.1978.1163055](https://doi.org/10.1109/TASSP.1978.1163055).
- [87] F. Quiero, F. Quintana, and L. Bennun, "A novel method based on cross correlation maximization, for pattern matching by means of a single parameter. Application to the human voice", *arXiv preprint arXiv:1503.03022*, 2015. [Online]. Available: <https://arxiv.org/abs/1503.03022> (visited on 07/12/2017).
- [88] T. Prätzlich, J. Driedger, and M. Müller, "Memory-restricted multiscale dynamic time warping", in *2016 IEEE International Conference on Acoustics, Speech and Signal Processing (ICASSP)*, Mar. 2016, pp. 569–573. DOI: [10.1109/ICASSP.2016.7471739](https://doi.org/10.1109/ICASSP.2016.7471739).
- [89] L. Gupta, D. L. Molfese, R. Tammana, and P. G. Simos, "Nonlinear alignment and averaging for estimating the evoked potential", *IEEE Transactions on Biomedical Engineering*, vol. 43, no. 4, pp. 348–356, Apr. 1996, ISSN: 0018-9294. DOI: [10.1109/10.486255](https://doi.org/10.1109/10.486255).

- [90] D. Silva and G. Batista, "Speeding Up All-Pairwise Dynamic Time Warping Matrix Calculation", in *Proceedings of the 2016 SIAM International Conference on Data Mining*, ser. Proceedings, DOI: 10.1137/1.9781611974348.94, Society for Industrial and Applied Mathematics, Jun. 2016, pp. 837–845. [Online]. Available: <http://epubs.siam.org/doi/abs/10.1137/1.9781611974348.94>.
- [91] P. Rocca, G. Oliveri, and A. Massa, "Differential Evolution as Applied to Electromagnetics", *IEEE Antennas and Propagation Magazine*, vol. 53, no. 1, pp. 38–49, Feb. 2011, ISSN: 1045-9243. DOI: 10.1109/MAP.2011.5773566.
- [92] S. Yang, A. Qing, and Y. B. Gan, "Synthesis of low sidelobe antenna arrays using the differential evolution algorithm", in *IEEE Antennas and Propagation Society International Symposium. Digest. Held in conjunction with: USNC/CNC/URSI North American Radio Sci. Meeting (Cat. No.03CH37450)*, vol. 1, Jun. 2003, 780–783 vol.1. DOI: 10.1109/APS.2003.1217577.
- [93] S. Yang, Y. Beng Gan, and A. Qing, "Moving phase center antenna arrays with optimized static excitations", en, *Microwave and Optical Technology Letters*, vol. 38, no. 1, pp. 83–85, Jul. 2003, ISSN: 1098-2760. DOI: 10.1002/mop.10977. [Online]. Available: <http://onlinelibrary.wiley.com/doi/10.1002/mop.10977/abstract>.
- [94] A. Semnani, M. Kamyab, and I. T. Rekanos, "Reconstruction of One-Dimensional Dielectric Scatterers Using Differential Evolution and Particle Swarm Optimization", *IEEE Geoscience and Remote Sensing Letters*, vol. 6, no. 4, pp. 671–675, Oct. 2009, ISSN: 1545-598X. DOI: 10.1109/LGRS.2009.2023246.
- [95] R. Storn and K. Price, "Differential Evolution – A Simple and Efficient Heuristic for global Optimization over Continuous Spaces", en, *Journal of Global Optimization*, vol. 11, no. 4, pp. 341–359, Dec. 1997, ISSN: 0925-5001, 1573-2916. DOI: 10.1023/A:1008202821328. [Online]. Available: <https://link.springer.com/article/10.1023/A:1008202821328> (visited on 07/14/2017).
- [96] Pasternack, *RG58c-U cable datasheet*. [Online]. Available: <https://www.pasternack.com/images/ProductPDF/RG58C-U.pdf> (visited on 07/04/2017).